UNIVERSITÉ DE NANTES
FACULTÉ DES SCIENCES ET DES TECHNIQUES

———

ÉCOLE DOCTORALE
VEGETAL, ENVIRONNEMENT, NUTRITION, AGROALIMENTAIRE, MER

Année 2012

Modélisation mécanique de la fracture et de la fragmentation d'aliments céréaliers modèle sous des conditions aux limites de la mastication

———

THÈSE DE DOCTORAT
Discipline : Science des matériaux
Spécialité : Science des matériaux

Présentée
et soutenue publiquement par

Lotfi HEDJAZI

Le 15 janvier 2010, devant le jury ci-dessous

Président		
Rapporteurs	M. S. FOREST	Professeur, Mines Paristech
	M. I. C. TRELEA	Professeur, AgroParistech
Examinateurs	Mme. M-A. PEYRON	Chargé de recherche, INRA Theix
	M. C. L. MARTIN	Directeur de recherche, CNRS
	M. N. MOES	Professeur, Ecole Centrale de Nantes
	M. J. LEGRAND	Professeur, Université de Nantes
Invité	Invité M. E. QANNARI	Professeur, ONIRIS Nantes

Directeur de thèse : Guy DELLA VALLE

Co-directeur de thèse : Sofiane GUESSASMA

ED : ……
(Uniquement pour STIM et SPIGA)

UNIVERSITÉ DE NANTES
FACULTÉ DES SCIENCES ET DES TECHNIQUES

———

ÉCOLE DOCTORALE
VEGETAL, ENVIRONNEMENT, NUTRITION, AGROALIMENTAIRE, MER

Année 2012

Modélisation mécanique de la fracture et de la fragmentation d'aliments céréaliers modèle sous des conditions aux limites de la mastication

———

THÈSE DE DOCTORAT
Discipline : Science des matériaux
Spécialité : Science des matériaux

Présentée
et soutenue publiquement par

Lotfi HEDJAZI

Le 15 janvier 2010, devant le jury ci-dessous

Président		
Rapporteurs	M. S. FOREST	Professeur, Mines Paristech
	M. I. C. TRELEA	Professeur, AgroParistech
Examinateurs	Mme. M-A. PEYRON	Chargé de recherche, INRA Theix
	M. C. L. MARTIN	Directeur de recherche, CNRS
	M. N. MOES	Professeur, Ecole Centrale de Nantes
	M. J. LEGRAND	Professeur, Université de Nantes
Invité	Invité M. E. QANNARI	Professeur, ONIRIS Nantes

Directeur de thèse : Guy DELLA VALLE

Co-directeur de thèse : Sofiane GUESSASMA

ED : ……
(Uniquement pour STIM et SPIGA)

Remerciements

En préambule à mon mémoire, je souhaiterais adresser mes remerciements les plus Chaleureux à M. Sofiane GUESSASMA, chargé de recherche à l'INRA de Nantes, de part sa qualité humaine et scientifique pour l'encadrement qu'il m'a fourni et du bénéfice que j'en ai tiré tout au long de ma présence avec lui, il m'a permis de contribué à l'élaboration de ce mémoire qui n'aurait pas vu le jour sans son aide.

Je tiens à remercier aussi directeur de thèse, M. Guy DELLA VALLE, en tant qu'ingénieur de recherche à l'INRA il s'est toujours montré à l'écoute et très disponible tout au long de la réalisation de ce mémoire.

Je remercie également les rapporteurs et les membres du jury qui ont bien voulu me faire l'honneur de juger mon travail.

Il m'est également impossible d'oublier les personnes suivantes qui m'ont accueillis dans leur laboratoires: M. Christophe MARTIN et M. Remy DENDIEVEL du laboratoire SIMAP à Grenoble ainsi que M. Christian SALLES et Mme Claude YVEN du laboratoire FLAVIC à Dijon.

Je remercie chaleureusement M. Noureddine BENSEDDIQ, Professeur à l'université de Lille, qui a corrigé et enrichi ce travail avec des remarques qui m'ont permis d'apporter d'ultimes améliorations. Pour sa générosité et la grande patience dont il a su faire preuve malgré ses charges académiques et personnelles.

Je souhaite évidemment remercier les différentes personnes de l'équipe MC2 pour leur soutien scientifique mais aussi et surtout pour avoir réussi à créer une super ambiance au sein et en dehors du laboratoire. Merci à Hubert, Roselyne, Laurent, Denis, Jane, … Merci à tous les doctorants, post-doctorants, et chercheurs de l'INRA.

Je n'oublie pas mes parents et toute ma famille pour leur contribution, leur soutien et leur patience, et tout particulièrement à mon frère Farid HEDJAZI.

Enfin, j'adresse mes plus sincères remerciements à tous mes proches et amis, qui m'ont toujours soutenue et encouragée au cours de la réalisation de ce mémoire.

Merci à tous et à toutes.

SOMMAIRE

Introduction générale

1. Contexte et objectif :

A la frontière entre l'élaboration des aliments et la nutrition, l'INRA a ouvert un programme de recherches sur la compréhension, en termes de cinétiques et de localisation, du devenir des aliments dans le Tube Digestif (TD) chez l'homme. La modélisation de l'ensemble ouvrirait la voie à la compréhension du comportement d'ingestion et de digestion chez l'homme. Outre les aspects cognitifs, les retombées d'un tel programme conduiraient à la conception d'aliments aux propriétés souhaitées, pour des populations ciblées. Il est donc essentiel d'étudier la transformation de l'aliment dans la cavité buccale, première étape du TD, dans la mesure où celle-ci lui confère ses propriétés de transport (viscosité, taille de particules), essentielles pour la vidange gastrique.

Dans ce contexte, cette thèse, s'appuie sur les compétences de l'UR-BIA sur la structure et les propriétés des produits à base d'amidon, et en particulier sur l'activité récente de modélisation de leurs propriétés mécaniques, cette activité ayant été initiée par des collaboration dans le domaine de la mécanique des matériaux notamment avec le SIMAP-GPM2 (Grenoble), LML (Lille) et Femto-st (Besançon). En outre, elle bénéficie de la collaboration antérieure au sein de l'INRA avec l'UMR-INRA-CSGA (Dijon), où sont étudiés les mécanismes de libération d'arômes en bouche, grâce notamment à un masticateur artificiel ; elle a également été l'occasion d'initier une collaboration sur des aspects numériques avec le GéM-ECN (Nantes) par une action PEPS-CNRS.

La mastication est un processus physiologique qui conduit à la déstructuration mécanique de l'aliment. C'est la première étape de la digestion ; elle permet de réduire la taille des aliments et de former un bol alimentaire en vue de sa déglutition. L'activité musculaire, qui aboutit à la dégradation par des mécanismes de fragmentation et d'agglomération, détermine un profil masticatoire. D'un point de vue mécanique, l'action des dents est comparable à une combinaison de compression et de cisaillement. Son efficacité dépend des caractéristiques physiologiques de l'individu (âge, état dentaire ….). Nous nous proposons d'étudier, dans cette thèse, les effets des aliments céréaliers sur la mastication humaine. Les céréales sont une part importante de l'alimentation humaine, et l'amidon en est le constituant majeur. Les aliments céréaliers se présentent fréquemment sous la forme de produits alvéolaires, au comportement mécanique fragile (biscuits…) ou ductile (pain).

L'objectif de ce travail est donc de modéliser la mastication humaine des produits céréaliers alvéolaires fragiles. Dans ce but, nous avons développé une approche de

modélisation mécanique qui prend en compte les échelles structurales associées à l'aliment : géométrie et densité du produit, structure cellulaire, paroi solide. Ces modèles doivent être capables de représenter l'effet des paramètres physiologiques (profil masticatoire, complexité du contact aliment – dent,…) et les propriétés physiques de l'aliment. Dans un souci de validation, nous avons adapté des méthodes expérimentales afin de produire des résultats nécessaires à la comparaison de ceux issus de ces modèles.

2. Démarche générale et division du mémoire :

La démarche est d'abord basée sur une modélisation par éléments finis (EF) pour étudier la propagation de fissures dans un produit à base d'amidon, pris comme aliment modèle (Figure 1).

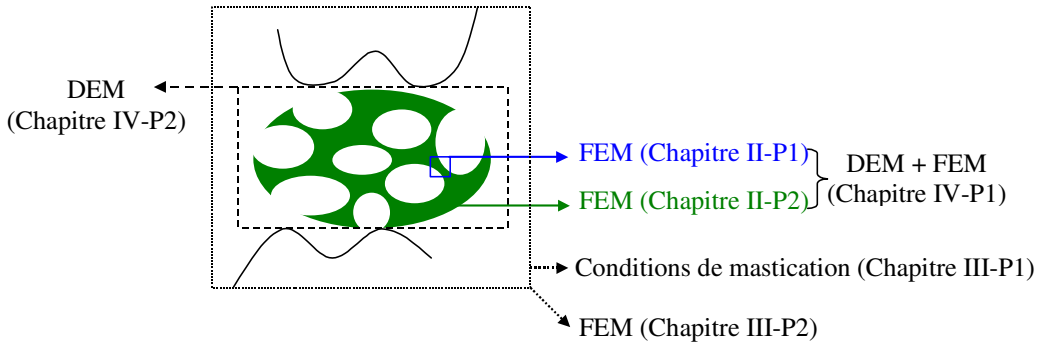

Figure.1. *Démarche de modélisation appliquée à la mastication humaine de produits céréaliers (EF et DEM).*

Cette approche permet de déterminer les critères physiques qui gouvernent la propagation de fissures dans les matériaux étudiés et de comprendre ainsi les propriétés de rupture. Cependant, par cette méthode, il est plus difficile de modéliser la fragmentation des produits. Pour palier à cette difficulté, la démarche est complétée par la modélisation par la méthode des éléments discrets (DEM). Par cette méthode, il est possible de décrire l'évolution du produit, en cours de compression, par des collections de grains de forme simple qui peuvent se fragmenter ou s'agglomérer. Les deux méthodes sont complémentaires parce que les critères physiques déterminés par EF peuvent être appliqués pour modéliser la fragmentation par la méthode DEM.

Cette démarche est développée suivant différentes étapes qui correspondent à cinq chapitres de la thèse :

- Le premier chapitre bibliographique présente les aspects généraux concernant la mastication humaine du point de vue physiologique, les propriétés rhéologiques des

aliments céréaliers et leur texture. Ensuite, sont rappelés les principes de base de la mécanique de la rupture et les différentes approches de modélisation existantes qui permettent de décrire la propagation de fissures dans les matériaux.

- Le deuxième chapitre concerne, pour une première partie, la modélisation par éléments finis de la propagation de fissures dans un matériau biopolymère dense à base d'amidon. Le critère de taux de restitution de l'énergie est introduit et les résultats de la simulation sont confrontés à des résultats expérimentaux obtenus à l'échelle macroscopique. Cette partie est entièrement constituée d'un article publié dans la revue Engineering Fracture Mechanics. Dans une deuxième partie de ce chapitre, le modèle présenté en première partie est appliqué à un matériau alvéolaire, de faible densité. Il s'agit d'un extrudé à base d'amidon, pour se rapprocher d'un aliment réel. Une étude expérimentale est menée en parallèle afin de valider les résultats numériques. Cette partie est entièrement constituée d'un article publié dans la revue Carbohydrate Polymers.
- Le troisième chapitre est d'abord consacré à des mesures physiologiques pour déterminer les conditions dynamiques de mastication, dans une première partie. A cette fin, une campagne d'essais a été réalisée par un sujet pour étudier, en collaboration avec l'INRA-Dijon, la dégradation de plusieurs aliments de type céréales petit-déjeuner, dont les caractéristiques morphologiques ont ensuite été déterminées par micro-tomographie RX (ESRF, Grenoble). Dans une deuxième partie de ce chapitre, la simulation de la compression en 3D de l'aliment entre deux dents par EF est présenté afin de prédire le comportement sous chargement complexe. Ce chapitre est présenté sous la forme de deux articles.
- Le quatrième chapitre est consacré à l'adaptation de la Méthode des Eléments Discrets (DEM) au contexte de la mastication humaine. Dans une première partie les données expérimentales acquises au deuxième chapitre sont utilisées pour modéliser le comportement du matériau dense à base d'amidon. Dans la deuxième partie de ce chapitre, la compression d'un aliment céréalier est modélisée par la DEM, en se basant sur sa structure réelle, déterminée au chapitre précédent. Ce chapitre est présenté sous la forme de deux projets d'article.
- Enfin dans un cinquième chapitre, nous rappellerons les principaux résultats obtenus pour en proposer une synthèse argumentée par rapport à la bibliographie avant de proposer, en conclusion, quelques perspectives que ce travail permet de dégager.

Chapitre I : Travaux antérieurs et étude bibliographique

Ce chapitre aborde les aspects suivants :

(1) Décrire les notions essentielles de la mastication, de la structure et des propriétés d'aliments céréaliers.

(2) Récapituler les notions essentielles de la mécanique de la rupture.

(3) Présenter les méthodes numériques utilisées pour modéliser la propagation de fissures dans les matériaux.

1. La mastication et les aliments solides :

1.1. La mastication

La mastication est la première phase de la digestion, c'est un processus physique qui fait appel aux muscles de la mâchoire. Les aliments contenus dans la cavité buccale sont écrasés, mélangés à la salive et lubrifiés. Ces transformations facilitent considérablement leur assimilation par le reste du système digestif. Pendant la mastication d'un aliment solide, la taille des particules constituant le bol alimentaire est réduite. Plusieurs facteurs déterminent le résultat de la mastication (Figure 2). La mastication est réalisée par un système qui comprend différentes structures anatomiques telles que les muscles masticateurs, l'articulation temporo-mandibulaire, les dents, la langue, les tissus mous de la cavité buccale, la mandibule et le maxillaire supérieur. La mandibule est capable de se déplacer en relation avec le crâne; son mouvement est guidé par deux articulations temporo-mandibulaires et par les contractions des muscles masticateurs. Les muscles sont les principaux déterminants du mouvement de la mâchoire. Les dents forment la zone occlusale où les particules d'aliments sont fragmentées. La fragmentation dépend :

- de la superficie totale d'occlusion et donc du nombre de dents antagonistes ;
- de la force maximale qui est fonction du volume musculaire, de l'activité musculaire de la mâchoire et de la coordination entre les différents muscles ;
- du mouvement de la mâchoire ;
- de la façon dont la langue et les joues mettent en mouvement les fragments de nourriture entre les dents ;
- de la structure et les propriétés mécaniques de l'aliment ;
- enfin, d'une production suffisante de salive, indispensable pour une bonne mastication, en vue de la première dégradation enzymatique de l'aliment.

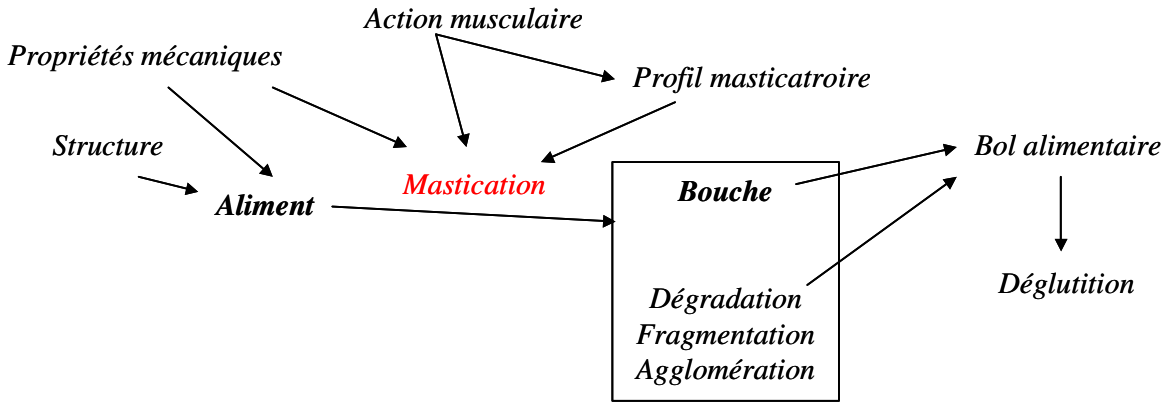

Figure 2. *Processus de la mastication Humaine.*

1.1.2. Caractéristiques de la fragmentation

La distribution des fragments d'aliments peut être obtenue par un processus physique de tamisage [1], ou par des technique d'analyse d'images du bol alimentaire [2] . La figure 3 présente la probabilité de sélection des particules fragmentées en fonction de leur taille [1]. Cette probabilité de sélection est donnée par une loi puissance:

$$S(X)=C\ X^{a} \qquad (1)$$

où C et a sont des constantes à déterminer pour chaque individu, X est la taille de la particule.

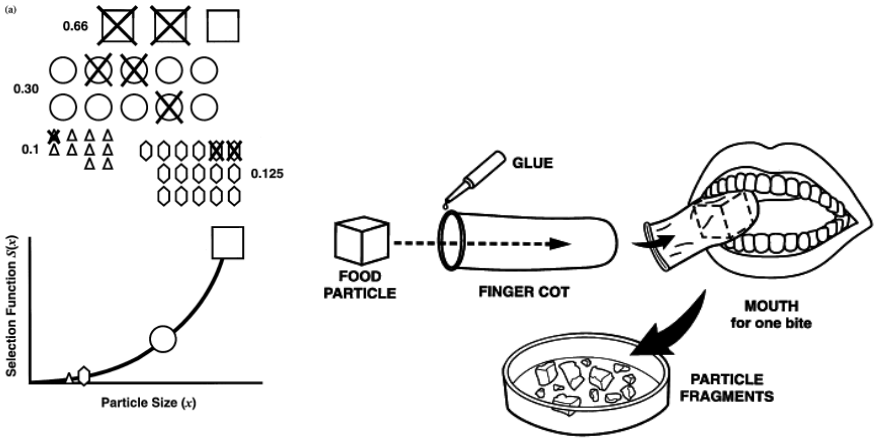

Figure 3 . *illustration de la sélection de fragments dans un modèle probabiliste de mastication [1].*

Le modèle de fragmentation s'appuie sur deux notions :

- la probabilité de sélection d'un fragment,
- le degré de fragmentation de ce dernier.

La première notion s'appuie sur le rôle prédominant de la langue [1], alors que le seconde s'appuie sur des principes de la mécanique de la rupture qui font intervenir deux autres

concepts: la géométrie du chargement et la propriété mécaniques de l'aliment. Si on considère que l'essentiel de la fragmentation se produit lors des derniers instants de l'occlusion, alors la fragmentation reste modérée au regard de la distance restante parcourue par les dents.

1.1.3. Profil masticatoire

La mastication est accomplie grâce à des mouvements mandibulaires rythmiques dans les trois dimensions de l'espace. Ces derniers permettent la fragmentation et l'écrasement de l'aliment entre les dents, associés à des mouvements coordonnés de la langue, des joues et des lèvres qui assurent le transport, la formation et le contrôle du bol alimentaire. Différents moyens sont utilisés pour étudier les mouvements mandibulaires, comme l'observation directe du point interincisif ou du menton, les enregistrements graphiques, les photo-graphiques, vidéographiques, radiographiques. Plus récemment, la cinéfluorographie et la vidéofluorographie ont permis de mieux connaître les mouvements. Chaque fois que le point interincisif mandibulaire revient à sa position initiale, la mandibule a effectué un cycle masticateur. Le mouvement d'ouverture et de fermeture des mâchoires permet d'établir le profil masticatoire (Figure 4a).

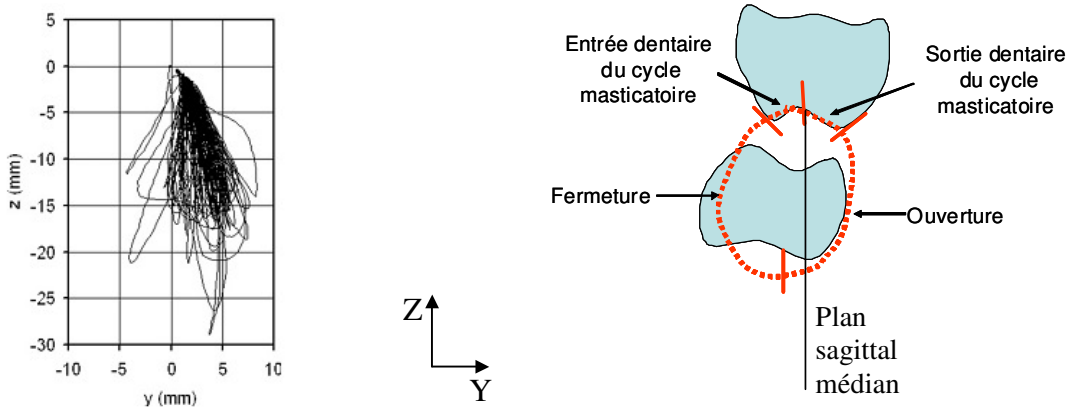

(a) (b)

Figure 4. *(a) Illustration de profils masticatoires [3]. (b) Divisions d'un cycle masticateur en différentes phase selon Lauret et le Gall [4]*

Les mouvements fonctionnels ne couvrent qu'une faible partie de l'enveloppe des mouvements limites. Selon les auteurs et les populations étudiées, l'amplitude moyenne du déplacement du point interincisif mandibulaire est :

- comprise entre 16 mm et 22 mm dans le sens vertical [4, 5];
- comprise entre quelques millimètres et 1 centimètre dans le sens transversal [4-6];

- dans le sens sagittal, est de 6 mm environ [7].

L'ouverture maximale est influencée par la taille de l'aliment à mastiquer [8, 9].

Ce profil traduit la trajectoire mandibulaire. Il varie d'un cycle de mastication à un autre en fonction de l'état de dégradation de l'aliment. Il varie aussi d'une dent à une autre et d'un individu à l'autre [3]. Selon les auteurs et l'aspect de la mastication qu'ils privilégient, ces cycles se caractérisent par une grande activité des muscles élévateurs et peuvent être divisés en trois phases [4] (Figure 4b):

- une phase d'ouverture, régulière et rapide chez l'homme ;
- une phase de fermeture rapide jusqu'au contact avec l'aliment ;

une phase de fermeture lente caractérisée par l'écrasement de l'aliment (phase de puissance ou « power stroke »).

- Une phase d'occlusion.

1.1.4. Etude physiologique de la mastication

L'étude physiologique s'intéresse aux activités motrices nécessaires pour mettre l'aliment dans un état compatible avec la déglutition. Ces activités sont principalement liées aux muscles des joues et de la langue. Ces muscles ramènent constamment la nourriture entre les deux rangées de dents, ce qui permet de maximiser le contact aliment-dent pour un meilleur rendement mécanique de la mastication. La force musculaire développée est adaptée à la dureté de d'aliment. Par exemple, la mastication des carottes ou de la viande requièrent environ 70-150N [10] alors que la force maximale pour un humain est d'environ 500-700N [11]. Ces forces sont estimées grâce notamment à l'électromyographie (EMG). L'EMG est une mesure indirecte des courants électriques qui accompagnent l'activité musculaire [12, 13]. L'analyse des signaux EMG montre également que, dans certains produits céréaliers, la force moyenne augmente au cours des premiers cycles, puis décroît brutalement entre 7 et 10 cycles et enfin diminue modérément jusqu'à ce que le point de la déglutition soit atteint [2]. Ces mesures mettent en évidence le rôle du comportement mécanique de l'aliment [14]. En outre, des mesures d'EMG effectuées sur des produits de même type et même composition (céréales petit-déjeuner) ont montré que des propriétés mécaniques différentes conduisaient à des caractéristiques masticatoires significativement différentes. La mastication, à laquelle contribuent les dents et la langue,grâce à ses muscles, mélange les aliments à la salive produite par les glandes salivaires : le mélange obtenu est appelé "bol alimentaire". La salive humidifie et lubrifie les aliments afin de faciliter la déglutition, avec un flux d'environ

0,5mL/min en conditions non stimulées et de 2 à 4 mL/min en conditions stimulées, lors de la mastication notamment [15].

1.1.5. Masticateurs artificiels

Plusieurs équipes de recherche se sont intéressées à la biomécanique de la mastication. Pour éliminer la grande variabilité interindividuelle, ils ont appliqué la robotique à la mastication afin de simuler certaines fonctions de la mastication humaine [3]. Ces robots comprennent en général :

- une partie fixe correspondant au maxillaire (mâchoire supérieure),
- une partie mobile correspondant à la mandibule (mâchoire inférieure),
- une articulation temporo-mandibulaire assurant la liaison entre les mâchoires (joints).

Des exemples de simulateurs sont illustrés dans la Figure 5. Les simulateurs de mastication peuvent être classés en trois catégories :

Modèles statiques : ce sont les modèles qui permettent l'étude de la déformation des mandibules sous de petites charges [13] et/ou l'étude des forces musculaires et leur incidence sur les fonctions de mastication.

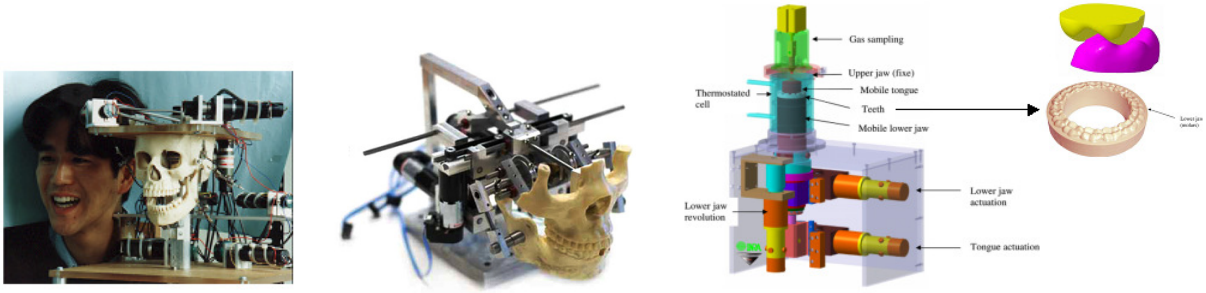

(a) (b) (c)

Figure 5. *(a) Robot permettant d'étudier le mouvement des mâchoires et les forces durant la mastication [3]. (b) Configuration permettant la simulation de mouvements complexes de mâchoires. [3] (c) Simulateur permettant de mesurer les forces de mastication sur les produits alimentaires [16] .*

Modèles dynamiques : dans ces modèles, les forces de mastication et le mouvement des mâchoires sont utilisés comme entrées pour étudier les différentes fonctions en rapport avec la mastication humaine [17-19]. Le simulateur de la Figure 5c correspond à cette catégorie.

Modèles cinématiques : ces modèles intègrent plus de complexité dans la description du mouvement des mandibules [20]. Les deux exemples montrés en Figure 5a et 5b font partie de ce type de modèle.

2. Structure et propriétés mécaniques des matériaux à base de biopolymères et des aliments céréaliers

Les biopolymères sont des polymères d'origine biologique, donc issus d'organismes vivants. Ils comprennent notamment des glucides et des protéines. L'amidon est un exemple de macromolécule glucidique. C'est la forme majeure d'accumulation des glucides dans les tissus végétaux. L'amidon est un polymère constitué de glucose. Les tissus animaux en sont dépourvus. Ce polymère de glucose est stocké dans les graines et tubercules de différentes plantes d'intérêt agronomique telles que céréales (blé, maïs, riz…), pomme de terre, manioc, pois, qui en contiennent 50 à 80% en base sèche ; il représente la principale source d'énergie de l'alimentation humaine, mais est également utilisé dans un grand nombre d'applications industrielles (agrochimie, papeterie, industrie textile…) [21].

2.1. Structure de l'amidon

L'amidon est stocké dans des grains semi-cristallins, insolubles, de diamètre allant de 1 µm à plus de 50 µm, et de densité comprise entre 1,4 et 1,5 g/cm^3. Il se compose de deux types de polymères : l'amylose et l'amylopectine, ce dernier polymère étant généralement le plus abondant (60 à 70 %). L'amylose représente 15 à 30% de la masse de l'amidon. C'est un polymère linéaire de résidus glucose liés par une liaison α-(1,4)-D-glucosidique. Cette longue chaîne prend la forme d'une hélice (6 résidus de glucose par tour d'hélice), stabilisée par des liaisons hydrogène entre les groupements hydroxyle et les molécules d'eau (Figure 6). L'amylopectine diffère de l'amylose car il s'agit d'un polymère ramifié. (Figure 6).

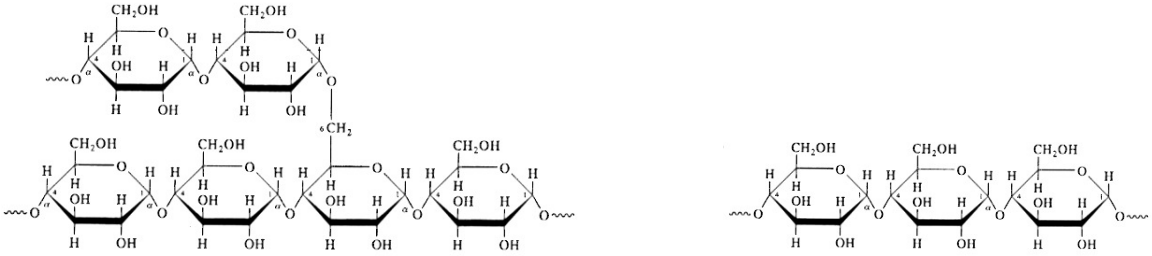

(a) (b)

Figure 6. *Structures de (b) l'amylose et de (a) l'amylopectine.*

Lors de la fabrication d'aliments, notamment à base de céréales (pain, céréales petit-déjeuner…), l'amidon contenu dans la farine, additionnée d'eau et d'autres ingrédients (sucre, matières grasses…) est soumis à des traitement thermomécaniques plus ou moins intenses

(cuisson, extrusion…); il perd ainsi sa structure granulaire semi-cristalline native, et se trouve alors à l'état amorphe, ce qui le rend digestible. La température de transition, qui dépend de la teneur en eau, elle est de l'ordre de 75°C pour une teneur en eau de 50% (base totale), et d'environ 125°C à 20% d'eau.

2.2. Comportement mécanique des produits à base d'amidon

Les propriétés mécaniques d'un matériau polymère dense sont dépendantes de :

- la cristallinité (ou taux de cristallinité), qui correspond au pourcentage en poids de la phase cristalline dans le matériau. Les cristaux ont une résistance chimique beaucoup plus élevée que la phase amorphe du même matériau.

- la température de transition vitreuse (Tg) qui correspond à la température à laquelle le polymère passe de l'état vitreux à l'état caoutchoutique. Dans l'état vitreux (températures basses), les mouvements intermoléculaires (glissements des chaînes) sont bloqués. Dans l'état caoutchoutique, les mouvements intermoléculaires sont possibles. La température de transition vitreuse Tg dépend donc de la rigidité de la chaîne polymère (une chaîne rigide aura une Tg haute, une chaîne souple aura une Tg basse), de la taille des groupes latéraux (des groupes latéraux grands vont être des obstacles au glissement des chaînes et donc donner un polymère de haute Tg) et la force des interactions intermoléculaires (des interactions fortes donnant une haute Tg) [22].

- le taux de réticulation correspond à la densité de liaisons pontales entre les chaînes. La présence des liaisons covalentes entre les chaînes (polymères thermodurcissables) donne lieu à des propriétés différentes de celles des polymères purement linéaires (matériaux thermoplastiques) dont les seules liaisons intermoléculaires sont des liaisons faibles (Van der Waals, ponts hydrogène etc.). Les thermoplastiques peuvent être fondus puis re-solidifiés alors que les thermodurcissables se décomposent à haute température mais ne fondent pas.

Les travaux sur l'amidon et ses transitions thermiques, à faible teneur en eau, ont montré que l'amidon peut être considéré, en première approche, comme un matériau thermoplastique. A faible teneur en eau ($\leq$ 10% en base totale), la valeur de sa densité est proche de celle de l'amidon natif.

Le comportement de l'amidon amorphe dépend donc de la température, mais aussi de la teneur en eau. La température de transition vitreuse, qui délimite les deux états, vitreux et caoutchoutique, permet de distinguer respectivement deux comportements : élastique et fragile d'une part ou visco-élastique et ductile d'autre part.

Le comportement mécanique de l'amidon dense dans l'état vitreux est de type fragile. A température ambiante, sa teneur en eau est inférieure à 12%. Le module de Young est de l'ordre du GPa alors que la déformation à la rupture est de quelques % [23] –(Figure 7).

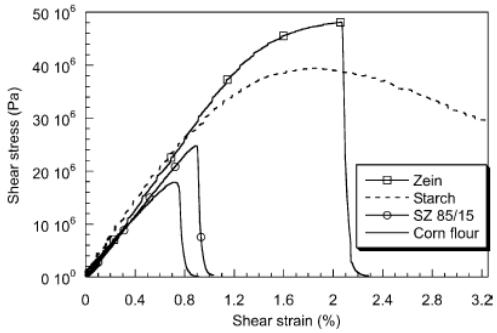

Figure 7. *Courbe contrainte/déformation, rupture à faible déformation, dans le domaine élastique [23].*

En raison de leur intérêt pratique, les produits transformés à base d'amidon, notamment les céréales petit-déjeuner extrudées, ont fait l'objet de nombreuses études ; leur comportement mécanique est décrit dans plusieurs travaux [23-29], dans la mesure où il détermine leur texture, qui est un des attributs sensoriels, important pour le consommateur. Ils peuvent être considérés comme des mousses solides, ou cellulaires, dont les parois sont constituées d'un mélange de biopolymères essentiellement constitués d'amidon amorphe. Outre les propriétés mécaniques intrinsèques du matériau constitutif des parois, leurs propriétés mécaniques sont fonctions de la densité relative [30], et de la distribution de taille des cellules ou alvéoles et des parois [24]. La modélisation mécanique par éléments finis a récemment permis de montrer que la rigidité des mousses solides était d'autant plus élevée que leur structure cellulaire était hétérogène.

Notre démarche dans cette thèse consiste donc à étudier d'abord l'amidon amorphe pris comme matériau dense, ou dense, à base de biopolymère, puis l'amidon transformé considéré comme matériau cellulaire, et pris comme modèle de céréales petit-déjeuner extrudées, dont le comportement lors de la mastication est finalement abordé. La teneur en eau des produits choisis est très faible ($\leq$5%, bh) et que Tg >> 37°, cette teneur en eau va augmenter assez peu par addition de salive. Par conséquent le matériau reste fragile pendant les premiers cycles de mastication ce qui justifie d'étudier la rupture fragile.

3. Mécanique de la rupture

La mécanique de la rupture est dédiée à l'application des principes de la mécanique en présence de discontinuités: fissure ou défaut. Elle permet entre autres de décrire la physique de la propagation de fissures connaissant la dimension des défauts et les conditions de sollicitation [31].

Les modes de fissuration impactant la mastication sont complexes. Pour préparer l'étude de la fissuration, il convient de rappeler quelques éléments de la théorie de la rupture en milieu homogène.

4. Description générale de la mécanique de la rupture

Le modèle de la fissuration intègre la géométrie de la fissure ainsi que son "mode de propagation". Si les fissures sont planes et se propagent dans leur plan, l'état général de la propagation se limite à la superposition de trois modes (Figure 8) [32] :

- **modes I** (ouverture) : les lèvres de la fissure se déplacent dans des directions opposées et perpendiculairement au plan de la fissure ;
- **modes II** (cisaillement plan) : les lèvres de la fissure se déplacent dans le même plan et dans une direction perpendiculaire au front de fissure ;
- **modes III** (cisaillement anti-plan) : les lèvres de la fissure se déplacent dans le même plan et dans une direction parallèle au front de la fissure.

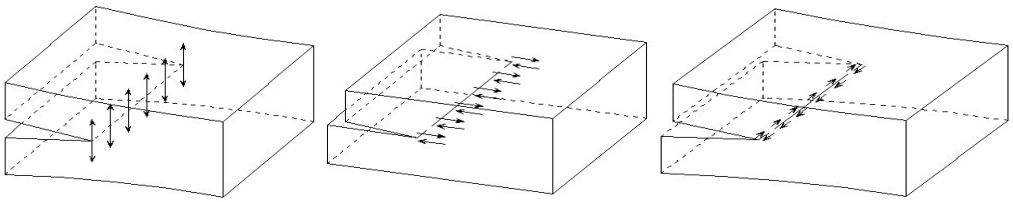

Mode I *Mode II* *Mode III*

***Figure 8**. Les trois modes de propagation de fissure [32].*

Le cas réel est une superposition de ces modes, on parle alors de mode mixte. L'objet de la mécanique de la rupture est l'étude des évolutions du front de la fissure en fonction des chargements appliqués et des caractéristiques du matériau au moyen des trois grandeurs [32] :

- K_c : le facteur d'intensité de contrainte critique,
- G_c : le taux de restitution d'énergie,
- γ : le taux de dissipation par unité d'accroissement de la fissure.

On considère le cas plan, l'axe OX dans le prolongement de la fissure et OY perpendiculairement à la fissure (figure 9)

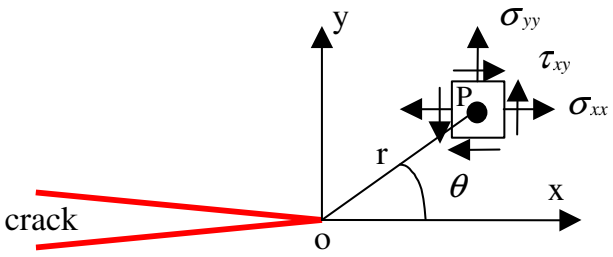

Figure 9. *Définition des axes (x,y) et des cordonnées (r, θ) au voisinage du font d'une fissure [33].*

Dans un cas bidimensionnel, en négligeant la déformation plastique , le champ de contraintes au voisinage du fond de la fissure peut s'exprimer de la manière suivante [33] :

$$\sigma_{ij}(r,\theta) = \frac{K}{\sqrt{2\pi r}} f_{ij}(\theta) + O(r) \qquad (5)$$

r et θ étant les cordonnées polaires du point P considéré (Figure 9) par rapport au fond de la fissure. $f_{ij}(\theta)$ est une fonction de l'angle polaire θ par rapport à l'extrémité de la fissure qui se rapporte à la contrainte σ_{ij} considérée ; $O(r)$ rassemble les termes du développement qui tende vers 0 avec r.

Au voisinage immédiat du fond de la fissure, les contraintes présentent une singularité en $\frac{1}{\sqrt{r}}$, c'est-à-dire que lorsque $r \to 0$, leur valeur tend vers l'infini.

Les autres termes d'ordre plus élevé de la relation (1.5) deviennent alors négligeables. La zone la plus critique est donc le voisinage immédiat du fond de la fissure. L'équation précédente s'écrit alors [32] :

$$\sigma_{ij} = \frac{K}{\sqrt{2\pi r}} f_{ij}(\theta) \qquad (6)$$

K est le facteur d'intensité des contraintes qui prend une des valeurs K_I , K_{II} ou K_{III} selon le mode de chargement de la fissure. K est le produit d'une contrainte par la racine carrée d'une longueur, il est exprimé en MPa.m$^{1/2}$. Les champs de contraintes s'expriment à l'aide des facteurs d'intensité des contraintes K_I , K_{II} et K_{III} par les relations suivantes [34]:

$$\sigma_x = \frac{K_I}{\sqrt{2\pi r}}\left(1-\sin\left(\frac{\theta}{2}\right)\sin\left(\frac{3\theta}{2}\right)\right)\cos\left(\frac{\theta}{2}\right) + \frac{K_{II}}{\sqrt{2\pi r}}\left(2+\cos\left(\frac{\theta}{2}\right)\cos\left(\frac{3\theta}{2}\right)\right)\sin\left(\frac{\theta}{2}\right)$$

$$\sigma_y = \frac{K_I}{\sqrt{2\pi r}}\left(1+\sin\left(\frac{\theta}{2}\right)\sin\left(\frac{3\theta}{2}\right)\right)\cos\left(\frac{\theta}{2}\right) + \frac{K_{II}}{\sqrt{2\pi r}}\cos\left(\frac{\theta}{2}\right)\cos\left(\frac{3\theta}{2}\right)\sin\left(\frac{\theta}{2}\right)$$

$$\sigma_{xy} = \frac{K_I}{\sqrt{2\pi r}}\cos\left(\frac{\theta}{2}\right)\cos\left(\frac{3\theta}{2}\right)\sin\left(\frac{\theta}{2}\right) - \frac{K_I}{\sqrt{2\pi r}}\left(1-\sin\left(\frac{\theta}{2}\right)\sin\left(\frac{3\theta}{2}\right)\right)\cos\left(\frac{\theta}{2}\right) \qquad (7)$$

Le taux de restitution d'énergie G, représente l'énergie nécessaire pour faire progresser la fissure d'une longueur unité. Elle correspond à la décroissance de l'énergie potentielle totale *Wp* pour passer d'une configuration initiale avec une longueur de fissure *a*, à une autre où la fissure s'est propagée d'une longueur *da* :

$$G=-\frac{\partial W_p}{\partial A} \tag{8}$$

L'énergie potentielle totale peuvent être décomposée en deux parties:

$$W_p = W_e + W_{ext} \tag{9}$$

où $W_e = \int_\Omega \sigma : \varepsilon$ représente l'énergie de déformation élastique, $W_{ext} = \int_\Omega f.u$ est l'énergie potentielle des forces extérieures *f*, et ∂A l'incrément de surface correspondant à l'extension de la fissure. En utilisant le champ des contraintes dans la zone singulière et la loi de comportement élastique linéaire, il est possible de relier le taux de restitution d'énergie aux facteurs d'intensités de contraintes par :

$$G=\frac{K_{III}^2}{2\mu}+\frac{\left(K_I^2+K_{II}^2\right)}{E'} \tag{10}$$

Avec $E=E'$ en contraintes planes, et $E'=E/\left(1-\nu^2\right)$ en déformations planes ; E est le module d'Young, ν est le coefficient de Poisson du matériau, et $\mu=E/2(1+\nu)$ est le module de cisaillement du matériau.

5. Propagation de la fissure selon le type de matériau

La propagation de la fissure est sensible au type de comportement du matériau étudié. Pour un matériau fragile, ce dernier subit une rupture brutale par la propagation « catastrophique » d'une fissure. Il existe une relation donnant la vitesse de propagation dans un tel matériau

$$Vc=\sqrt{\frac{E}{\rho}} \tag{11}$$

E *:* module d'Young , ρ masse volumique.

Dans le cas de l'amidon vitreux, de densité = 1,43 g/cm^{3}et de module E=2,5 GPa, la valeur théorique de la vitesse est $Vc \approx 1{,}32 km/s$.

Pour décrire la propagation de fissure, la prise en compte du phénomène de rupture est cruciale. Il existe deux types de rupture : ductile ou fragile, selon que le matériau présente ou non un phénomène de plasticité accompagnant la rupture. Le tableau 1 résume les différences entre la rupture fragile et la rupture ductile

Tableau 1 : Caractéristiques de la rupture ductile et de la rupture fragile

Caractéristiques d'une rupture fragile	Caractéristiques d'une rupture ductile
Comprend peu ou pas de déformation du matériau.	D'abord, on observe un processus de déformation au cours duquel le matériau se déchire lentement avec une grande dépense d'énergie.
La propagation de fissures est rapide (environ 2000 m/s). La rupture fragile n'est possible que lorsque les fissures se propagent à des vitesse élevées.	La propagation de fissures est un processus lent. On observe une déformation plastique importante avant et pendant la propagation des fissures.
La propagation de la fissure confère à la surface de rupture un aspect brillant et lisse. Elle peut s'accompagner d'autre instabilité comme les réseaux de fissures	La fissure se propage avec un faciès rugueux

Pour un matériau cellulaire, la propagation de la fissure est plus complexe. Elle dépend de l'hétérogénéité du matériau, notamment la présence de cellules dont les bords représentent des concentrateurs de contraintes [35]. On ne peut pas parler de propagation si la taille du défaut (préfissure) est du même ordre de grandeur que la taille des cellules.

6. Critères de propagation brutale de la fissure

L'expérience montre que la propagation brutale de la fissure intervient lorsque l'énergie de Griffith, G, atteint une valeur critique notée G_c. Pour les matériaux fragiles, en considérant le seul mode I de fissuration et en supposant un état de déformations planes, Griffith prend pour valeur critique l'énergie nécessaire pour créer des surfaces supplémentaires dans le matériau, soit :

$$G_c = 2\gamma_s \qquad (12)$$

γ_s étant la densité d'énergie superficielle.

La valeur G s'exprime en J/m^2 ou en N/m, et parfois appelée force d'extension de la fissure ou taux de restitution d'énergie.

Pour les matériaux métalliques, dont la rupture s'accompagne d'une forte déformation plastique en fond de fissure, le critère de Griffith est modifié par :

$$G_{IC} = 2\gamma_s + \gamma_p \qquad (13)$$

γ_p étant l'énergie de déformation plastique par unité de surface : γ_p est très grand par rapport à γ_s, le rapport pouvant atteindre 1000.

La valeur critique G_c correspond à une valeur d'intensité de contraintes notée *Kc*. Dans le cas général, on a :

$$G_C = \frac{K_{IC}^2 + K_{IIC}^2}{E'} + \frac{K_{IIIC}^2}{2\mu} \qquad (14)$$

Avec $E' = E$ en contraintes planes et $E' = E/(1-\nu^2)$ en déformation planes.

La valeur critique K_C, appelée ténacité, est caractéristique du matériau et du mode de chargement. Il y a rupture lorsque le paramètre K atteint la valeur critique K_C. Le mode I étant le plus endommageant, c'est la valeur critique K_{1C} qui est généralement utilisée pour caractériser les matériaux. Le tableau 2 donne quelques exemples de données expérimentales sur la ténacité de certains matériaux [36].

L'épaisseur influe sur l'état de contraintes. Pour des éprouvettes de faible épaisseur (plaques), chargées en mode I dans leur plan, l'état de contraintes planes est prédominant et la valeur critique du facteur d'intensité de contraintes en mode I est élevée notamment pour les matériaux ductiles. Lorsque l'épaisseur augmente, on observe une transition vers un état de déformations planes. Le facteur d'intensité de contraintes critique diminue et n'évolue plus au delà d'une certaine épaisseur : c'est cette valeur minimale stabilisée du K_{1C} qui définit la ténacité du matériau (Figure 10). On note, cependant, que dans matériau massif dont la fissure de débouche sur les surfaces la valeur du facteur d'intensité de contraintes en chaque point du font évolue dépendant de sa proximité à la surface du fait de la transition de l'état de contraintes planes à l'état de déformations planes.

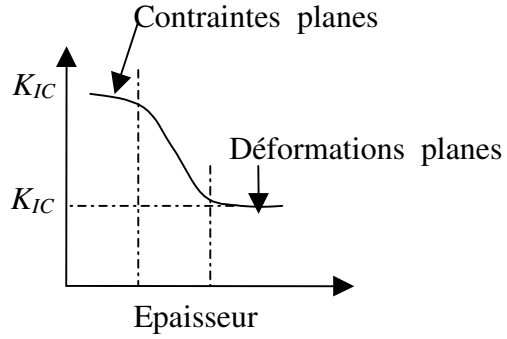

***Figure 10**. Variations caractéristiques de la ténacité K_{IC} [31].*

Tableau 2. La ténacité mesurée de quelques matériaux [36].

Matériel	La ténacité ($MPa\,m^{1/2}$)
Acier doux	140
Alliages de titane	55 – 120
acier au carbone	30
Nickel, cuivre	> 100
Béton armé	10 – 15
Béton non armé	0.2
Roches, verre	1
Céramiques (alumine, SiC)	3 – 5
Nylon	3
Polyester	0,5
Chips (pomme de terre)	0,12

7. Méthodes numériques utilisées pour la modélisation numérique de propagation de fissures

La simulation numérique de propagation de fissures a fait l'objet de nombreux travaux depuis une trentaine d'années, conjointement à des essais expérimentaux, afin de mieux approcher les critères de rupture. Cependant, les problèmes liés à la simulation ainsi que les difficultés rencontrées dans la mise en oeuvre des expériences rendent encore ce sujet d'actualité. D'un point de vue numérique, le principal obstacle reste le suivi de la fissure au cours du temps notamment en 3D.

7.1. Méthodes basées sur les éléments finis

La modélisation numérique par élément finis est largement répandue dans la recherche scientifique et industrielle. Etudier le comportement mécanique d'une structure, par la méthode des éléments finis, consiste d'abord à effectuer une discrétisation géométrique. La structure est subdivisée en sous-domaines de forme géométrique simple appelés « éléments finis » interconnectés en des points appelés « nœuds ». A chaque élément est associé une loi de comportement qui relie souvent la contrainte à la déformation. On parle aussi de définition de paramètres mécaniques ; l'approximation de la solution (déplacements, contraintes) est définie non pas sur l'ensemble de la structure mais pour chacun de ses éléments, en convertissant le systèmes de relâchements en une forme matricielle adéquate (matrice globale) avant résolution par des technique d'inversion.

La modélisation numérique par éléments finis est un outil puissant pour étudier les comportements des matériaux sous chargements simple. Dans la suite du texte, nous

présentons les modèles numériques existants pour la simulation de la propagation de la fissure, sans rentrer dans le détail de la méthode des éléments finis.

Découplage des degrés de liberté

Cette méthode consiste à modifier la connectivité des nœuds en se basant sur un critère de découplage des nœuds. On en déduit la nouvelle position du front de la fissure comme le montre la figure 11.

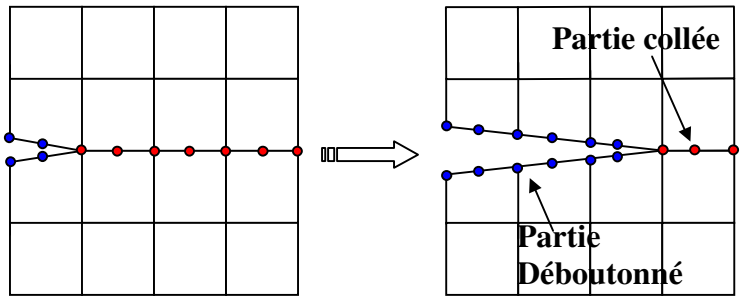

Figure 11. *Méthode de relâchement de nœud*

Dans le cas des fissures sollicitées en mode I, le trajet de la fissure est entièrement connu puisque il est rectiligne. La discrétisation du trajet est alors entièrement dépendante de la taille de maille utilisée le long de celui-ci. La technique employée couramment est celle dite du déboutonnage ou relâchement de nœuds [37, 38]. La création de discontinuité est facile avec cette méthode sauf que l'on échappe pas la sensibilité des résultats vis à vis des maillage. Il faut aussi envisager des éléments adéquates afin de déterminer, par exemple, les facteur d'intensités de contraintes sans recourir à maillage centré autour de la fissure.

Remaillage

Pour avoir une bonne idée des champs à proximité du front de la fissure, il faut conserver un maillage concentré et suffisamment fin autour du front de la fissure. Le remaillage a été utilisé à cette fin dans plusieurs travaux [39, 40]. A un pas de temps donné, l'opération de remaillage nécessite de projeter les champs de la solution du pas précédent sur le nouveau maillage. Cette méthode conduit à un déséquilibre des champs lorsque les solutions discrétisées ne sont pas les mêmes pour les maillages successifs. Cette difficulté devient insurmontable quand les champs en questions dépendent de l'historique de chargement (ex. comportement visqueux) La Figure 12 illustre le principe du remaillage dans le cas d'une fissure qui interagit avec un trou [41].

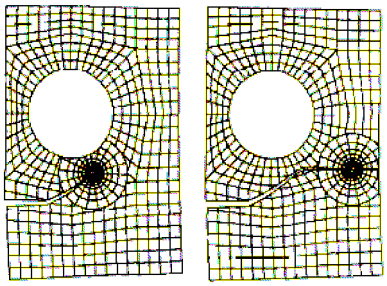

Figure 12. *Méthode de remaillage appliquée à la progression d'une fissure à proximité d'un trou [41].*

Elimination d'éléments (Element deletion method)

Cette méthode consiste à éliminer des éléments satisfaisant un critère de rupture donné. Cette méthode, simple à mettre en œuvre, impose une perte de matière. Elle est plus adaptée à des problèmes d'usure qu'à la propagation de fissures (Figure 13). La méthode est néanmoins souvent utilisée pour les problèmes de propagation de fissures comme le montre la figure 14. Elle présente l'inconvénient de surestimer la concentration de la contrainte [42]. Ce principe a été appliqué dans le cas de l'étude de fissure dans une molaire humaine sous sollicitation [43].

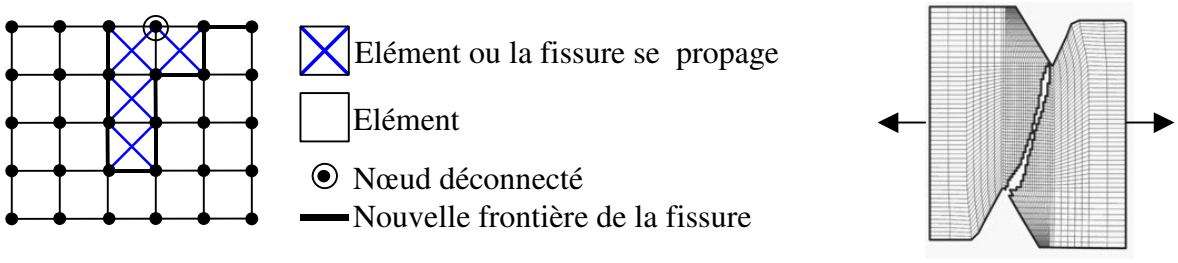

Figure 13. *Méthode d'élimination d'éléments appliquée à l'usinage [42].*
(a) diagramme élimination d'éléments . (b) propagation de la fissure.

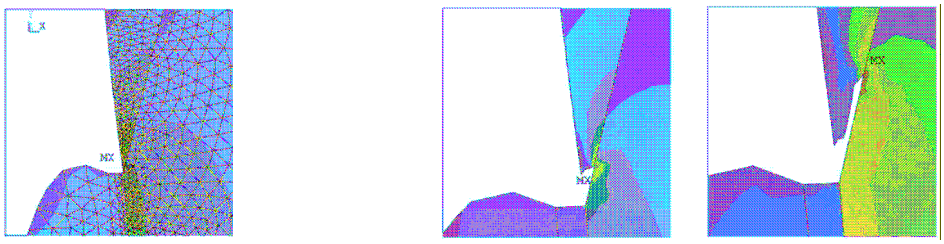

Figure 14. *Méthode d' élimination d'éléments appliquée à l'étude de lésions dentaires [43] :*
(a) Maillage. (b) propagation de la fissure.

Eléments cohésifs

Ce modèle s'appuie sur la séparation des éléments en mettant en œuvre un modèle cohésif. Les lois cohésives sont plus connues pour modéliser l'endommagement localisé. Cette méthode possède néanmoins quelques inconvénients. Elle introduit un élément d'épaisseur nul de rigidité finie qui modifie la rigidité globale de la structure. De plus, pour des raison de coût en élément, le trajet de la fissure doit être connu pour enrichir la partie du maillage concernée par la propagation. Donc l'intérêt dans ce type d'approche est plus de calculer grandeurs associées à une propagation prescrite, c-a-d dont on connaît par avance le trajet.

Plusieurs auteurs ont employé des modèles cohésifs. Les travaux de Needleman font référence à l'interface est le premier à utiliser des fonctions de types polynomial et exponentiel pour décrire la relation traction-séparation ($t - \Delta$) [44] (Figure 15). Tvergaard a appliqué le modèle cohésif pour décrire le rôle de la plasticité dans la résistance à la propagation de la fissure [45]. Camacho et Ortiz ont développé un modèle cohésif pour étudier le propagation de multiples fissures dans des directions arbitraires dans des matériaux fragiles [46].

Geubelle et Baylor ont utilisé une relation bilinéaire de traction-séparation appliquée aux problèmes de fissuration de la matrice et aux problèmes du délaminage dans les plaques composites stratifiées [47].

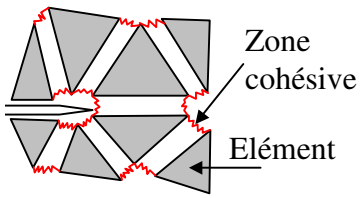

Figure 15. *Modèle de zones cohésives selon Xu–Needleman [48].*

7.2. Méthodes sans maillage

Méthodes des éléments frontière (Boundary element method)

La méthode des éléments de frontière est une formulation du problème local aux dérivés partielles en un problème sur la frontière du domaine où s'applique le problème, grâce à une intégration sur ce domaine [49]. Seules les lèvres sont discrétisées, ce qui est le principal avantage de cette méthode. Elle est tout particulièrement adaptée à l'étude des problèmes de fissuration en 3D pour des structures à géométrie complexe.

Dascheng et al., et Ortiz et al. ont étudié la propagation de la fissure par fatigue dans un matériau laminé et dans les aciers à comportement ductile, respectivement [50, 51].

Méthodes sans maillage

Les méthodes sans maillage sont basées sur un ensemble de nœuds répartis dans le solide sans requérir un maillage de celui-ci. Cette caractéristique en fait une méthode particulièrement utile pour résoudre les problèmes de grandes déformations et la rupture. On peut citer par exemple « Element-Free Galerkin Method ». Dans cette méthode, la description de la géométrie se fait uniquement à l'aide de nœuds sans recourir à la connectivité d'éléments (Figure 16). Elle a été développé par plusieurs auteurs dans le cas de la propagation de la fissure pour prendre en compte la discontinuité du matériau en utilisant cette approche [52-54].

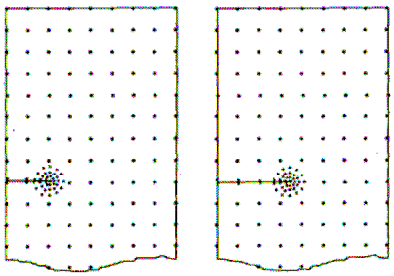

Figure 16. *Modèle sans maillage avec représentation de la géométrie par des nœuds [52].*

De par leur nature, ces méthodes sont très efficaces lorsque l'on traite les grandes déformations ou la fragmentation. A une échelle plus locale, la dynamique moléculaire est utilisée pour palier à la singularité de la contrainte au fond de la fissure. Son principe consiste à résoudre l'équilibre dynamique d'un grand nombre d'atomes définissant son comportement macroscopique à l'aide d'un potentiel quadratique. Dienes et Paskin ont utilisé cette technique pour simuler la propagation de la fissures en mettant en évidence le rôle du potentiel inter-atomique, les contrainte locales au front de la fissure et la vitesse de propagation [55].

7.3. Méthodes basées sur la partition de l'unité (partition of unity method)

La méthode de la partition de l'unité [56] est utilisée afin d'enrichir l'approximation en éléments finis classiques par des fonctions additionnelles, (i) discontinues pour les éléments traversés par la fissure pour représenter les discontinuités des champs de déplacement et (ii) discontinues pour les éléments contenant le front de la fissure pour caractériser le champ asymptotique en pointe de la fissure. La caractéristique de cette méthode est l'utilisation du maillage initial sans nécessité de se conformer à la géométrie de la fissure, sans raffinement ni remaillage au cours du propagation.

La méthode X-fem est basée sur ce concept. Elle permet de modéliser la présence d'un défaut (fissure ou autre) sans le mailler explicitement. Elle a été appliquée dans le cas de la rupture par fatigue [57, 58], la rupture fragile [59, 60] et pour des fissurations multiples [61].

7.4. Méthodes des élément discret (DEM)

La méthode des éléments discrets permet de tenir compte de la discontinuité et de l'hétérogénéité des matériaux granulaires. Elle est basée sur le principe de la dynamique moléculaire [62, 63], qui traite le matériau considéré comme un assemblage d'un grand nombre de particules en interaction. Les lois de contact définissent l'interaction entre deux particules, qui sont liées entre elles par un pont solide élastique. Les lois qui décrivent le critère de la propagation de la fissure seront explicitées dans le chapitre IV. La figure 17 présente la modélisation d'un processus de coupe à l'aide de la méthode des éléments discrets avec des particules sphériques [64]. Les particules rompues sont marquées avec une couleur différente. Des essais simples de traction et de compression, effectués sur la céramique [65], sont illustrées sur la figure 18. La méthode permet de retrouver les propriétés macroscopiques de la rupture, grâce à la connaissance à l'état microscopique.

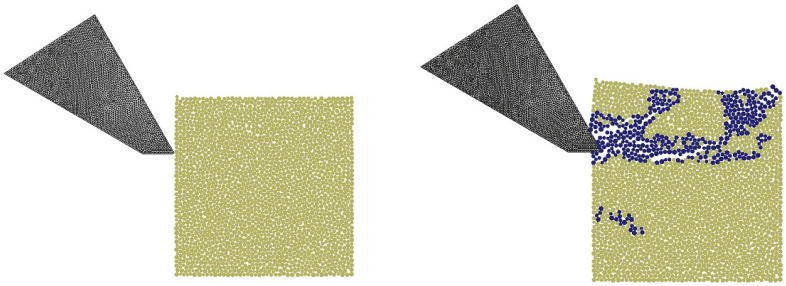

(a) (b)

Figure 17. *(a) configuration initiale de la géométrie, (b) fracturations d'une roche lors de la coupe [64].*

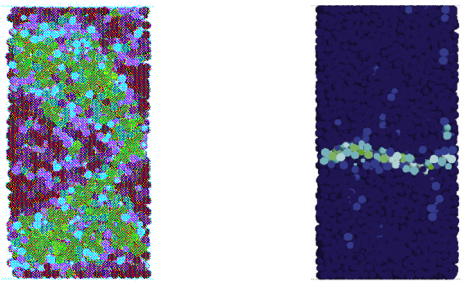

(a) (b)

Figure 18*. (a) Endommagement en compression, (b) Endommagement en traction [65].*

Les méthodes numériques utilisées pour simuler la propagation de fissure ne sont pas toutes équivalentes. Il semble que les méthodes classiques basées sur la méthode des éléments finis montrent certaines limites face à des méthodes plus enrichies ou les méthodes sans maillage. L'utilisation de zones cohésives est relativement difficile à mettre en oeuvre notamment afin de se prémunir de la dépendance au maillage, et surtout le risque élevé de distorsion de maillage. Dans ce contexte, les méthodes sans maillage sont une alternative attrayante, bien que leur usage reste peu répandu, notamment lorsqu'il s'agit d'interpréter physiquement les grandeurs associées aux paramètre internes du modèle.

References

[1] Lucas. PWP, J. F.Agrawal.,K. R.Bruce.,I. C. Food physics and oral physiology. Food Quality and Preference. 2002;13(4):203-213.

[2] Yven C, Guessasma S, Chaunier L, Della Valle G, Salles C. The role of mechanical properties of brittle airy foods on the masticatory performance. Journal of Food Engineering;101(1):85-91.

[3] Xu WL, Bronlund JE, Potgieter J, Foster KD, Röhrle O, Pullan AJ, Kieser JA. Review of the human masticatory system and masticatory robotics. Mechanism and Machine Theory. 2008;43(11):1353-1375.

[4] Lauret J, Le Gall M. La mastication, une réalité oubliée par l'occlusodontologie. Cah Prothese. 1994(85):30-46.

[5] Ahlgren J. Masticatory movements in man. In: Anderson DJ, Matthews B, editors Mastication Bristol: John Wright. 1976.

[6] Gillings B, Graham C, Duckmanton N. Jaw movements in young adult men during chewing. J Prosthet Dent. 1973(29):616-627.

[7] Proschel P, Hofmann M. Frontal chewing patterns of the incisor point and their dependence on resistance of food and type of occlusion. J Prosthet Dent. 1988(24):59-617.

[8] Mioche L, Hiiemae K, Palmer J. A postero-anterior videofluorographic study of the intra-oral management of food in man. Archs Oral Biol. 2002;80:47-267.

[9] Van Der Bilt A, Van Der Glas H, Olthoff L, Bosman F. The effect of particle size reduction on the jaw gape in human mastication. J DentRes. 1991;7:70-931.

[10] Anderson DJ. Measurements of stress in mastication. I. J, DentR. 1956;41:35-664.

[11] Gürsel O. A new device for measuring mastication force (Gnathodynamometer). Annals of anatomy ISSN 0940-9602 2002;184, n°4:pp. 393-396.

[12] B. May SS, M. Saltzman. A three-dimensional mathematical model of temporomandibular joint loading. Clin Biomech. 2001;16 (6):461–471.

[13] KOOLSTRAJ.H. A three-dimensional mathematical model of the human masticatory system predicting maximum possible bite forces. Journal of biomechanics. 1988;21, n°7:pp. 563-576

[14] GONZALEZ.R. The use of electromyography on food texture assessment = L'utilisation de l'électromyographie pour l'évaluation de la texture des aliments. Food science and technology international 2001;vol. 7, n°6: 461-471.

[15] Jehl-Pietri C, Monteil R, Madinier I, Raybaud-Diogene H, M. B. Sécheresse buccale, xérostomie et mesure de l'activité sécrétoire salivaire. Ann Med Interne. 1997;148:209-216.

[16] Salles C, Tarrega A, Mielle P, Maratray J, Gorria P, Liaboeuf J, Liodenot JJ. Development of a chewing simulator for food breakdown and the analysis of in vitro flavor compound release in a mouth environment. Journal of Food Engineering. 2007;82(2):189-198.

[17] J. Koolstr, T.M.van Eijden. The jaw open–close movements predicted by biomechanical modelling. J Biomech. 1997;30 (9):943–950.

[18] J.H. Koolstra , T.M.van Eijden. Dynamics of the human masticatory muscles during a jaw open–close movement. J Biomech. 1997;30 (9):883–889.

[19] J.H. Koolstra TMvE. A method to predict muscle control in the kinematically and mechanically indeterminate human masticatory system. JBiomech. 2001;34:1179–1188.

[20] J.A. Gal LMG, S. Palla, G. Murray, I.J. Klineberg. Analysis of human mandibular mechanics based on screw theory and vivo data. J Biomech. 2004;37:1405–1412.

[21] LAFARGUE D. Etude et élaboration de films à base de polysaccharides pour la fabrication de gélules pharmaceutiques. Thèse de Doctorat, Université de Nantes. Etude et élaboration de films à base de polysaccharides pour la fabrication de gélules pharmaceutiques.

[22] Bizot H, Le Bail P, Leroux B, Davy J, Roger P, Bule´on A. Calorimetric evaluation of the glass transition in hydrated, linear and branched polyanhydroglucose compounds. Carbohydrate Polymer. 1997;32:33–50.

[23] Chanvrier H, Colonna P, Della Valle G, Lourdin D. Structure and mechanical behaviour of corn flour and starch-zein based materials in the glassy state. Carbohydrate Polymers. 2005;59(1):109-119.

[24] Babin P, Della Valle G, Dendievel R, Lourdin D, Salvo L. X-ray tomography study of the cellular structure of extruded starches and its relations with expansion phenomenon and foam mechanical properties. Carbohydrate Polymers. 2007;68(2):329-340.

[25] Chanvrier H, Valle GD, Lourdin D. Mechanical behaviour of corn flour and starch-zein based materials in the glassy state: A matrix-particle interpretation. Carbohydrate Polymers. 2006;65(3):346-356.

[26] Chaunier L, Della Valle G, Lourdin D. Relationships between texture, mechanical properties and structure of cornflakes. Food Research International. 2007;40(4):493-503.

[27] Duizer L. A review of acoustic research for studying the sensory perception of crisp, crunchy and crackly textures. Trends in Food Science & Technology. 2001;12(1):17-24.

[28] Nicholls RJ, Appelqvist IAM, Davies AP, Ingman SJ, Lillford PJ. Glass transitions and the fracture behaviour of gluten and starches within the glassy state. Journal of Cereal Science. 1995;21(1):25-36.

[29] ROUDAUT. G DC, LE MESTE. M. Influence of water on the crispness of cerealbased foods : acoustic, mechanical, and sensory studies. Journal of Texture Studies. 1998;29:199-213.

[30] Huang JS, Lin JY. Fatigue of cellular materials. Acta Materialia. 1996;44(1):289-296.

[31] Engerand J-L. Mécanique de la rupture. Technique de l'ingénieur 1990.

[32] Gdoutos EE. Fracture mechanics : An Introduction. Kluwer Academic Publishers, Dordrecht, The Netherlands. 1993.

[33] IRWIN(G.R.). Analysis of stresses and strains near the end of a crack traversing a plate. Journal of applied mechanics. sept. 1957:361.

[34] Perez N. Fracture mechanics. Department of Mechanical Engineering
University of Puerto Rico. 2004.

[35] Hedjazi L, Guessasma S, Della Valle G, Benseddiq N. Finite element modelling of crack propagation in carbohydrate extruded starch with open void structure. Carbohydrate Polymers;83(4):1696-1706.

[36] Micheael F, Ashby, David R.H. Engineering materials 1, an introduction to their properties and applications. Butterworth Heinemann. 1996.

[37] Sander M, Richard HA. Finite element analysis of fatigue crack growth with interspersed mode I and mixed mode overloads. International Journal of Fatigue. 2005;27(8):905-913.

[38] Sander M, Richard HA. Experimental and numerical investigations on the influence of the loading direction on the fatigue crack growth. International Journal of Fatigue;28(5-6):583-591.

[39] Réthoré J, Gravouil A, Combescure A. A stable numerical scheme for the finite element simulation of dynamic crack propagation with remeshing. Computer Methods in Applied Mechanics and Engineering. 2004;193(42-44):4493-4510.

[40] Shahani AR, Amini Fasakhodi MR. Finite element analysis of dynamic crack propagation using remeshing technique. Materials & Design. 2009;30(4):1032-1041.

[41] Rashid MM. The arbitrary local mesh replacement method: An alternative to remeshing for crack propagation analysis. Computer Methods in Applied Mechanics and Engineering. 1998;154(1-2):133-150.

[42] H.C. Lee JSC, K.H. Jung, Y.T. Im. Application of element deletion method for numerical analyses of cracking. Journal of Achievements in Materials and Manufacturing Engineering 35/2. 2009:154-161.

[43] Dejak B, Mlotkowski A, Romanowicz M. Finite element analysis of mechanism of cervical lesion formation in simulated molars during mastication and parafunction. The Journal of Prosthetic Dentistry. 2005;94(6):520-529.

[44] Needleman A. An analysis of tensile decohesion along an interface. Journal of the Mechanics and Physics of Solids. 1990;38(3):289-324.

[45] Tvergaard V. Resistance curves for mixed mode interface crack growth between dissimilar elastic-plastic solids. Journal of the Mechanics and Physics of Solids. 2001;49(11):2689-2703.

[46] Camacho GT, Ortiz M. Computational modelling of impact damage in brittle materials. International Journal of Solids and Structures. 1996;33(20-22):2899-2938.

[47] Geubelle PH, Baylor JS. Impact-induced delamination of composites: a 2D simulation. Composites Part B: Engineering. 1998;29(5):589-602.

[48] Belytschko J-HSHWT. A comparative study on finite element methods for dynamic fracture. Private communication. 2007.

[49] Bellis C. Méthode des Eléments de Frontière Accélérée en Mécanique de la Rupture 3D. Master 2 « Mathématiques et Applications ». 2007-2008.

[50] Dacheng S, Xingrui M. An application of the boundary element method to the fatigue crack propagation in a cracked heterogeneous body. Engineering Fracture Mechanics. 1997;56(6):839-840.

[51] Ortiz J, Cisilino AP, Otegui JL. Boundary element analysis of fatigue crack propagation micromechanisms in austempered ductile iron. Engineering Analysis with Boundary Elements. 2001;25(6):467-473.

[52] Belytschko T, Lu YY, Gu L. Crack propagation by element-free Galerkin methods. Engineering Fracture Mechanics. 1995;51(2):295-315.

[53] Cordes LW, Moran B. Treatment of material discontinuity in the Element-Free Galerkin method. Computer Methods in Applied Mechanics and Engineering. 1996;139(1-4):75-89.

[54] Belytschko T, Organ D, Gerlach C. Element-free galerkin methods for dynamic fracture in concrete. Computer Methods in Applied Mechanics and Engineering. 2000;187(3-4):385-399.

[55] Dienes GJ, Paskin A. Molecular dynamic simulations of crack propagation. Journal of Physics and Chemistry of Solids. 1987;48(11):1015-1033.

[56] Melenk JM, Babuska I. The partition of unity finite element method: Basic theory and applications. Computer Methods in Applied Mechanics and Engineering. 1996;139(1-4):289-314.

[57] Gravouil A MN, Belytschko T. Non-planar 3D crack growth by the extended 5nite element and level sets : Part II: Level set update. International Journal of Numerical Methods in Engineering. 2002;53:2569-2586.

[58] Elguedj T, Gravouil A, Combescure A. Appropriate extended functions for X-FEM simulation of plastic fracture mechanics. Computer Methods in Applied Mechanics and Engineering. 2006;195(7-8):501-515.

[59] Zi G BT. New crack-tip elements for XFEM and applications to cohesive cracks. International Journal of Numerical Methods in Engineering. 2003;57:2221-2240.

[60] Menouillard T RJ, Combescure A, Bung H. Efficient explicit time stepping for the eXtended Finite Element Method (X-FEM). International Journal of Numerical Methods in Engineering. 2006;991-939:68.

[61] Liang J, Huang R, Prévost JH, Suo Z. Evolving crack patterns in thin films with the extended finite element method. International Journal of Solids and Structures. 2003;40(10):2343-2354.

[62] Cundall P.A. SODL. A discrete numerical model for granular assemblies. Géotechnique. 1979;29(1):47-65.

[63] Poschel T. ST. Computational Granular Dynamics: Models and Algorithms. Springer, ISBN : 3540214852. 2005.

[64] Rojek J, Oñate E, Labra C, Kargl H. Discrete element simulation of rock cutting. International Journal of Rock Mechanics and Mining Sciences;48(6):996-1010.
[65] Liu X, Martin CL, Delette G, Bouvard D. Elasticity and strength of partially sintered ceramics. Journal of the Mechanics and Physics of Solids;58(6):829-842.

Chapitre II. Mécanismes de propagation de fissure

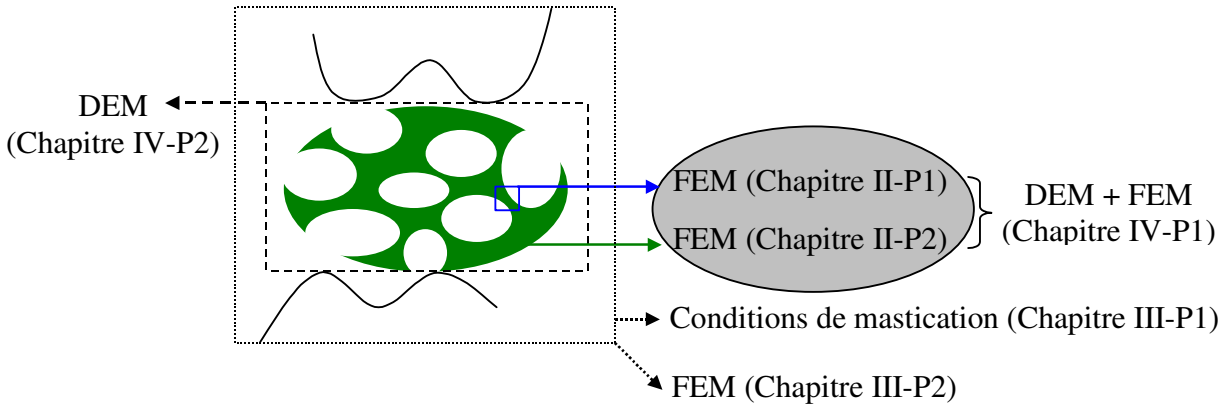

Les propriétés mécaniques à la rupture gouvernent la texture des aliments solides, et spécialement celle des produits céréaliers alvéolaires, qui sont la base de notre alimentation (pain, biscuits, céréales pour petit déjeuner...). Elles dépendent de leur structure multi-échelle, des propriétés mécaniques du matériau biopolymère dense composant les parois. Le but de ce chapitre est donc d'appliquer les principes de la mécanique de la rupture afin de comprendre la propagation des fissures dans un matériau à base d'amidon amorphe vitreux, et donc fragile, en considérant le matériau dense puis alvéolaire. L'évolution d'une fissure dépend de plusieurs propriétés intrinsèques du matériau, la géométrie de l'échantillon et la nature des charges appliquées. Ces caractéristiques doivent être prises en compte dans une approche de modélisation numérique.

Dans une première partie, l'objectif est donc de démontrer que les principes de fracture régissent la propagation de fissures dans le matériau dense à base d'amidon. Plus précisément, nous nous consacrerons à la détermination des critères de propagation permettant de prédire la trajectoire des fissures. Pour cela, la propagation de la fissure dans les matériaux biopolymère vitreux est étudiée numériquement et expérimentalement. La méthode numérique est développée dans le code élément finis (EF) Ansys pour la modélisation de la propagation de la fissure 2D dans des matériaux élastiques fragiles. La modélisation nécessite notamment des techniques de déboutonnage de nœuds. Un critère de taux de restitution d'énergie est utilisé afin de déterminer la nouvelle direction de propagation de la fissure à chaque pas de temps. Les résultats du modèle sont comparés à ceux d'essais expérimentaux effectués sur des éprouvettes entaillées trouées sous une charge de traction. Les résultats expérimentaux montrent que le chemin de la fissure est influencé par la présence du trou, ce qui permet de tester le critère de la propagation des fissures en mode mixte. Les résultats obtenus, et en particulier la stratégie de présentation de la fissure, ainsi que la bonne prédiction de sa propagation en fonction du critère utilisé montrent l'intérêt de la méthode EF pour la modélisation de la propagation de fissures.

Dans une seconde partie, est abordé le rôle de la structure cellulaire sur la mécanique de la rupture des aliments solides alvéolaires, notamment par la présence de vides et la multiplicité des défauts à partir desquels la fissuration peut se développer. En effet, l'hétérogénéité de contraintes se développe dans de tels matériaux à proximité des parois cellulaires, ce qui conduit à un comportement de fracturation plus complexe. Cette partie présente donc une extension de la méthode de découplage des degrés de liberté pour prendre en compte la structure cellulaire d'un amidon extrudé, afin de simuler la propagation des fissures dans ce type de matériau, pris comme modèle d'aliment céréalier. Dans ces

matériaux, une répartition complexe des contraintes a lieu lors du chargement, conduisant à une extension de la fissure différent de celle du matériau dense. En se basant sur la notion des facteurs d'intensité de contrainte, le critère de taux de restitution d'énergie maximale est mis en œuvre. La méthode définie en partie 1 est adaptée à ce type de matériau. Le maillage est basé sur une modification de la connectivité des éléments sur un maillage régulier (2D). Une valeur du module de Young est attribuée à chaque élément en fonction du niveau du pixel associé aux gris des images, qui reflète la structure cellulaire. Les résultats numériques montrent que la structure cellulaire est responsable du développement d'un mode mixte local. La propagation des fissures montre des changements significatifs de chemin en raison de la répartition hétérogène des contraintes. La comparaison entre les chemins de fissure numériques et expérimentaux montre bien que les prédictions des fissures sont sensibles à la résolution du maillage et à la distribution de niveaux de gris. Enfin, le critère est capable de bien prédire l'extension de fissure si le contraste entre les régions est correctement décrit. Un des intérêts de ce modèle réside dans son aptitude à être généralisé à des aliments éréaliers fragiles, dont l'amidon extrudé, amorphe vitreux et cellulaire, fournit un bon modèle.

Partie 1

Modélisation par éléments finis de la propagation de la fissure dans un matériaux dense biopolymère a base d'amidon

Article.1

How cracks propagate in a vitreous dense biopolymer material

Hedjazi L, Guessasma S, Valle GD, Benseddiq N. How cracks propagate in a vitreous dense biopolymer material. Engineering Fracture Mechanics;78(6):1328-1340.

How cracks propagate in a vitreous dense biopolymer material

L. Hedjazi[1] , S. Guessasma[1]* , G. Della Valle[1], N. Benseddiq[2]

[1] INRA, UR 1268 Biopolymères, Interactions & Assemblages (BIA), Rue de la Géraudière, 44316 Nantes , France

[2] University of Lille 1-CNRS, UMR 8107, Laboratory of Mechanics of Lille, BP179, 59653 Villeneuve d'Ascq, France

* Corresponding author

Phone. +33 (0)2 40 67 50 36, fax.+33(0)2 40 67 51 67

E-mail address: sofiane.guessasma@nantes.inra.fr

1. Abstract

Crack propagation in vitreous biopolymer material is studied considering numerical and experimental aspects. Finite Element computation is performed to predict crack propagation in starch material. Maximum dilatational strain energy criterion is used as a criterion for crack propagation. Model validation is undertaken considering notched specimens with a hole under tensile loading. The experimental results show that the crack path is affected by the presence of the defect, which allows adequate testing of the crack propagation criterion under a mixed mode. The predicted results show that the selected criterion anticipates adequately the crack propagation in vitreous starch under linear elastic conditions.

Keywords

Fracture mechanics; Crack growth; Vitreous biopolymer; Finite Element method.

2. Introduction

Human mastication of cereal based products can be regarded as a complex mechanical process leading to food particle breakdown. Because of its importance for the other degradation steps, understanding such a process depends on our ability to address fracture mechanisms that are associated to mastication.

Mastication is a mechanical process that allows size reduction of food upon complex loading conditions [1, 2]. Several approaches have been developed to account for the mechanics of mastication [1, 3]. Statistical approaches that aims at considering size reduction as related to the probability of particle selection are a way to describe the size reduction process [4, 5].

However, these approaches do not account for the mechanisms responsible for such reduction. The idea of comparing mastication to simple mechanical tests is a first step to understand material fracturing behaviour [1]. Although the apparent loading is transmitted from the cheek muscles to food particles by compression, the non-uniform contact between teeth and food item allows a more efficient bending deformation mechanism. Thus, in several crispy products such as breakfast cereals, food breakdown operates following the idea of the opening mode, which is one of the well known fracture modes commonly observed in materials. The opening mode requires local tension loading and the presence of a defect for crack propagation. Upon loading, stress concentration in the vicinity of the defect leads to crack propagation and material failure if enough energy is delivered.

The aim of this work is to apply principles of the fracture mechanics in order to understand crack propagation in solid food products, and specially cereal foods which are the basis of our diet (breads, biscuits, breakfast cereals…). Such products have a complex multi-scale structure and all these levels influence their mechanical properties (see for instance [6]). For example, cellular structure influences significantly the mechanics of food breakdown primarily because of the presence of voids and multiplicity of defects from which cracking could develop. Stress heterogeneity develops in such materials near the cell walls leading to a more complex fracturing behaviour. However, we do not want to introduce this important effect into our analysis but rather focus on dense vitreous starch because it represents the main ingredient of many processed cereal products. As the main component of the cell walls, its fracture behaviour is supposed to be essential for the fragmentation process of the cereal food. The objective of this work remains attached to the demonstration that fracture principles govern the propagation of cracks in dense starch material. More precisely, we focus on the determination of the crack trajectory of biopolymer-based material using adequate crack propagation criteria.

3. Modelling technique

Following the idea of Griffith [7], the presence of a crack in an elastic material decreases the potential energy and increase the surface energy [8]. Energy increase is related here to the creation of additional surfaces in the material, in a way that pending bonds between atoms belonging to these surfaces increase the energy of the material. At the microstructure scale, crack initiation is a material response to the mechanical instability driven by the excessive amount of energy that the material is not capable to accumulate. Mechanical instability depends on the spatial distribution of material heterogeneities. Spatial monitoring of the

change in the strain energy density is one way to predict when and where crack extension develops [9]. This principle is used, in this work, combined with the stress intensity factors to evaluate the crack propagation in starch material.

3.1. Crack propagation criteria

In the present work, linear elastic fracture mechanics is used to address the particular problem of crack propagation in starch material. Within this framework, the stress intensity factor (K) concept is particularly exploited [10]. This quantity is the driving force for crack extension [8, 9]. It relates the local elastic stress field near the crack tip to the known global stress or displacement field. Stress intensity factor can thus be derived by computing the stress or displacement field in the local coordinate system attached to the crack tip. In a 2D analysis, it can be shown that the stress field has the following form [11] :

$$\sigma_i(r,\theta) = \frac{K_i}{\sqrt{2\pi r}} f_i(\theta) \tag{1}$$

where σ_i denotes the stress tensor, K_i is the stress intensity factor, f_i is a geometrical function defining the angular dependency of the stress field. Voigt notation is used for tensor indices.

In the case of a plate containing a centre crack, the terms in expression (1) may therefore be explicated as follows [9]:

$$\sigma_1 = \frac{K_I}{\sqrt{2\pi r}}\cos\frac{\theta}{2}\left(1-\sin\frac{\theta}{2}\sin\frac{3\theta}{2}\right) - \frac{K_{II}}{\sqrt{2\pi r}}\sin\frac{\theta}{2}\left(2+\cos\frac{\theta}{2}\cos\frac{3\theta}{2}\right) \tag{2a}$$

$$\sigma_2 = \frac{K_I}{\sqrt{2\pi r}}\cos\frac{\theta}{2}\left(1+\sin\frac{\theta}{2}\sin\frac{3\theta}{2}\right) + \frac{K_{II}}{\sqrt{2\pi r}}\sin\frac{\theta}{2}\cos\frac{\theta}{2}\cos\frac{3\theta}{2} \tag{2b}$$

$$\sigma_6 = \frac{K_I}{\sqrt{2\pi r}}\cos\frac{\theta}{2}\sin\frac{\theta}{2}\cos\frac{3\theta}{2} + \frac{K_{II}}{\sqrt{2\pi r}}\cos\frac{\theta}{2}\left(1-\sin\frac{\theta}{2}\sin\frac{3\theta}{2}\right) \tag{2c}$$

In an infinite plate containing a crack with length 2a and loaded by a normal stress σ_2 and shear stresses σ_6, the stress intensity factors are :

$$K_I = \sigma_2\sqrt{\pi a} \tag{3a}$$

$$K_{II} = \sigma_6\sqrt{\pi a} \tag{3b}$$

K_I is related to the opening mode whereas K_{II} has to deal with shearing effect. When both modes are contributors, a mixed mode model has to be planned. For instance, during mastication, both factors are associated to the fracturing but with a more prevailing opening mode, especially in the case of a brittle material.

The computation of crack intensity factors allows to compare, at a given loading, their value to the critical intensity factor, i.e. crack toughness Kc or resistance force to crack extension, which is a material property. If the computed intensity factors exceed the material property, then material fracture occurs. This statement defines the first crack propagation criterion, which determines when a crack propagates. In our case, the sample geometry used in the experimental part does not allow a direct measurement of the crack growth resistance Kc. If we consider the material to be brittle enough, Kc is proportional to the fracture load. This last quantity is measurable and is instead used to determine the first criterion for the starting of crack extension.

However, this criterion does not predict the direction of crack propagation θ.Various criteria for the crack growth direction under mixed-mode loading have been proposed in the literature (see for example [8, 9, 12] for a review of the main contributions). Among the possible criteria [13-21], we have implemented the maximum dilatational strain energy criterion, which is detailed hereafter.

The volume strain energy density can be defined as :

$$\Gamma = \int_0^{\varepsilon_i} \sigma_i d\varepsilon_i \tag{4}$$

where ε_i and σ_i are the stress and strain components.

Considering that the material is Hookean :

$$\Gamma = \int_0^{\varepsilon_i} \sigma_i s_{ij} d\sigma_j \tag{5}$$

Where s_{ij} are the components of the compliance tensor.

Assuming that the material is isotropic, each of the compliance components can be expressed as a function of the engineering constants :

$$s_{11} = 1/E \tag{6a}$$

$$s_{12} = -\nu/E \tag{6b}$$

$$2(s_{11} - s_{12}) = 1/G \tag{6c}$$

where ν, E and G are Poisson coefficient, Young and shear moduli, respectively.

Taking into account the deformation components, it turns out that the elastic energy can be expressed as follows :

$$\Gamma = \frac{1}{2E}\left(\sigma_1^2 + \sigma_2^2 + \sigma_3^2\right) - \frac{\nu}{E}\left(\sigma_1\sigma_2 + \sigma_1\sigma_3 + \sigma_2\sigma_3\right) + \frac{1}{2G}\left(\sigma_4^2 + \sigma_5^2 + \sigma_6^2\right) \tag{7}$$

The minimum of Γ is related to significant volume change, where dilatation dominates whereas its maximum is correlated to shape variation (distortion), which leads to yielding.

The strain energy density can be thus decomposed into dilatational Γ_v and distortional Γ_d components as a sum :

$$\Gamma = \Gamma_v + \Gamma_d \tag{8}$$

where :

$$\Gamma_v = \frac{1-2\nu}{6E}\left(\sigma_1+\sigma_2+\sigma_3\right)^2 \tag{9}$$

and

$$\Gamma_d = \frac{1+\nu}{6E}\left[\left(\sigma_1-\sigma_2\right)^2+\left(\sigma_1-\sigma_3\right)^2+\left(\sigma_3-\sigma_2\right)^2+6\left(\sigma^2{}_4+\sigma^2{}_5+\sigma^2{}_6\right)\right] \tag{10}$$

In the following, plane strain is assumed since the stress distribution within the material thickness is not negligible within the framework of the 2D-analysis. It follows that the expressions of the densities of strain energy can be rewritten as :

$$\Gamma = \frac{1}{2E}\left(\sigma_1+\sigma_2\right)^2-\frac{\left(1+\nu\right)}{E}\left(\sigma_1\sigma_2+\sigma_6^2\right) \tag{11}$$

$$\Gamma_v = \frac{\left(1-2\nu\right)\left(1+\nu\right)^2}{6E}\left(\sigma_1+\sigma_2\right)^2 \tag{12}$$

$$\Gamma_d = \frac{1+\nu}{3E}\left[\nu\left(\sigma_1+\sigma_2\right)^2-2\nu\sigma_1\sigma_2\left(1+\nu\right)^2+\left(1-\nu\right)^2\left(\sigma_1-\sigma_2\right)^2+3\sigma^2{}_6\right] \tag{13}$$

The maximum energy release rate criterion stipulates that crack extends along the direction of maximum dilatational strain energy density, neglecting distortion effects.

This criterion can be enounced as :

$$\frac{\partial}{\partial\theta}\Gamma_v = 0 \quad ; \quad \frac{\partial^2}{\partial\theta^2}\Gamma_v < 0 \tag{14}$$

Knowing that the energy release due to the presence of a crack of size r is :

$$\Sigma = r\Gamma \tag{15}$$

where Σ is the factor of strain energy density.

The criterion reduces to :

$$\frac{\partial}{\partial\theta}\Sigma = 0 \quad ; \quad \frac{\partial^2}{\partial\theta^2}\Sigma < 0 \tag{16}$$

Taking advantage of the analytical expressions of the stress singularities (equations II2a-II2c) and the dilatational term of the strain energy density (equation 12) under plane strain state, the dilatational part of the factor of strain energy density can be written :

$$\Sigma_v = \frac{(1-2\nu)(1+\nu)^2}{6E}\left((1+\cos\theta)K_I^2 - 2\sin\theta K_I K_{II} + (1-\cos\theta)K_{II}^2\right) \quad (17)$$

The criterion (expression 16) can be further simplified into :

$$\frac{\partial}{\partial\theta}\left(K_I^2\cos\theta - 2\sin\theta K_I K_{II} - \cos\theta K_{II}^2\right) = 0 \quad ; \quad \frac{\partial^2}{\partial\theta^2}\left(K_I^2\cos\theta - 2\sin\theta K_I K_{II} - \cos\theta K_{II}^2\right) < 0 \quad (18)$$

Finally, the angle that maximises the dilatational strain energy corresponds to the optimal crack direction. The optimal quantity θ_c must satisfy the following constraints :

$$\theta_C = \arctan\left(\frac{2K_I K_{II}}{K_{II}^2 - K_I^2}\right) \quad (19a)$$

$$\theta_C > \arctan\left(\frac{K_I^2 - K_{II}^2}{2K_I K_{II}}\right) \quad (19b)$$

Inequality (19b) simply means that the function $\Sigma_v(\theta)$ possesses a maximum value when $\theta=\theta c$.

3.2. Finite Element computation

Finite Element computation is used for the implementation of the crack propagation criteria. A specific tool is developed under the ANSYS package environment (ANSYS Inc, Canonsburg, Pennsylvania, U.S.A.) for such a purpose. Linear elastic analysis is conducted on a 2-dimensional plane under the plane strain state. A single hole is introduced in order to create a heterogeneous stress distribution upon loading. Such stress field allows a local mixed mode to be implemented even if only traction is used. The other way of creating a heterogeneous stress at the crack tip is to consider a mixed loading device [22]. This way is not considered here because of the difficulty to perform reliable experiments with brittle starch specimens. The plate is meshed using 8-node quadrilateral elements (PLANE 82). This element has structural displacement capabilities in X and Y directions. A specific regular meshing of the plate is developed assuming a modified element connectivity as shown in Figure 1a. The benefit of using regular meshing is to avoid remeshing while conducting the analysis, which can be a source of numerical instabilities (see [22-26] for some examples of other alternatives). The cost of using a regular mesh is to plan initially significant refinement

in order to represent properly the structure geometry. Each element in our regular mesh does not share any node with the neighbouring elements. Prior to loading, all coincident nodes are coupled, which means that structural displacements in both directions are the same until given criteria are satisfied. If so, node decoupling is decided in order to simulate crack extension. Such technique is more efficient compared to those techniques based on element deletion [27-29], which provoke significant material removal. A horizontal crack of length (a) is initiated by decoupling all nodes composing the horizontal line (Figure 1b). Plate dimensions, crack length and position as well as hole size and relative position with respect to the crack tip are adjusted to fit the experimental conditions detailed in the next section.

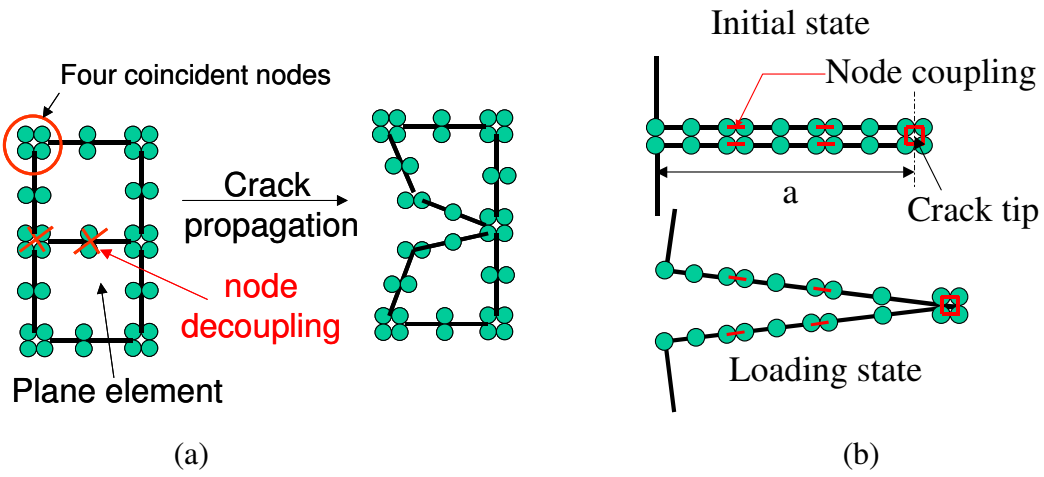

Figure 1. *(a) Modified element connectivity for crack propagation. (b) crack initiation using node decoupling.*

Mesh density is varied in order to study the mesh sensitivity to crack path prediction. A typical FE model contains a total of 1.44×10^6 degrees of freedom (dof).

The material behaviour is supposed to be elastic and isotropic. Elastic parameters are determined based on tensile loading experiments performed on unnotched specimens with no hole. The measured Young's modulus is 0.312 GPa and Poisson's ratio is 0.3.

The boundary conditions correspond to the experimental tensile loading conditions. All nodes of the bottom line are constrained against displacement in X-direction whereas a structural displacement –U(t)/2 is imposed in Y-direction, where t refers to the simulation time. Similarly, nodes of the top line are displaced by a positive amount + U(t)/2 in Y-direction and the rest of the degrees of freedom is fixed to the ground value.

The elastic problem is solved using the preconditioned Conjugate Gradient PCG solver. At each load (time) increment, a post-processing is applied to compute the stress intensity factors

based on the nodal displacement field. Crack propagation is decided based on the flowchart given in Figure 2. Because of numerical instabilities upon node decoupling, some additional substeps are added without increasing further loading in order to allow stress equilibrium conditions. Such a step is performed before any additional load (time) increment.

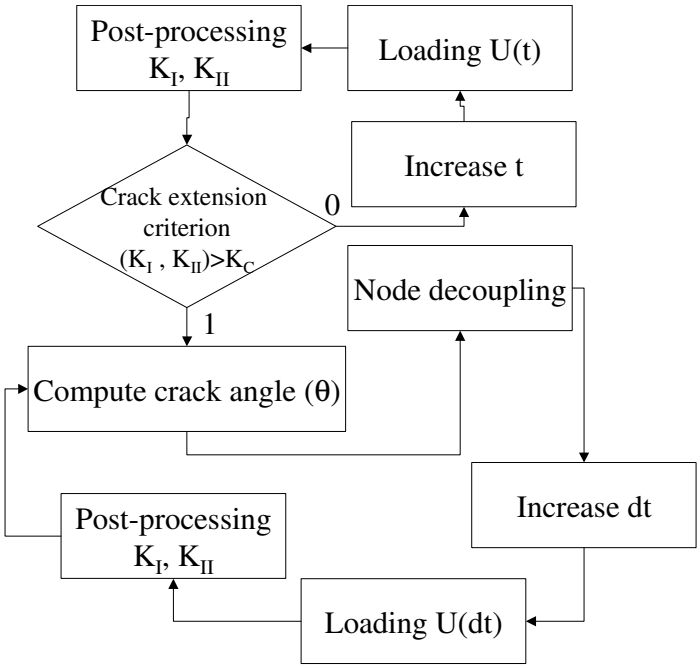

Figure 2. *Flowchart summarizing the main steps for the simulation of crack propagation.*

Because decoupling is performed on a regular square grid, decoupling leads to a rough approximation of the crack direction. Within a single step, only three angles can be selected 0°, 90° or –90°. In order to improve further more the accuracy of crack direction prediction, especially for a prevailing opening mode, crack extension is performed along couples of length units on a square grid containing 20x20 elements. It is then possible to describe crack extension within an accuracy of about 2.79 degrees. Each decoupling step represents thus a crack extension along the 20x20 units, corresponding to a physical dimension varying between 0.66 mm and 2.0 mm.

4. Experimental layout

The raw material is a native potato starch, purchased from Roquette (Lille, 59-France). Preprocessing of native starch is performed using extrusion. The initial moisture content is 16 % on a total water basis (wb). Starch is mixed with water to increase the total moisture to

about 27% wb. The mixture is stored in a cool environment for about 24 hours before processing.

SCANIA (Crosne, France) single-screw extruder is used to process the mixture under the following conditions: the temperature profile is 100-110-120 °C, leading to a product temperature of about 127°C. The specific mechanical energy is 251±27 J/g for a feed rate of about 360±28 g/h and a screw rotation speed of 25 rpm. Ribbons (thickness 1mm) with a final moisture content of 13 - 14 % (wb) are milled using nitrogen cryogrinding to obtain an amorphous powder. The starch powder is stored in a controlled environment at a relative humidity of 60% (NaBr), a temperature of 20° for 2 weeks.

Thermomoulding of amorphous starch powder is performed with a temperature of 140°C, a pressure of about 57 MPa and a duration of 15 min, before water cooling of the mould. Strips of dimensions 35 x 10 x 1 mm^3 are obtained and stored in dessicators at a controlled relative humidity (NaBr, RH= 60 % , 20 °C), until they reach a stable final moisture content of about 12% wb. Under these conditions, the glass transition temperature (Tg) of amorphous starch is much higher than ambient temperature (Tg ≈ 100°C) and the sample is expected to display a brittle behaviour [30].

Holes are designed in the specimens to allow stress concentration to develop (Figure 3). Notches are performed on the specimens using a circular saw (thickness 100 µm). The notch size is larger than 0.5 mm to guarantee a fracture force within the load cell limits (Figure 3). The notch depth is also limited to avoid a unique opening mode.

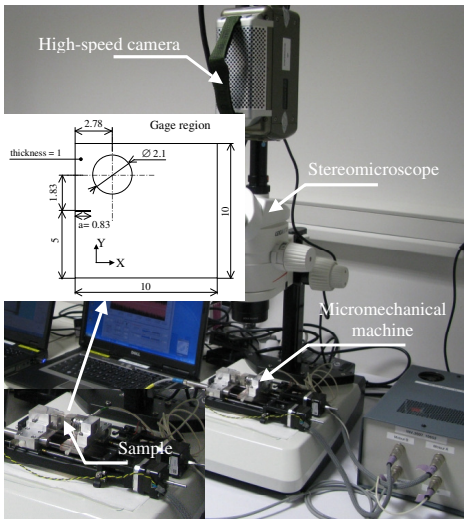

Figure 3.*Experimental setup for crack growth monitoring.*

Mechanical testing is undertaken using a micro-mechanical testing machine capable of micro level displacement. The load cell has a peak force of ±125 N with an accuracy of 0.25N. The

load frame is 0.5 – 125 N. The driving system is composed of two synchronised motors ensuring a displacement accuracy of 1.25 µm. The displacement range is 0.01 – 20 mm. The displacement rate can be tuned in the range 1.25 – 2000 $\mu m.s^{-1}$. Traction is performed on notched specimens. Sample mounting is ensured by a drop of super glue on the fixtures. The specimen is positioned carefully on the fixture. A low pressure is maintained on the specimen for about 1 minute, creating a uniform glue layer and squeezing out the excess of glue. The gage length is adjusted to about 10 mm (Figure 3). Traction is performed under a constant displacement rate of 40 $\mu m.s^{-1}$ and up to material failure. Mechanical testing is coupled to image acquisition using a high speed camera Phantom V7.3 from Photonline (Marly Le Roi, 78-France). The camera is used to observe the crack propagation while testing and, if possible, to determine the crack speed (see for example [11] for a review of available techniques for crack observation). The camera is based on an active pixel CMOS sensor (Figure 3) . It allows a full frame size of 800x600 pixels, for which the recording rate attains 6688 frames per seconds. It is possible to increase further more the recording speed up to 190 000 fps but with the cost to decrease the ROI (Regions of Interest) size. Several tests are performed to determine the largest ROI size for which crack extension can be observed, at least within two frames. In order to ensure optimal performance, the high-speed camera is mounted on a stereomicroscope (Figure 3). Sample observation is realised under low magnification conditions in order to increase the pixel size. The ROI size, corresponding to the gage length, is 300 pixels, for which the pixel size is 33 µm. Crack path is determined experimentally using image analysis. Thresholding and skeletonisation operators are performed on the images followed by isolation and averaging of the crack faces positions. All these procedures are performed using the public domain image analysis software (ImageJ from NIH-USA).

5. Results and discussion

Figure 4a shows a typical load–displacement curve obtained in the case of a mixed-mode fracture experiment. As expected, brittle failure characterises the starch material at a water content of 12%wb as no plastic deformation is observed prior fracturing.

Fracture load in the linear part authorises the use of the critical intensity factor as a linear-elastic fracture criterion [31]. Its magnitude, for the considered sample dimensions, is about 79 N. Figure 4b shows the observed crack trajectory corresponding to the mechanical response shown in Figure 4a.

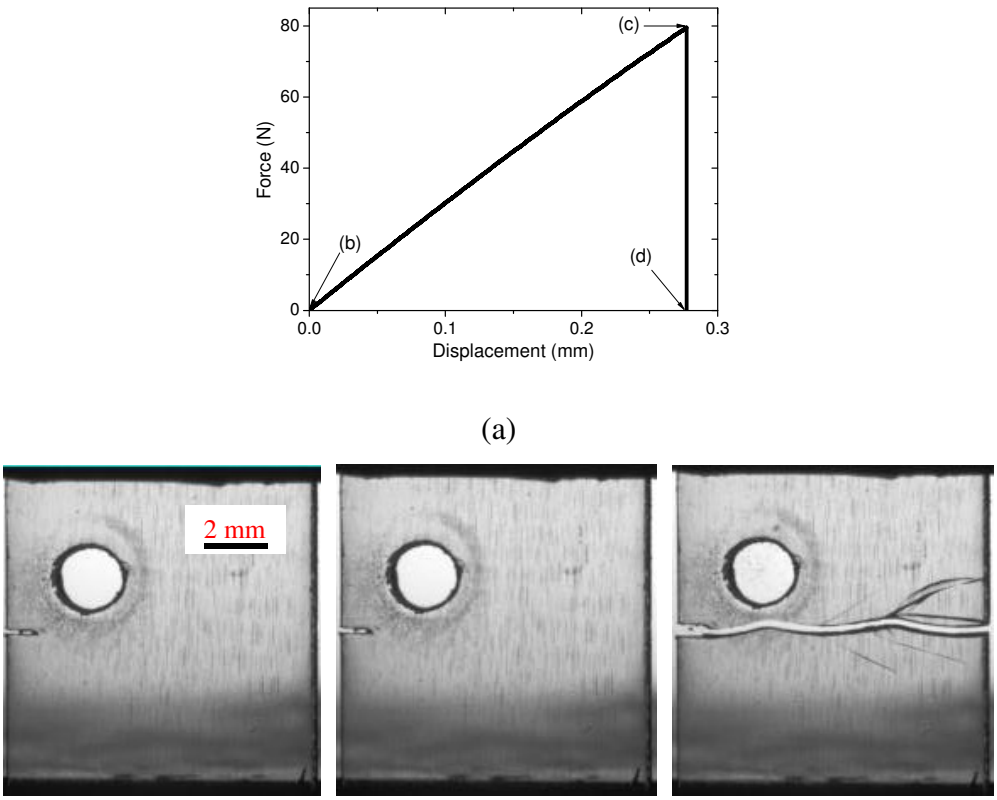

Figure 4. *(a) Load response of notched starch specimen for which (b)-(d) crack trajectory is deviated by the presence of a hole.*

Sudden failure of the material is observed which means that a large extension of the crack is triggering unstable fracture. The crack path is deviated by the presence of the defect as a consequence of the stress concentration around the hole. Crack – defect interaction is a well known feature and is widely observed [23, 32, 33]. Crack path deviation depends on the relative position of the notch with respect to the hole. It can be understood that the largest energy release is maximised if the crack stops at the hole. This situation is depicted in Figure 5, where the notch position intersects the hole.

Figure 5a shows that crack-stopping (Figure 5d) requires reloading of the structure in order to increase the stress level up to the complete failure of the material. Stress reconcentrates at the periphery of the hole where crack departure is likely to be initiated. At this stage, the complete failure of the material is associated to two cracks that extend in a two-stage process. When the notch is far enough from the hole position, the crack is not sensitive to the stress

heterogeneity developed near the hole. Crack extension depends thus on the unique opening mode.

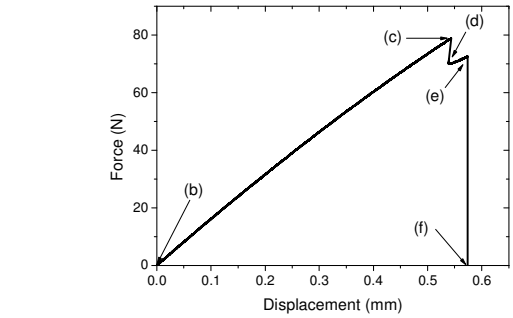

(a)

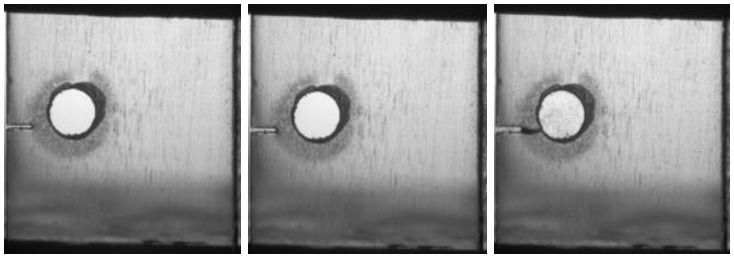

(b) initial (c) opening (d) crack-stopping

(e) reloading (f) failure

Figure 5. *(a) Mechanical response associated to (b)-(d) crack-stopping and the (e) reloading stage which allows (f) complete failure of the material.*

In all cases, cracks under tensile loading undertake significant crack path changes, which are often named crack branching [8, 34-36]. The present crack branching is a quite different phenomenon compared to crack coalescence [37]. Indeed, when the crack extends beyond the hole, it continues its extension using the unique opening mode. But, the crack path changes suddenly and several branches appear at different positions. It is not completely understood which mechanism drives such phenomenon. It can be attributed to the interaction of the crack

tip with microstructural defects [8]. Such instability is driven by the accumulation of strain energy because the crack is not able to attain the Rayleigh wave speed [25, 38, 39]. Such explanation becomes meaningful when the far-field driving force is well above the necessary fracture energy, and in turn the crack speed becomes dependent on the acoustic wave speed. Crack branching can be thus regarded as a kinetic response of the material to the unbalanced Griffith criterion, i.e., strain energy release rate increases significantly while the energy needed to create additional surfaces is almost constant [34].

Crack branching can lead to significant fragmentation of the sample, as shown in Figure 6. For this particular configuration, stress concentration at the hole circumference exceeds that of the crack tip, which promotes crack nucleation around the hole. Taking into account the time interval between the frames of Figure 6b and 6c, it is possible to give an estimation of the crack extension velocity, which, for some branches, appear to be as large as 136 $m.s^{-1}$ (for instance taking into account the distance between arrows in Figure 6c and 6d). Since only one time interval separates the frames, it is not possible to properly measure the crack velocity. All efforts to increase further more the frame rate are inconclusive for the observation the crack growth within a larger temporal window. Moreover, among the recognised difficulties to measure the crack speed in brittle transparent materials is the fact that surface observation of the sample provides a measurement of the crack position averaged over sample thickness (Figure 6c) [11]. The observed crack velocity is a limiting value, much lower than Rayleigh surface wave speed (of the order of 2000 – 5000 $m.s^{-1}$) for solid materials [11, 40]. The crack speed is thus a material dependent quantity. Beside crack branching, other instabilities are observed such as wavy crack path (Figures 4d, 5f, 6d). This instability is a direct consequence of crack speed reduction and the formation of soft material zone near the crack tip [40].

The FE analysis is conducted in order to predict the crack propagation in the case of a fracture mixed mode configuration, where crack deviation is observed without crack stopping. The case treated here is that corresponding to Figure 4. The crack branching is not considered numerically since the present crack growth criteria does not allow the prediction of such phenomenon. Crack branching tracking require an additional criterion such as a critical crack velocity [38]. See for example [26] for more details.

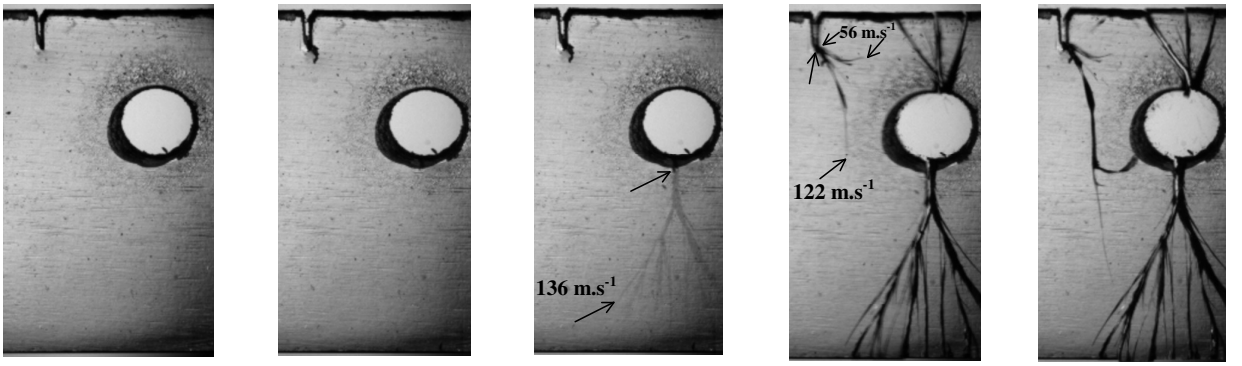

(a) prior loading (b) opening (t=0 s) (c) crack extension (t=33 µs) (d) t =66 µs (e) t =99 µs

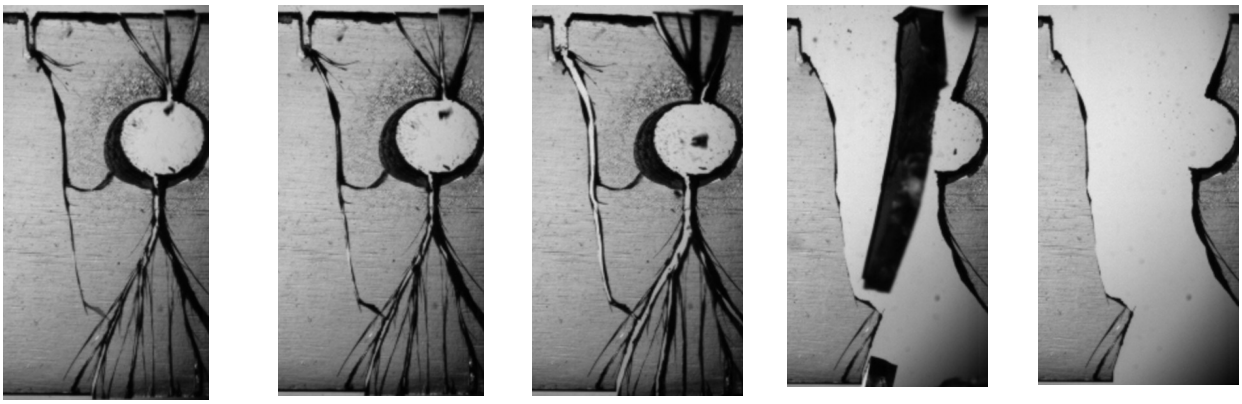

(f) t =132 µs (g) t =165 µs (h) t =297 µs (i) t =2871 µs (j) t =38841 µs

Figure 6. *Crack branching in brittle starch. ROI size 160x304 pixels, frame rate 30303 fps, frame interval 33 µs.*

Figure 7 shows the crack path predictions for several mesh sizes ranging from $1.6x10^5$ to $1.44x10^6$ dofs. The crack increment dimension varies between 0.66 mm up 2.0 mm depending on the mesh refinement. This quantity corresponds to the total number of node decoupling within a unit of time increment. It is clearly depicted that the mesh refinement has a large influence of the prediction of crack trajectory (Figure 7).

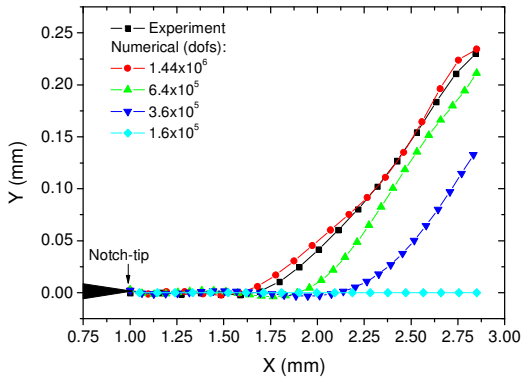

Figure 7. *Crack path prediction as function of mesh density under a mixed-mode loading.*

As the mesh size is increased the crack angle accuracy is improved. A good agreement between the finite element and the experimental results is observed for the largest mesh size. This result shows that the maximum dilatational strain energy release criterion is capable of capturing the crack trajectory under mixed-mode loading conditions.

Figure 8 depicts the evolution of the stress intensity factors (K_I and K_{II}) as well as the crack angle as function of crack extension. These predictions correspond to the largest mesh size and thus to the best agreement between the experimental and numerical paths. As the loading increases, the opening stage corresponds to the stress accumulation at the crack tip without any crack extension. During this stage, K_I increases up to a critical value (K_{IC} = 0.49 $MPam^{0.5}$) for which crack instability is reached. This value corresponds to the failure load F= 79 N. The crack extends and as it approaches the hole position, the mixed-mode develops, which corresponds to the increase of K_{II} up to 0.08 $MPa.m^{0.5}$ (Figure 8).

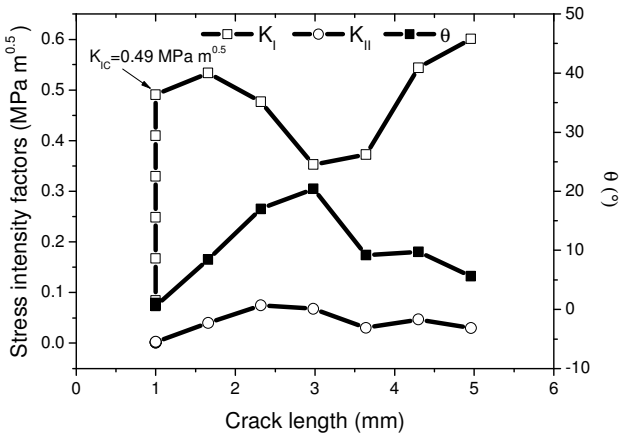

Figure 8. *Predicted stress intensity factors and crack direction as function of crack extension for the largest mesh density under mixed-mode loading.*

When the crack bypasses the hole, the opening mode predominates again as shown by the decrease of K_{II}. Even far from the hole position, the sliding (shearing) mode is still contributor (K_{II}= 0.03 $MPa.m^{0.5}$). At any crack position, we notice that the ratio K_{II}/K_I does not exceed 20%, which means that even in the presence of a hole, the local mixed-mode does not allow an equal balance between shearing and opening modes. The predicted crack angle is more correlated to the variation of K_{II} rather than to K_I. Indeed, K_{II} varies by 110 % in the whole crack length range whereas K_I changes by only 41%. The largest crack angle (θ=20 °) is predicted at the shortest distance from the hole. Change in the crack angle is correlated to the variation of K_{II}/K_I as suggested by equation 19a.

Figure 9 shows the evolution of the principal stress distribution as function of crack growth. In the case of a pure opening mode (sample with no hole), the stress remains symmetric with respect to the crack direction, when the crack direction is perpendicular to the loading direction. In our case, the presence of the hole alters such a symmetry as depicted in Figure 9a. Note also the stress concentration at the crack tip.

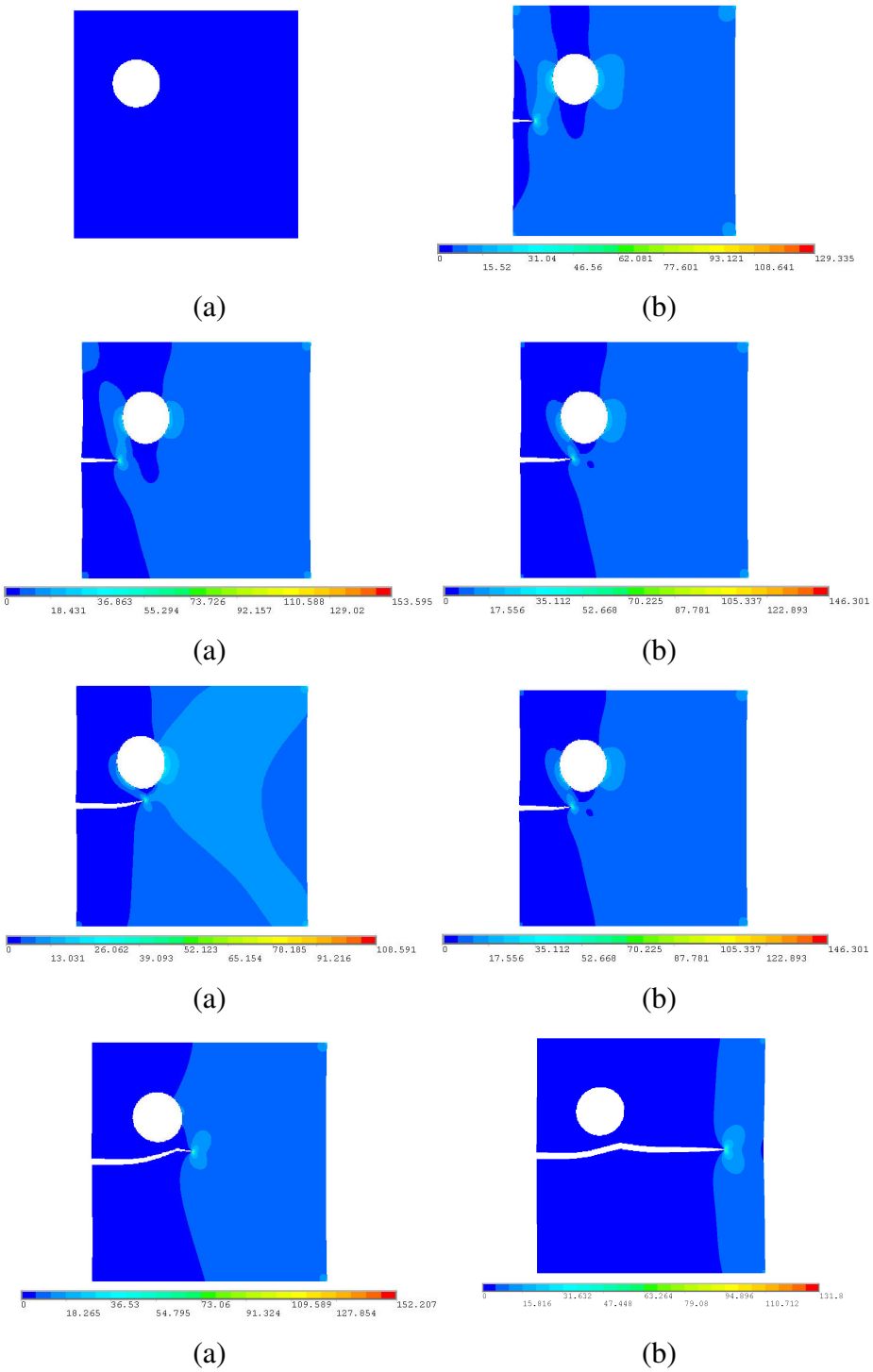

Figure 9. *Principal stress distribution as function of crack growth.*

As the crack approaches the hole, the stress distribution evolves significantly especially because of the stress concentration at the hole circumference and the modification of the crack path. When the crack bypasses the hole (Figure 9g, 9h), the stress symmetry is partially restored.

6. Conclusions

The following conclusions can be drawn at the light of the numerical and experimental analysis

- Brittle starch failure is driven by unstable crack growth leading to complete failure of the material unless crack is stopped at a particular defect.
- The presence of an heterogeneity, here a hole, modifies the stress distribution in the material which leads to local mixed mode and in turn to crack path changes. The numerical analysis of the ratio K_{II}/K_I (<20%) demonstrates that the opening mode is still the major contributor in triggering the crack direction.
- The critical stress intensity factor for which crack extension starts is close to 0.5 $MPa.m^{0.5}$. Numerical simulation provides thus an efficient tool to predict such quantity even in the case of complex loading and geometry.
- The maximum energy release rate criterion is effective to predict the crack growth giving adequate meshing conditions.
- Crack branching is observed in brittle, amorphous and dense starch material, but the present model cannot handle such instability. Reliable predictions are mostly related to kinetic considerations and our ability to measure changes in crack growth velocity. Such a work is not undertaken here because of inadequate crack propagation criteria.

In a future work, extension of the present model will be undertaken in the case of cellular products.

Acknowledgements

The authors are grateful for the help provided by Roselyne Desirest and Laurent Chaunier (BIA –INRA, France) for the technical assistance in sample preparation.

References

[1] Lucas PW, Prinz JF, Agrawal KR, Bruce IC. Food physics and oral physiology. Food Quality and Preference. 2002;13(4):203-213.

[2] Luyten A, Pluter JJ, van Vliet T. Crispy/crunchy crusts of cellular solid foods: A literature review with discussion J Texture Stud. 2004;35(5):445-492.

[3] Heath MR. The oral measurement of food: the bases of oral success and for understanding the sensations that drive us to eat. Food Quality and Preference. 2002;13:453-461.

[4] Jalabert-Malbos ML, Mishellany-Dutour A, Woda A, Peyron MA. Particle size distribution in the food bolus after mastication of natural foods. Food Quality and Preference. 2007;18(5):803-812.

[5] Baragar FA, van der Bilt A, van der Glas HW. An analytic probability density for particle size in human mastication. Journal of Theoretical Biology. 1996;181(2):169-178.

[6] Guessasma S, Babin P, Della Valle G, Dendievel R. Relating cellular structure of open solid food foams to their Young's modulus : finite element calculation. International Journal of Solids and Structures. 2008;45(10):2881-2896.

[7] Griffith AA. The Phenomena of Rupture and Flows in Solids. Transactions of the Royal Society. 1921;221:163-167.

[8] Perez N. Fracture mechanics. Boston: Kluwer Academic Publishers, 2004.

[9] Gdoutos EE. Fracture mechanics: An introduction. Dordrecht: Springer, 2005.

[10] Irwin GR. Analysis of stresses and strains near the end of a crack traversing a plate. Journal of applied mechanics. 1957;79:361.

[11] Ravi-Chandar K. Dynamic fracture of nominally brittle materials. International Journal of Fracture. 1998;90(2):83-102.

[12] Qian J, Fatemi A. Mixed mode fatigue crack growth: A literature survey Engineering Fracture Mechanics 1996;55:969-990.

[13] Sutton MA, Deng X, Ma F, Newman JC, James M. Development and application of a crack tip opening displacement-based mixed mode fracture criterion. International Journal of Solids and Structures. 2000;37:3591-3618.

[14] Nuismer RJ. Energy-release rate criterion for mixed mode fracture. International Journal of Fracture. 1975;22(3):245-250.

[15] Gao X, Kang X, Wang H. Dynamic crack tip fields and dynamic crack propagation characteristics of anisotropic material. Theoretical and Applied Fracture Mechanics. 2009;51:73-85.

[16] Grégoire D, Maigre H, Réthoré J, Combescure A. Dynamic crack propagation under mixed-mode loading - Comparison between experiments and X-FEM simulations. International Journal of Solids and Structures. 2007;44:6517-6534.

[17] Ichikawa M. Reliability evaluation of brittle solids under polyaxial stress states based on maximum energy release rate criterion. Engineering Fracture Mechanics. 1995;51:629-635.

[18] Soh A, Bian, LC,. Mixed mode fatigue crack growth criteria. International Journal of Fatigue 2001;23:427-439.

[19] Yosibash Z, Priel E, Leguillon D. A failure criterion for brittle elastic materials under mixed-mode loading. International Journal of Fracture. 2006;141(1-2):291-312.

[20] Ayatollahi MR, Aliha MRM. Mixed mode fracture in soda lime glass analyzed by using the generalized MTS criterion. International Journal of Solids and Structures. 2009;46(2):311-321.

[21] Mall S, Murphy JF, Shottafer JE. Criterion for mixed-mode fracture in wood. Journal of Engineering mechanics-ASCE. 1983;109(3):680-690.

[22] Lebaillif D, Recho N. Brittle and ductile crack propagation using automatic finite element crack box technique. Engineering Fracture Mechanics. 2007;74(11):1810-1824.

[23] Azócar D, Elgueta M, Rivara MC. Automatic LEFM crack propagation method based on local Lepp-Delaunay mesh refinement. Advances in Engineering Software. 2009;41(2):111-119.

[24] Giner E, Sukumar N, Denia FD, Fuenmayor FJ. Extended finite element method for fretting fatigue crack propagation. International Journal of Solids and Structures. 2008;45(22-23):5675-5687.

[25] Rabczuk T, Song J-H, Belytschko T. Simulations of instability in dynamic fracture by the cracking particles method. Engineering Fracture Mechanics. 2009;76(6):730-741.

[26] Song J-H, Belytschko T. Cracking node method for dynamic fracture with finite elements. Int J Numer Meth Engng. 2009;77:360–385.

[27] Dejak B, Mlotkowski A, Romanowicz M. Finite element analysis of mechanism of cervical lesion formation in simulated molars during mastication and parafunction. The Journal of Prosthetic Dentistry. 2005;94(6):520-529.

[28] Gudimetla P, Yarlagadda PKDV. Finite element analysis of the interaction between an AWJ particle and a polycrystalline alumina ceramic. Journal of Achievements in Materials and Manufacturing Engineering. 2007;23(1):7-14.

[29] Lee HC, Choi JS, Jung KH, Im YT. Application of element deletion method for numerical analyses of cracking. Journal of Achievements in Materials and Manufacturing Engineering. 2009;35/2:154-161.

[30] Chanvrier H, Colonna P, Della Valle G, Lourdin D. Structure and mechanical behaviour of corn flour and starch-zein based materials in the glassy state. Carbohydrate Polymers. 2005;59(1):109-119.

[31] Howard K, Dana M. ASM Handbook: Mechanical Testing and Evaluation. ASM International, 2000.

[32] Hasebe N, Wang X, Kondo M. Interaction between crack and arbitrarily shaped hole with stress and displacement boundaries. International Journal of Fracture. 2003;119(1):82-102.

[33] Chudnovsky A, Ma J, Ivanova E, Shulkin Y, Shlyapobersky J. Rate sensitivity of fracture trajectory. International Journal of Rock Mechanics and Mining Sciences. 1997;34(3-4):287.e281-287.e217.

[34] Sherman D. Branching in constrained brittle layers. Scripta Materialia. 1997;37(12):1939-1944.

[35] Sharon E, Gross SP, Fineberg J. Local crack branching as a mechanism for instability in dynamic fracture. Physical Review Letters. 1995;74(25):5096-5099.

[36] Ravi-chandar K, Knauss WG. An experimental investigation into dynamic fracture 3. On steady-state crack-propagation and crack branching. International Journal of Fracture. 1984;26(2):141-154.

[37] Vere-jones D. branching model for crack propagation. Pure and Applied Geophysics. 1976;114(4):711-725.

[38] Linder C, Armero F. Finite elements with embedded branching. Finite Elements in Analysis and Design. 2009;45(4):280-293.

[39] Nguyen TD, Klein PA. A study of dynamic crack instabilities using cohesive continuum methods. 11th International Conference on Fracture. Turin, Italy; 2005.

[40] Gao H. A theory of local limiting speed in dynamic fracture. Journal of The Mechanics and Physics of Solides. 1996;44(9):1453-1474.

Partie 2

Modélisation par éléments finis de la propagation de la fissure dans des extrudé a base d'amidon de faible densité

Article.2

Finite element modelling of crack propagation in carbohydrate extruded starch with open void structure

Hedjazi L, Guessasma S, Della Valle G, Benseddiq N. Finite element modelling of crack propagation in carbohydrate extruded starch with open void structure. Carbohydrate Polymers;83(4):1696-1706

Finite Element modelling of crack propagation in carbohydrate extruded starch with open void structure

L. Hedjazi[1] , S. Guessasma[1]* , G. Della Valle[1], N. Benseddiq[2]

[1]Research Unit BIA, INRA, Rue de la Géraudière, Nantes 44130, France

[2]Laboratory of mechanics of Lille (UMR CNRS 8107), University of Lille 1, BP179 59653 Villeneuve d'Ascq, France

* Corresponding author

Phone. +33 (0)2 40 67 50 36, fax.+33(0)2 40 67 51 67

E-mail address: sofiane.guessasma@nantes.inra.fr

1. Abstract

This study presents a new way of describing the void architecture of a carbohydrate polymer to allow the simulation of crack propagation in extruded starch material. In these materials, complex stress distribution takes place upon loading leading to a jagged crack extension. Based on the principle of stress intensity factors, the maximum energy release criterion is implemented and combined with a particular 2D meshing of the material. The meshing is based on a modification of the element connectivity in a regular grid. A material property is assigned to each element based on grey level of acquired images of the carbohydrate material. The numerical results show that the void structure is responsible for the development of a local mixed mode. Crack propagation exhibits significant changes in the crack path because of the heterogeneous stress distribution. The comparison between numerical and observed crack paths well shows that the predictions are sensitive to grey level distributions and mesh refinement. Finally, the criterion is able to predict nicely the crack extension if the contrast between bright and dark regions is properly addressed.

Keywords

Extrusion; carbohydrate material; starch; fracture; finite element analysis.

2. Introduction

Extrusion is a popular way of food processing (Guy, 2001; Ho, Karwe & Kokini, 1991) allowing the design of food products with a wide diversity of textures and formulations, such as breakfast, snacks. Starch is the basic ingredient in such products. Its extrusion leads to the

creation of a foam solid as a result of the expansion during processing (Babin, Della Valle, Dendievel, Lourdin & Salvo, 2007). The resulting void architecture of the carbohydrate polymer depends on the processing conditions and, in turn, significantly affects the texture of the designed product (Babin, Della Valle, Dendievel, Lourdin & Salvo, 2007 ; Wilkinson, Dijksterhuis & Minekusy, 2000). One of the targeted functional properties is the size reduction of the product during mastication (Lucas, Prinz, Agrawal & Bruce, 2002; Voon, Lucas, Chew & Luke, 1986). Such feature is intimately related to the texture of the food product and undoubtedly to its mechanical properties. There was a considerable effort dedicated to the study of the relation between the mechanical properties of the designed food and the mastication performance (Dan & Kohyama, 2007). Finite element computation has also been considered for the study of the oral (i.e., physiology of mastication) process (Dejak, Mlotkowski & Romanowicz, 2003; Rohrle & Pullan, 2007).These studies are, however, limited to the analysis of the stress state in teeth and jaws for particular loading conditions (Ichim, Kieser & Swain, 2007; Reina, Garcıa-Aznar, Domınguez & Doblare, 2007).

More importantly, the mechanical behaviour of the chewed product is either completely ignored or roughly approximated in several approaches (Okada, Honma, Nomura & Yamada, 2007; Turker, Sowman, Tuncer, Tucker & Brinkworth, 2007; Xu, Kuhnert, Foster, Bronlund, Potgieter & Diegel, 2007). For example, macroscopic homogeneity of the mechanical properties is often assumed but we know that the food transformation process induces a complex structure with a non-homogeneous distribution of mechanical properties.

A better understanding of food failure under real mastication conditions would certainly require a deeper analysis of the rupture of the studied carbohydrate material. There is a huge body of work in that area, within a more general context related to the mechanics of cellular materials. In our specific case, the cell structure refers to the highly porous starch material.

One of the most known result is that the compression behaviour of the cellular material is quite different from its tensile behaviour (Gibson & Ashby, 1997). For the former one, the deformation mechanism is basically determined by the crushing of cells. This mechanism can be approached using linear elastic fracture mechanics. If the material rupture is brittle, the rupture can be anticipated using single crack growth.

This hypothesis is not quite restrictive in the context of mastication. Several studies show that food compression results in significant bending of the food part and consequently to the development of an opening mode (Dejak, Mlotkowski & Romanowicz, 2003; Lucas, Prinz, Agrawal & Bruce, 2002).

In such a way, the fracture behaviour of cellular food products was also studied (Babin, Della Valle, Dendievel, Lourdin & Salvo, 2007 ; Fontanet, Davidou, Dacremont & LeMeste, 1997; Kirby & Smith, 1998; Primo-Martin, de Beukelaer, Hamer & van Vliet, 2008; Sandoval, Chaunier, Courcoux & Della Valle, 2008). One of the major result is related to the effect of the void ratio ϕ on the critical stress intensity factor (Gibson & Ashby, 1997)

$$K_{IC} \propto \sigma_{fs} \rho^{n} \qquad (1)$$

where K_{1C} is the critical stress intensity factor (the fracture toughness), σ_{fs} is the fracture stress of the intrinsic material composing the cell wall, $\rho = 1 - \phi$ is the relative density. n is an exponent equal to 1.5, for a regular array of cells.

Choi and co-workers (Choi & Sankar, 2005) report values for n in the range 0.79 – 1.1 depending on the cell length and strut thickness using numerical simulations.

Equation (1) has a more general validity and does not prejudge of the nature of the cellular material. However, this equation considers only a microstructure descriptor as affecting a mechanical property. And even so, the property is expected to vary by the action of other descriptors such as cell wall size distribution, variability of the wall properties, among other effects.

The fracture toughness in equation (1) determines when a crack is expected to propagate under given loading conditions. However, it is not informative about the crack trajectory unless to consider adequate criteria that combine the stress state around the crack tip and the elastic energy expression using Hook's law. Crack trajectory is related to the fragmentation stage in the mastication process, and thus requires a particular attention.

Within this context, a finite element approach is developed to account for the explicit effect of the void structure of extruded starch on the crack propagation.

Crack propagation has been widely studied, but we focus, in the following, on the literature dealing with the topic of heterogeneous materials where unstable crack growth is microstructural dependent. The most available literature on this topic concerns randomly structured materials such as concrete, fibrous and particulate composites (Bazant, 1997; Guarino, Garcimartin & Ciliberto, 1998; Jenq & Shah, 1988). The topic of cellular materials has also covered the fracture mechanics (Choi & Sankar, 2005; Schmidt & Fleck, 2001; Thuvander, Jernkvist & Gunnars, 2000) but with more focus on fatigue failure analysis (Ingraham, DeMaria, Issen & Morrison, 2009; Kanny, Mahfuz, Carlsson, Thomas & Jeelani, 2002; Motz, Friedl & Pippan, 2005; Vendra, Neville & Rabiei, 2009), damage (Lipperman,

Ryvkin & Fuchs, 2007a; Taylor, Hazenberg & Lee, 2003; Wittel, Dill-Langer & Kroplin, 2005) and crack propagation criteria (Dillard, Forest & Ienny, 2006).

From the computational viewpoint, crack propagation has been studied in random materials using lattice or discrete element models (Belytschko, Organ & Gerlach, 2000; Schlangen & Garboczi, 1996, 1997; Wittel, Dill-Langer & Kroplin, 2005). The main principle behind is the discretisation of the material by means of 1D elements (in a 2D microstructure) that exchange forces and can be thus eliminated when a given criterion is satisfied. Such method is mesh dependent and the results are considerably dependent on the fracture criterion. Finite element computation was extensively used for the study of unstable crack propagation. Damage based approaches such as cohesive models have been implemented (Cornec, Scheider & Schwalbe, 2003; Gasser & Holzapfel, 2005; Wu & Yin, 2003). The technique is able to cope with stress singularity considering a few number of parameters that can be adjusted based on experimental observation (Cendon, Galvez, Elices & Planas, 2000). The success of the cohesive model is based on the choice of the traction – separation law, but the model remains phenomenological. Some refinement of the method has been introduced based on a cohesive interaction law that accounts for nonlinearities and surface energy effects in nanomaterials (Gao & Ji, 2003). Micromechanical models have been used to determine the failure of heterogeneous materials by knowing the spatial distribution of mesoscale heterogeneity (Thuvander, Jernkvist & Gunnars, 2000; Zhu & Tang, 2004). Other finite element approaches are more based on damage formulation (Geers, de Borst & Peerlings, 2000). Finally, efficient techniques exploiting computer graphics such as cellular automata were also considered for the simulation of 3D crack patterns (Gobron & Chiba, 2001).

The heterogeneous structure has a significant effect on the crack propagation. Size effects have been identified leading for example to the concept of crack fractality (Bazant, 1997; Morel, Bouchaud, Schmittbuhl & Valentin, 2002). Fracture toughness in cellular materials is, in this way, dependent on the cell size (Gibson & Ashby, 1997). Size effects introduce a limitation in the study of crack propagation in cellular materials. Indeed, the analysis of the discrete cell rupture using continuum mechanics supposes that the crack length is some order of magnitude larger than the cell size.

In this paper, crack propagation in starch porous material is studied accounting for the following developments:

- In our Finite Element model, we assign to each element material properties based on the observed grey level associated to the void structure of starch material. This principle is used in several computational approaches aiming at implementing material properties related to some information about the heterogeneous microstructure (Chiaia, Vervuurt & VanMier, 1997; Prado & van Mier, 2003; Thuvander, Jernkvist & Gunnars, 2000; Zhu & Tang, 2004). This technique contrasts with the approaches using the description of cellular materials as regular assemblies of beam elements (Choi & Sankar, 2005; Lipperman, Ryvkin & Fuchs, 2007b; Ryvkin, Fuchs, Lipperman & Kucherov, 2004; Schmidt & Fleck, 2001).
- We use a regular meshing combined with a specific element connectivity to avoid extensive computation with remehsing. Our technique allows thus a non-prescribed crack propagation with no need to special interface elements (Alfaiate, Pires & Martins, 1997).
- We use the stress intensity factors to derive our crack growth criterion. These have proved to be applicable in several cellular food products (Vincent, 2004). Among the possible criteria, we use the maximum energy release criterion.

3. Experimental layout

The raw material is a maize starch prepared using two high amylose content starches following the procedure detailed in (Della Valle, Colonna, Patria & Vergnes, 1996; Della Valle, Vergnes, Colonna & Patria, 1997). The final amylose content is 47% for the material denoted B in the same work (Della Valle, Vergnes, Colonna & Patria, 1997).

The material is processed using a Clextral BC45 twin-screw extruder (screw diameter 56 mm, screw length 1 m). The processing conditions are fixed as follows: screw rotation speed 166 rpm, feed rate 33.4 kg/h, added water during feeding 27.5%. Under these conditions, the product temperature in the die channel is 167 °C, whereas the specific mechanical energy is 167 Wh/kg. More details about the processing procedure can be found in (Babin, Della Valle, Dendievel, Lourdin & Salvo, 2007 ; Della Valle, Colonna, Patria & Vergnes, 1996; Della Valle, Vergnes, Colonna & Patria, 1997). The final moisture of the extruded material is adjusted to 12% thanks to long duration storage under a controlled environment (relative humidity 60% over saturated NaBr salt and temperature 20°). Samples, regular in shape, of dimensions 30x 10x t mm^3 are carefully machined using a circular saw (thickness = 0.1 mm) from the extruded ribbons for mechanical testing, where t is the material thickness varying between 1.4 to 3.0 mm. The relative density of the material is 0.22 as indicated by the

measured densities of the dense (ρ=1400 kg/m^3) and the extruded (ρ =424 kg/m^3) materials. The overall void content of the material is thus about 70%.

Mechanical testing is undertaken using a micro-mechanical testing machine capable of micro level displacement. The load cell has a peak force of ±125 N with an accuracy of 0.25N. The driving system is composed of two synchronised motors ensuring a displacement accuracy of 1.25 µm. Traction is performed on notched specimens. Samples are fixed by a drop of super glue onto the fixtures. The gauge length is adjusted to about 10 mm (Figure 1a).

Tensile loading is performed at a constant displacement rate of 40 µm.s^{-1} and up to material failure. Mechanical testing is coupled to image acquisition using a digital camera with a recording rate of 100 frames per seconds. The frame size is adjusted to allow sample observation with a fine resolution and as large as possible Region Of Interest (ROI). For this purpose, the digital camera is mounted on stereomicroscope (Figure 1b). Figure 1a shows the dimensions of the ROI (Region Of Interest) as well as the loading conditions. Typically, for a ROI of 10 mm length, the pixel size is about 33 µm.

4. Numerical technique

4.1. Crack propagation criterion

In order to define the crack propagation criterion for the studied carbohydrate polymer, we use the concept of the J integral (Gdoutos, 2005) introduced by Rice (Rice, 1968). Following the definition of the J integral in the case of a mixed mode analysis (Saouma, 2008)

$$J_1 = \int_{\Omega}\left[\Gamma dy - \mathbf{t}\frac{\partial \mathbf{u}}{\partial x}\right]ds \qquad (2)$$

$$J_2 = \int_{\Omega}\left[\Gamma dx - \mathbf{t}\frac{\partial \mathbf{u}}{\partial y}\right]ds \qquad (3)$$

where Ω is a contour surrounding the two-dimensional crack. Γ is the strain energy density, **u** is the displacement vector, **t** is the traction vector along the unit vector **n**, which is perpendicular to the path defined by the contour.

J_1 and J_2 represent the energy release rate for crack extensions parallel and perpendicular to the crack.

Expressing the two contour integrals as function of stress intensity factors leads to the following relationships

$$J_1 = \alpha\left(K_I^2 + K_{II}^2\right) \qquad (4)$$

and

$$J_2 = 2\alpha K_I K_{II} \quad (5)$$

with

$$\alpha = \frac{1}{E} \text{ for plane strain} \quad (6a)$$

and

$$\alpha = \frac{1-\nu^2}{E} \text{ for plane stress} \quad (6b)$$

where E and ν are Young's modulus and Poisson coefficient, respectively. K_I and K_{II} are the stress intensity factors associated to the opening and shearing modes.

The corresponding angle of propagation can be thus defined by the ratio of the energy release rates parallel and perpendicular to the crack (Hellen & Blackburn, 1975). It can be thus written as

$$\theta = \arctan\left(\frac{J_2}{J_1}\right) \quad (7)$$

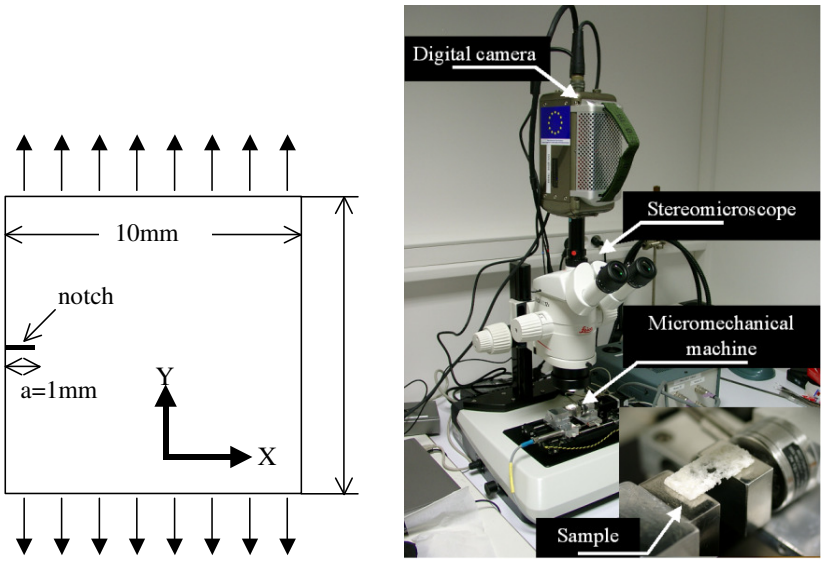

(a) (b)

Figure 1. *(a) Dimensions of the observed ROI of the carbohydrate polymer showing in particular the notch size for tensile loading experiment. (b) Experimental set-up for tensile loading of extruded samples.*

which simplifies into

$$\theta = \arctan\left(\frac{2K_I K_{II}}{K_I^2 + K_{II}^2}\right) \quad (8)$$

Equation (8) predicts the crack angle following the maximum energy release rate. Figure 2 shows the plot of θ as function of the ratio K_{II}/K_I.

4.2. Finite Element model

Images of extruded starch are meshed considering the conversion of each pixel by an 8-node plane element. The meshing is thus regular and the mesh size corresponds to the resolution of the image. The ANSYS code (ANSYS Inc, Canonsburg, Pennsylvania, U.S.A.) is used for such purpose combined with a self-written program. Plane strain state is assumed within the 2D linear elastic analysis.

The connectivity of the elements is modified to account for the possibility to propagate a crack in all possible directions (Figure 3a). Indeed, the elements do not share any of their corresponding nodes but initially all degrees of freedom of coincident nodes are coupled.

Because node decoupling in a regular square grid is limited to three angles (-90°, 0 and 90°), node decoupling is performed in a large domain corresponding to the size of the decoupling step (Figure 3b). In this study, the decoupling domain is restricted to 20x20 elements ahead the crack tip, where the physical dimension of this domain depends on the resolution of the images.

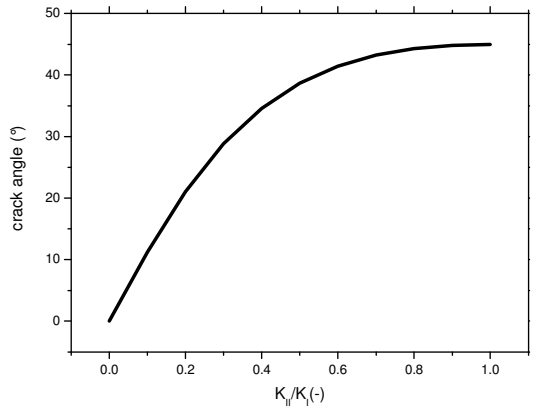

Figure 2. *Prediction of the crack propagation angle as function of the ratio of the stress intensity factors.*

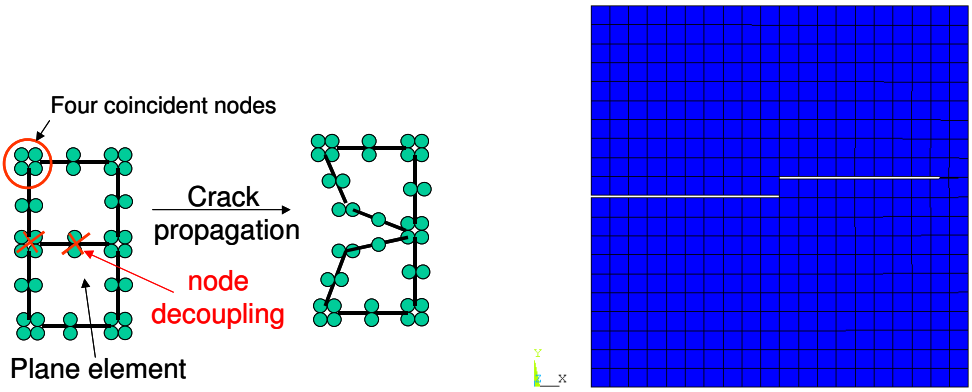

(a) (b)

Figure 3. *(a) Crack propagation using node decoupling. (b) node decoupling along a large domain allowing the crack propagation with small angles.*

In our case, the decoupling size is 667 µm for an image resolution of 300 x300 pixels. The lowest vertical displacement within the decoupling domain predicts crack extension with an angle as small as 2.79 degrees.

The material properties used in our simulation are those corresponding to isotropic elastic materials with a constant Poisson ratio (ν=0.3). Isotropy is thus assumed at the scale of the individual elements. However, Young's modulus is spatially varied in order to represent the real heterogeneity of starch material. For this purpose, the grey level of each pixel of the image corresponds to an element with a given value of Young's modulus. In such a way, a dark pixel represents an element with a large Young's modulus and vice-versa.

The conversion of the grey level into a material property assumes a linear correlation of the form

$$E_i = E_{max} + \left(\frac{E_{min} - E_{max}}{256} \right) n_i \qquad (9)$$

where i refers to the pixel index. E_{min} and E_{max} are the lower and upper limits for Young's modulus, respectively. n_i is the grey level associated to pixel i.

The linear conversion used in equation 8 can be compared to an approximation of the exponential decay of light transmission. Because of the void structure, light attenuation is linear with respect to the depth of penetration in the solid.

The upper bound of the elastic property is fixed to 140 MPa. This value is much less than the elastic modulus of the dense starch material. This value is chosen in accordance with the measured rupture force. The lower bound of the elastic modulus is varied in a large domain (from 140 MPa down to 1 Pa) to account for the sensitivity of the predicted path with regard

to the bright regions. Figure 4 shows an example of image conversion into a Finite Element model using up to 1397 material models for the carbohydrate polymer. In fact, the same model of isotropic elastic material is used each element is assigned a different value of Young's modulus.

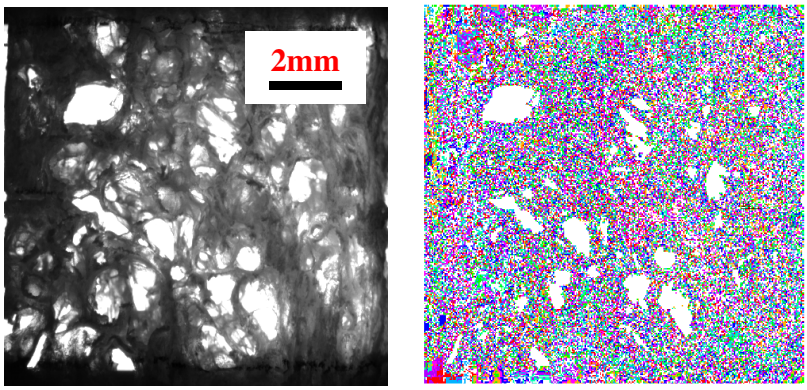

(a) (b)

Figure 4. *(a) A typical porous material and (b) the corresponding finite element mesh. Colours associated to elements represent different material properties. ROI area = 100 mm*^{2}.

Prior loading, a crack of length comparable to the measured crack size is numerically created by decoupling all those nodes belonging to the crack baseline.

The plate is loaded applying the experimental conditions. All nodes of the bottom line are constrained against displacement in X-direction whereas a structural displacement –U(t)/2 is imposed in Y-direction, where t refers to the simulation time. Nodes of the top line are displaced by a positive amount + U(t)/2 in Y-direction and the other degrees of freedom are fixed.

The elastic problem is solved using the preconditioned Conjugate Gradient PCG solver. The stress intensity factors are computed thanks to the nodal displacement results. When the imposed displacement reaches the failure value, the crack propagation is started with the implemented criterion (equation 8). Stress intensity factors are computed in the post-processing thanks to the nodal displacement field. For this purpose, five nodes are used, one corresponding to the crack tip and the nearest two backward nodes for each crack surface.

5. Results and discussion

Figure 5 shows images of the porous carbohydrate material at different stages. In Figure 5a, the crack opening is utmost and corresponds to a peak force of about 19 N (failure stress of

1.32 MPa). The loading of the material reveals a slope of about 62 MPa. This value is slightly smaller than Young's modulus of the intact specimen because of the presence of the notch. The crack opening cannot be easily distinguished because the notch intercepts a dense region.The crack propagation leads to a brittle failure of the material as attested by the abrupt decrease of the force (data not shown).

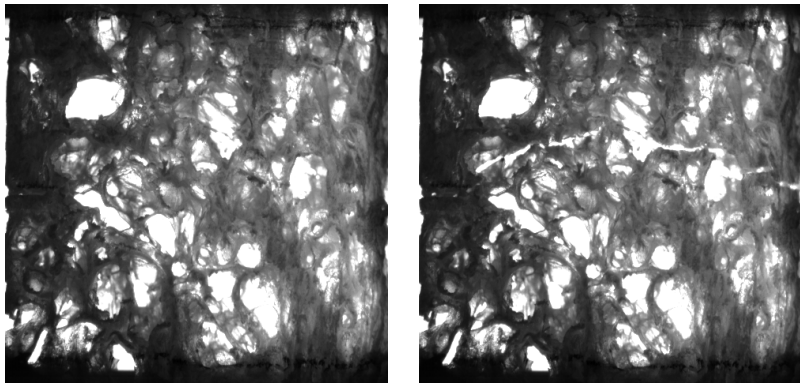

(a) crack opening b) crack propagation

Figure 5. *(a) Largest crack opening corresponding to the peak force and (b) crack propagation leading to brittle rupture of the carbohydrate porous polymer.*

Since the frame rate is fixed to 100 fps, it is not possible to estimate the velocity of the crack growth, or at least, we should say that it is beyond 1 $m.s^{-1}$. The crack trajectory is shown in Figure 5b. Despite tensile loading, the crack path is jagged. Sudden variations in crack propagation are correlated to the presence of a void structure, because such structure modifies the stress distribution at the cell walls. It is also clear that change in the crack path means the development of a local mixed fracture mode in which shearing has a non-negligible contribution. Jagged crack propagation is not specific to starch foams but it is well observed in various other porous materials (Dillard, Forest & Ienny, 2006; Hazenberg, Freeley, Foran, Lee & Taylor, 2006).

In order to underline the effect of the void structure on the crack trajectory, different values of E_{min} are used. A low bound value is suggested to increase the contrast between dark and bright regions. It is also more realistic with regards to the presence of the void structure. Figure 6 shows the predicted crack path using the maximum elastic energy release criterion for different values of E_{min}. Note that E_{max} = 140 MPa is constant for all these runs. When Emin=Emax, the material is homogeneous. The crack propagates perpendicular to the loading direction following the opening mode. This result simply indicates that $\theta=0$ when $K_{II} \to 0$.

The decrease of E_{min}, modifies significantly the crack path. The crack trajectory becomes insensitive to E_{min} below 1 KPa. The computation becomes difficult to perform because of numerical instabilities when $E_{min} \to 0$. Such instabilities are principally due to large deformations associated to elements with small Young's moduli.

The analysis of mesh sensitivity is conducted by resizing the image of the porous carbohydrate material from its original size (300x300 pixels) down to 100x100 and up to 500x500 pixels (Figures 7a – 7c). The computation of the crack path with the lowest resolution predicts a significant deviation from the original path (Figure 7d). This result is not surprising because fewer details appear with subresolutions. For those resolutions larger than 200x200 pixels, the path differences become more attenuated. When increasing further more the resolution above the original image size, we do not add additional information. However, any pixel in the original image will appear as a homogeneous domain composed of several pixels in the modified image (Figure 7c). This has a minor, but not negligible, effect on the crack path (Figure 7d).

Figure 8a depicts the numerical force – displacement response for one of the test conditions in Figure 5. Here, the simulation is performed using the original resolution (300x300 pixels). The moduli bounds for this case are as follows E_{min}= 0.001 MPa, E_{max}= 140 MPa. The crack propagation is initiated at a break elongation of 0.21 mm (failure strain of 2.1%). This value is the exactly the elongation at which material rupture is observed in Figure 5b. The corresponding numerical peak force is about 20 N, which is 5% larger than the experimental failure force. This small deviation is attributed to the selected E_{max} value, as mentioned above. Figure 8b depicts the predicted crack path using the maximum elastic energy release criterion. In this figure, evident crack changes can be classified into small and large crack angle variations. Jagged crack extension is related to the heterogeneous distribution of the elastic modulus but its magnitude of variation remains small (i.e., weak contrast of the elastic modulus). Significant path changes are particularly associated to large regions where the elastic modulus is the lowest one. These regions are efficient stress concentrators because the elastic modulus contrast is utmost. Such contrast makes these regions acting like crack traps. However, the brittle failure of the material indicates that crack traps are not effective in arresting completely the crack progress because elastic energy is still available for the complete failure of the material.

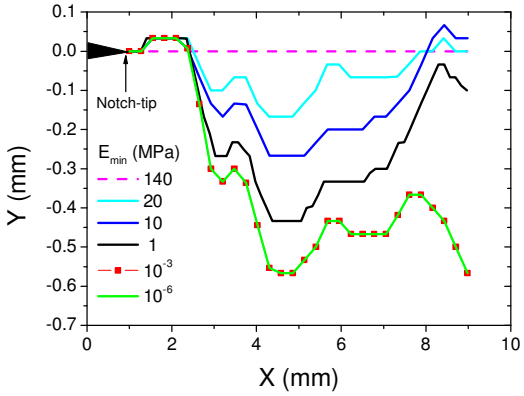

Figure 6. *Comparison between crack paths for different values of E_{min}.*

(a) (b) (c)

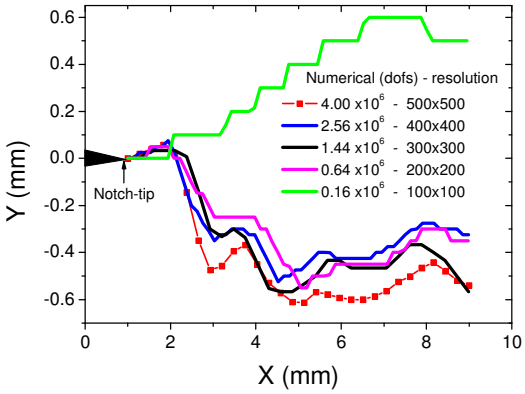

(c)

Figure 7. *(a) – (c) The same ROI observed at different resolutions (a) original 300x300 pixels (b) 100x100 pixels, (c) 500x500 pixels. (d) predicted crack propagation as function of resolution.*

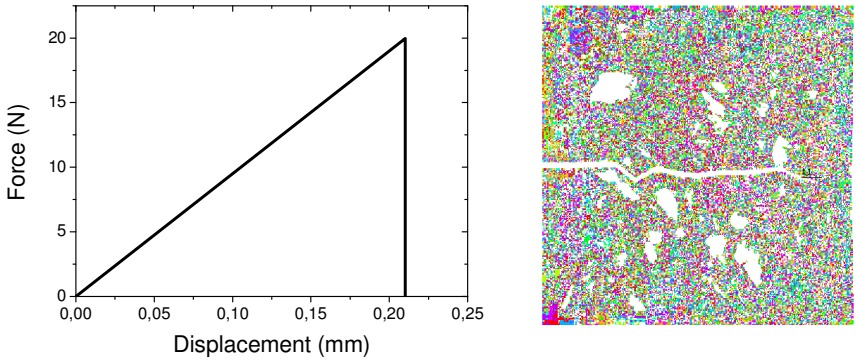

(a) (b)

Figure 8. *(a) Predicted force – displacement response using the linear elastic approximation. (b) predicted jagged crack propagation.*

Figure 9 shows the evolution of the stress distribution in the carbohydrate material as function of crack extension. In Figure 9a, the stress distribution corresponds to the largest crack opening and thus to the highest stress concentration at the crack tip before propagation. Few decoupling steps ahead, the crack orientation does not change significantly as shown in Figure 9b. The first significant change of direction in crack propagation corresponds to Figure 9c, where a significant stress concentration develops downward the crack position. The crack path remains almost normal to the loading direction (Figure 9d – 9f) as long as the crack does not encounter stress concentrators.

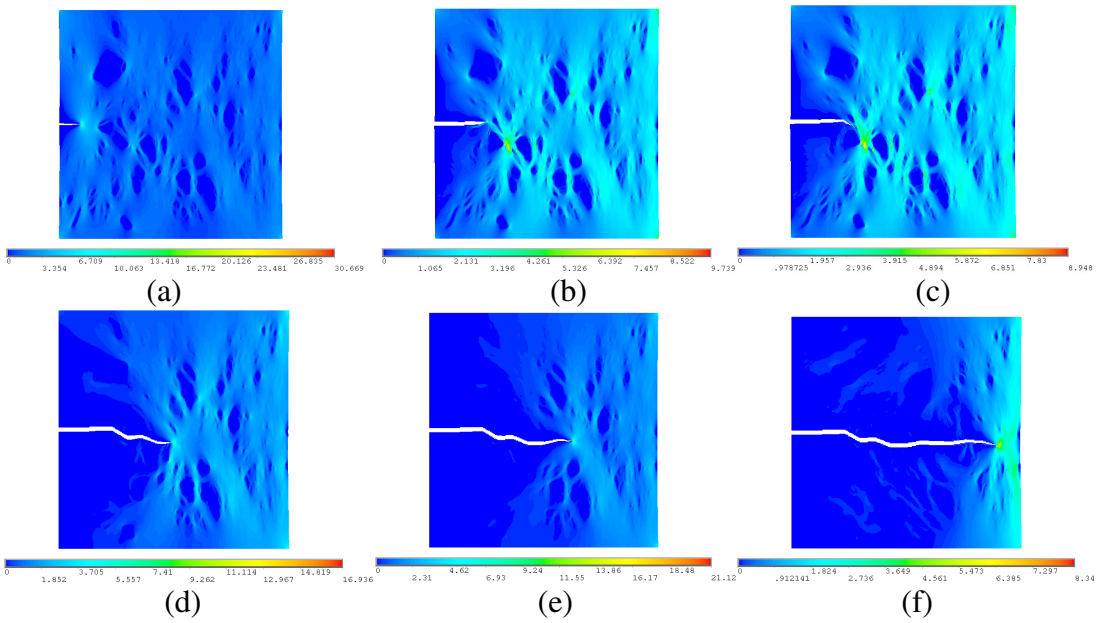

Figure 9. *Principal stress S1distribution as function of crack extension.*

The analysis of the stress intensity factors reveals that the ratio K_{II}/K_I is significantly affected by the heterogeneous void structure (Figure 10). K_{II}/K_I is found to vary in a large range from 0.003 up to 0.3. The variation of the crack angle is fully correlated to the ratio K_{II}/K_I as shown in Figure 10. The jagged character of crack propagation is inferred to the change of the predicted crack angles as a consequence of the strong local mixed mode.

The local mixed mode is strengthened at the first steps of the crack propagation (crack length < 4 mm) because of the strong spatial variability of the elastic properties. If we consider the value of K_I at those crack positions, where the opening mode is still predominant (say for example $K_{II}/K_I<0.01$), K_I fluctuates between 0.12 and 0.33 $MPa.m^{0.5}$. For different food items (Vincent, 2004), Vincent and co-workers report fracture toughness in the range 0.11 – 0.13 $MPa.m^{0.5}$ (Pérez, Saunders & Vincent, 2008; Vincent, 2004). For other cellular materials, such as carbonated apatite materials, fracture toughness is 0.14 $MPa.m^{0.5}$ (Morgan, Yetkinler, Constantz & Dauskardt, 1997).

In our case, the fracture toughness can be determined from the critical values of the stress intensity factors in which both K_I and K_{II} are contributors. Indeed, preceding results show that ,in the heterogeneous structure, both tension and shearing effects take place in the heterogeneous structure. Such determination of fracture toughness requires different testing configurations that we are not able to proceed with, and in which the critical values of K_I and K_{II} can be separately determined. Numerical attempts have been considered for the determination of the mixed mode crack toughness by changing the loading conditions numerically (Choi & Sankar, 2005), but such studies have unfortunately no experimental validation.

Any combination of K_I and K_{II} in Figure 10 must lead to an expression that is larger than the fracture toughness. This condition states the unstable crack propagation for our brittle material. Moreover, few expressions of fracture toughness are available in the case of a mixed mode fracture (Perez, 2004). The reason is that we did not expect shearing effect to develop when measuring the critical value of K_I using tensile loading.

The results shown in Figure 10 well demonstrate that the prediction of the crack path is dependent on how accurate is our description of the void environment of the crack.

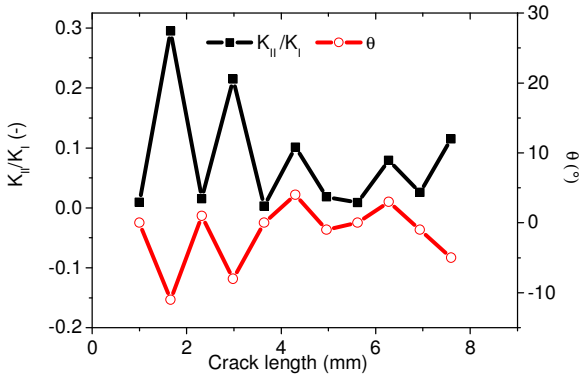

Figure 10. *Ratio of stress intensity factors and predicted crack angle as function of crack position.*

In order to describe the effect of such environment on the crack propagation, several porous structures exhibiting different grey level histograms are tested (Figure 11a). The histogram associated to Sample A corresponds to the porous material shown in Figure 13a. In this case, the pixel frequency of the bright regions is the highest one. Bright regions become less frequent as we move from sample A to sample D.

Figure 11b exhibits the predicted crack paths for the considered carbohydrate porous materials. The highest jagged path corresponds to material A, exhibiting the largest contrast between the dark and bright regions. In this case, the mixed mode is strengthened because of the stress heterogeneities. Materials C and D are characterised by predicted paths close to the horizontal line, which indicates a predominant opening mode.

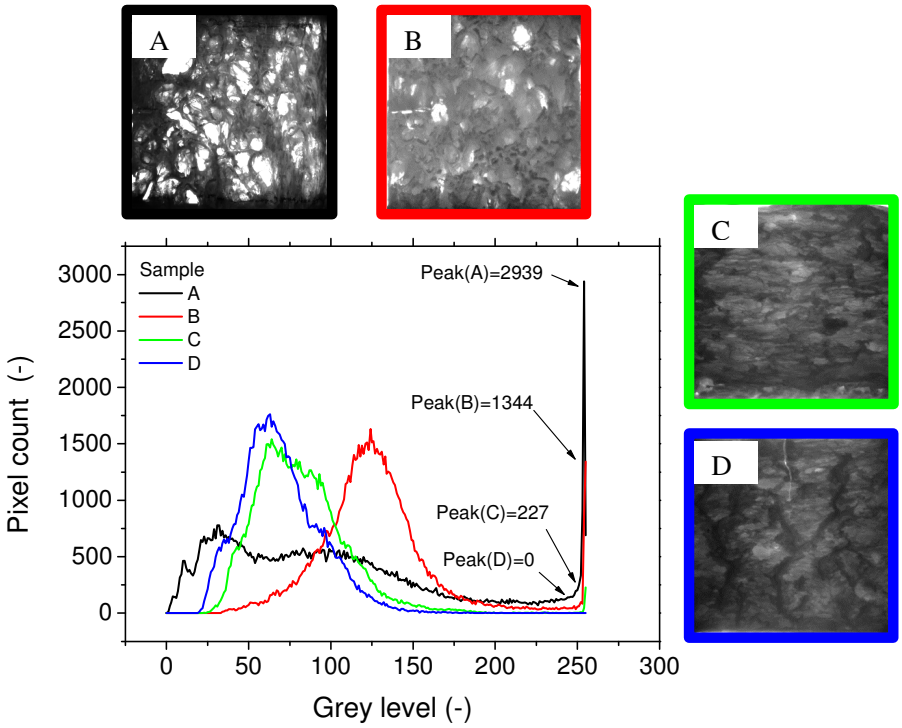

(a)

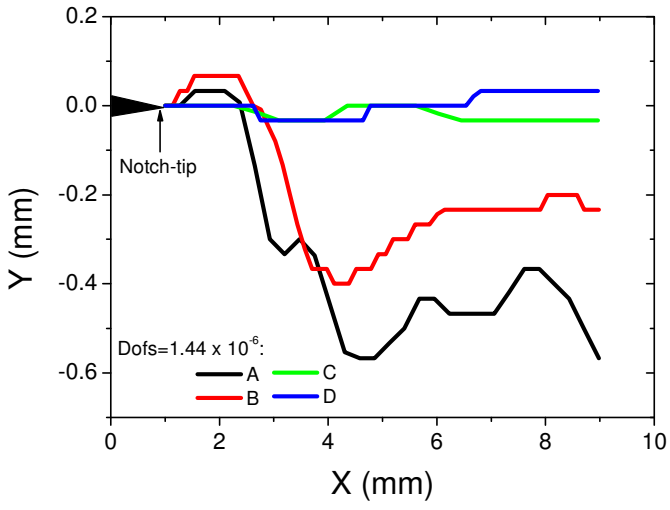

(b)

Figure 11. *Effect of void structure: (a) Grey-level histograms and (b) the predicted crack paths.*

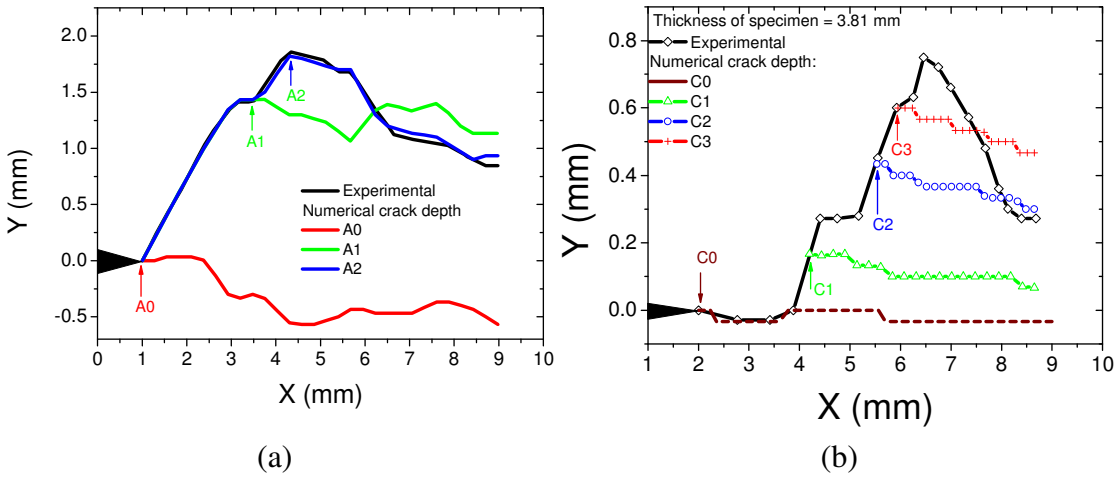

Figure 12. *Comparison between experimental and numerical crack paths for different numerical initial crack positions for two porous carbohydrate materials exhibiting (a) large and (b) low contrast of material properties.*

We can confirm, at this stage, that the contrast between dark and bright regions modulates the mixed mode propagation.

When comparing the experimental (Figure 5b) and numerical (Figure 9f) crack paths, a significant discrepancy is pointed out. Indeed, the numerical model is not able to predict accurately the first crack propagation increments. The crack trajectory in Figure 5b remains far above the predicted one. The numerical model fails in predicting significant angle variation in those regions with no evident contrast of material properties. This is precisely the case of the first crack position increments where the presence of a dark region indicates local changes in void structure. Under these circumstances, the true crack propagation can only be approached if 3D crack propagation is considered.

In order to validate our numerical approach, crack propagation is simulated for different crack sizes. The crack tip position corresponds in each run to the real observed position. The purpose here is to increase the initial crack size until adequate matching is found between the numerical and experimental crack trajectories. Figure 12 compiles the predicted results for two materials exhibiting distinct contrasts A and C. In Figure 12a are shown the various paths related to sample A. The first configuration (notch-tip A0) corresponds to the case described above in Figure 9. When extending the crack position to about 3.5 mm (notch tip A1), there are still differences in crack trajectories. If the crack tip position is increased further (notch tip A2), the numerical model is able to predict adequately the crack extension.

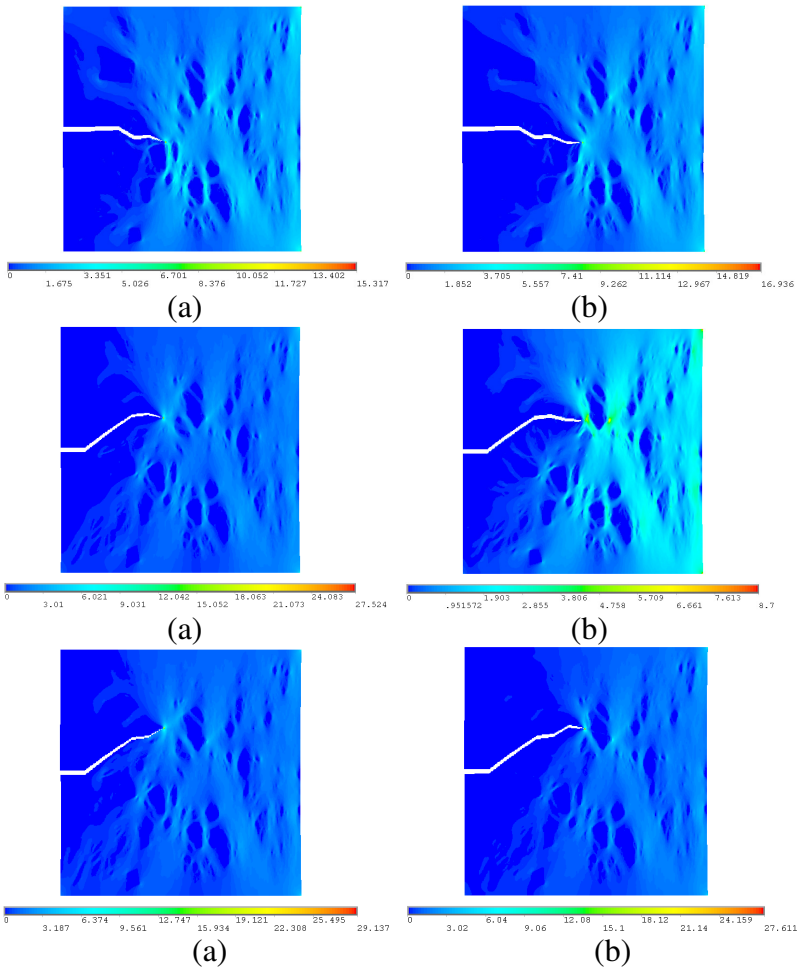

Figure 13. *Evolution of the principal stress S1 distribution at two successive steps: x= 4.1 mm for (a), (c) and (e), whereas x= 4.7 mm for (b), (d) and (f) for three different notch configurations: (a) – (b) notch-A0, (c) – (d) notch-A1, (e) – (f) notch-A2.*

Figure 12b shows the path corrections in the case of material C. Because of the low contrast, any correction (notch-tip C1 to C3) is not able to predict significant variations in the crack path because stress heterogeneities are not properly described.

Figure 13 compares the stress distribution evolutions for the crack configurations treated in Figure 12a. Figures 13a-13b correspond to the case where no path correction is performed (notch-A). We see for the notch-A1 (Figure 13c-13d) that the simulated crack path propagates towards the bottom periphery of a stress concentrator, where the stress levels are higher. The crack propagates along this periphery, predicting a lower position compared to the experimental path. When correcting the crack position using notch-A2 (Figures 13e-13f), the stress distribution around the heterogeneity is modified. The crack trajectory seems then more accurate and closer to experimental one.

6. Conclusions

- Within the context of linear elastic fracture analysis, a regular meshing is successfully considered for the prediction of small crack angle variation in a carbohydrate porous material. The angle accuracy depends on the size of the crack increment weighted by the resolution of the image acquisition.
- The description of the porous carbohydrate material in terms of spatial heterogeneous distribution of material properties explains most variations of crack trajectories observed experimentally.
- The development of a strong local mixed mode is dependent on the local material properties contrast. The presence of stress concentrators contributes in changing significantly the crack trajectory; this change is all the more significant as the crack tip is close to these regions with a high stress level.
- The maximum energy release criterion is able to predict the true crack trajectory if the image contrast remains informative of the void structure. A large contrast between bright and dark regions in the porous materials contributes to strengthen the mixed mode.
- The jagged character of crack propagation in the studied starch porous material is correlated to a large variations of the stress intensity factor ratio. This quantity is found to vary in a wide range from 0.003 up to 0.3, whereas K_I changes between 0.12 and 0.33 $MPa.m^{0.5}$.

References

Alfaiate, J., Pires, E. B., & Martins, J. A. C. (1997). A finite element analysis of non-prescribed crack propagation in concrete. *Computers & Structures, 63*(1), 17-26.

Babin, P., Della Valle, G., Dendievel, R., Lourdin, D., & Salvo, L. (2007). X-ray tomography study of the cellular structure of extruded starches and its relations with expansion phenomenon and foam mechanical properties. *Carbohydrate Polymers, 68*(2), 329-340.

Bazant, Z. P. (1997). Scaling of quasibrittle fracture: Asymptotic analysis. *International Journal of Fracture, 83*(1), 19-40.

Belytschko, T., Organ, D., & Gerlach, C. (2000). Element-free Galerkin methods for dynamic fracture in concrete. *Computer Methods in Applied Mechanics and Engineering, 187*(3-4), 385-399.

Cendon, D. A., Galvez, J. C., Elices, M., & Planas, J. (2000). Modelling the fracture of concrete under mixed loading. *International Journal of Fracture, 103*(3), 293-310.

Chiaia, B., Vervuurt, A., & VanMier, J. G. M. (1997). Lattice model evaluation of progressive failure in disordered particle composites. *Engineering Fracture Mechanics, 57*(2-3), 301-+.

Choi, S., & Sankar, B. V. (2005). A micromechanical method to predict the fracture toughness of cellular materials. *International Journal of Solids and Structures, 42*(5-6), 1797-1817.

Cornec, A., Scheider, I., & Schwalbe, K. H. (2003). On the practical application of the cohesive model. *Engineering Fracture Mechanics, 70*(14), 1963-1987.

Dan, H., & Kohyama, K. (2007). Interactive relationship between the mechanical properties of food and the human response during the first bite. *Archives of Oral Biology, 52*, 455-464.

Dejak, B., Mlotkowski, A., & Romanowicz, M. (2003). Finite element analysis of stresses in molars during clenching and mastication. *Journal of Prosthetic Dentistry, 90*(6), 591-597.

Della Valle, G., Colonna, P., Patria, A., & Vergnes, B. (1996). Influence of amylose content on the viscous behaviour of low hydrated molten starches. *Journal of Rheology, 40*, 347-362.

Della Valle, G., Vergnes, B., Colonna, P., & Patria, A. (1997). Relations between rheological properties of molten starches and their expansion behaviour in extrusion. *Journal of Food Engineering, 31*(3), 277-295.

Dillard, T., Forest, S., & Ienny, P. (2006). Micromorphic continuum modelling of the deformation and fracture behaviour of nickel foams. *European Journal of Mechanics a-Solids, 25*(3), 526-549.

Fontanet, I., Davidou, S., Dacremont, C., & LeMeste, M. (1997). Effect of water on the mechanical behaviour of extruded flat bread. *Journal of Cereal Science, 25*(3), 303-311.

Gao, H. J., & Ji, B. H. (2003). Modeling fracture in nanomaterials via a virtual internal bond method. *Engineering Fracture Mechanics, 70*(14), 1777-1791.

Gasser, T. C., & Holzapfel, G. A. (2005). Modeling 3D crack propagation in unreinforced concrete using PUFEM. *Computer Methods in Applied Mechanics and Engineering, 194*(25-26), 2859-2896.

Gdoutos, E. E. (2005). *Fracture mechanics: An introduction*. Dordrecht: Springer.

Geers, M. G. D., de Borst, R., & Peerlings, R. H. J. (2000). Damage and crack modeling in single-edge and double-edge notched concrete beams. *Engineering Fracture Mechanics, 65*(2-3), 247-261.

Gibson, L. J., & Ashby, M. F. (1997). *Cellular solids*. Cambridge: Pergamon Press Ltd.

Gobron, S., & Chiba, N. (2001). Crack pattern simulation based on 3D surface cellular automata. *Visual Computer, 17*(5), 287-309.

Guarino, A., Garcimartin, A., & Ciliberto, S. (1998). An experimental test of the critical behaviour of fracture precursors. *European Physical Journal B, 6*(1), 13-24.

Guy, R. (2001). *Extrusion Cooking - Technologies and Applications*. Woodhead Publishing

Hazenberg, J. G., Freeley, M., Foran, E., Lee, T. C., & Taylor, D. (2006). Microdamage: A cell transducing mechanism based on ruptured osteocyte processes. *Journal of Biomechanics, 39*(11), 2096-2103.

Hellen, T. K., & Blackburn, W. S. (1975). Calculation of stress intensity factors for combined tensile and shear loading. *International Journal of Fracture, 11*(4), 605-617.

Ho, C.-T., Karwe, M. V., & Kokini, J. L. (1991). *Food Extrusion Science and Technology* CRC Press.

Ichim, I., Kieser, J. A., & Swain, M. V. (2007). Functional significance of strain distribution in the human mandible under masticatory load: Numerical predictions. *Archives of Oral Biology, 52*(5), 465-473.

Ingraham, M. D., DeMaria, C. J., Issen, K. A., & Morrison, D. J. (2009). Low cycle fatigue of aluminum foam. *Materials Science and Engineering a-Structural Materials Properties Microstructure and Processing, 504*(1-2), 150-156.

Jenq, Y. S., & Shah, S. P. (1988). Mixed-mode fracture of concrete. *International Journal of Fracture, 38*, 123-142.

Kanny, K., Mahfuz, H., Carlsson, L. A., Thomas, T., & Jeelani, S. (2002). Dynamic mechanical analyses and flexural fatigue of PVC foams. *Composite Structures, 58*(2), 175-183.

Kirby, A. R., & Smith, A. C. (1998). Impact studies on extruded food foams. *Journal of Materials Science, 23*, 2251-2254.

Lipperman, F., Ryvkin, M., & Fuchs, M. B. (2007a). Fracture toughness of two-dimensional cellular material with periodic microstructure. *International Journal of Fracture, 146*(4), 279-290.

Lipperman, F., Ryvkin, M., & Fuchs, M. B. (2007b). Nucleation of cracks in two-dimensional periodic cellular materials. *Computational Mechanics, 39*(2), 127-139.

Lucas, P. W., Prinz, J. F., Agrawal, K. R., & Bruce, I. C. (2002). Food physics and oral physiology. *Food Quality and Preference, 13*(4), 203-213.

Morel, S., Bouchaud, E., Schmittbuhl, J., & Valentin, G. (2002). R-curve behavior and roughness development of fracture surfaces. *International Journal of Fracture, 114*(4), 307-325.

Morgan, E. F., Yetkinler, D. N., Constantz, B. R., & Dauskardt, R. H. (1997). Mechanical properties of carbonated apatite bone mineral substitute: strength, fracture and fatigue behaviour. *Journal of Materials Science-Materials in Medicine, 8*(9), 559-570.

Motz, C., Friedl, O., & Pippan, R. (2005). Fatigue crack propagation in cellular metals. *International Journal of Fatigue, 27*(10-12), 1571-1581.

Okada, A., Honma, M., Nomura, S., & Yamada, Y. (2007). Oral behavior from food intake until terminal swallow. *Physiology & Behavior, 90*, 172-179.

Pérez, F. J. R., Saunders, D., & Vincent, J. F. V. (2008). Mechanical tests on crispy & crunchy foods. *Crispy Cracks Symposium*. Wageningen, the Netherlands.

Perez, N. (2004). *Fracture mechanics*. Boston: Kluwer Academic Publishers.

Prado, E. P., & van Mier, J. G. M. (2003). Effect of particle structure on mode I fracture process in concrete. *Engineering Fracture Mechanics, 70*(14), 1793-1807.

Primo-Martin, C., de Beukelaer, H., Hamer, R. J., & van Vliet, T. (2008). Fracture behaviour of bread crust: Effect of bread cooling conditions. *Journal of Food Engineering, 89*(3), 285-290.

Reina, J. M., Garcıa-Aznar, J. M., Domınguez, J., & Doblare, M. (2007). Numerical estimation of bone density and elastic constants distribution in a human mandible. *Journal of Biomechanics, 40*, 828-836.

Rice, J. R. (1968). A path independent integral and approximate analysis of strain concentration by notches and cracks *Journal of Applied Mechanics, 35*(2), 379-&.

Rohrle, O., & Pullan, A. J. (2007). Three-dimensional finite element modelling of muscle forces during mastication. *Journal of Biomechanics, 40*(15), 3363-3372.

Ryvkin, M., Fuchs, M. B., Lipperman, F., & Kucherov, L. (2004). Fracture analysis of materials with periodic microstructure by the representative cell method. *International Journal of Fracture, 128*(1-4), 215-221.

Sandoval, A. J., Chaunier, L., Courcoux, P., & Della Valle, G. (2008). Bulk mechanical behavior of commercial particle food foams. *Journal of Texture Studies, 39*(4), 405-425.

Saouma, V. E. (2008). *Lecture Notes in: fracture mechanics* University of Colorado.

Schlangen, E., & Garboczi, E. J. (1996). New method for simulating fracture using an elastically uniform random geometry lattice. *International Journal of engineering science, 34*(10), 1131-1144.

Schlangen, E., & Garboczi, E. J. (1997). Fracture simulations of concrete using lattice models: Computational aspects. *Engineering Fracture Mechanics, 57*(2-3), 319-332.

Schmidt, I., & Fleck, N. A. (2001). Ductile fracture of two-dimensional cellular structures. *International Journal of Fracture, 111*(4), 327-342.

Taylor, D., Hazenberg, J. G., & Lee, T. C. (2003). The cellular transducer in damage-stimulated bone remodelling: a theoretical investigation using fracture mechanics. *Journal of Theoretical Biology, 225*(1), 65-75.

Thuvander, F., Jernkvist, L. O., & Gunnars, J. (2000). Influence of repetitive stiffness variation on crack growth behaviour in wood. *Journal of Materials Science, 35*(24), 6259-6266.

Turker, K. S., Sowman, P. F., Tuncer, M., Tucker, K. J., & Brinkworth, R. S. A. (2007). The role of periodontal mechanoreceptors in mastication. *Archives of Oral Biology, 52*, 361-364.

Vendra, L., Neville, B., & Rabiei, A. (2009). Fatigue in aluminum-steel and steel-steel composite foams. *Materials Science and Engineering a-Structural Materials Properties Microstructure and Processing, 517*(1-2), 146-153.

Vincent, J. F. V. (2004). Application of fracture mechanics to the texture of food. *Engineering Failure Analysis, 11*(5), 695-704.

Voon, F. C. T., Lucas, P. W., Chew, K. L., & Luke, D. A. (1986). A simulation approach to undestanding the masticatory process. *Journal of Theoretical Biology, 119*(3), 251-262.

Wilkinson, C., Dijksterhuis, G. B., & Minekusy, M. (2000). From food structure to texture. *Trends in Food Science and Technology, 11*, 442-450.

Wittel, F. K., Dill-Langer, G., & Kroplin, B. H. (2005). Modeling of damage evolution in soft-wood perpendicular to grain by means of a discrete element approach. *Computational Materials Science, 32*(3-4), 594-603.

Wu, Z. S., & Yin, J. (2003). Fracturing behaviors of FRP-strengthened concrete structures. *Engineering Fracture Mechanics, 70*(10), 1339-1355.

Xu, W. L., Kuhnert, L., Foster, K., Bronlund, J., Potgieter, J., & Diegel, O. (2007). Object-oriented knowledge representation and discovery of human chewing behaviours. *Engineering Applications of Artificial Intelligence, 20*(7), 1000-1012.

Zhu, W. C., & Tang, C. A. (2004). Micromechanical model for simulating the fracture process of rock. *Rock Mechanics and Rock Engineering, 37*(1), 25-56.

Chapitre III. Mécanismes de masication

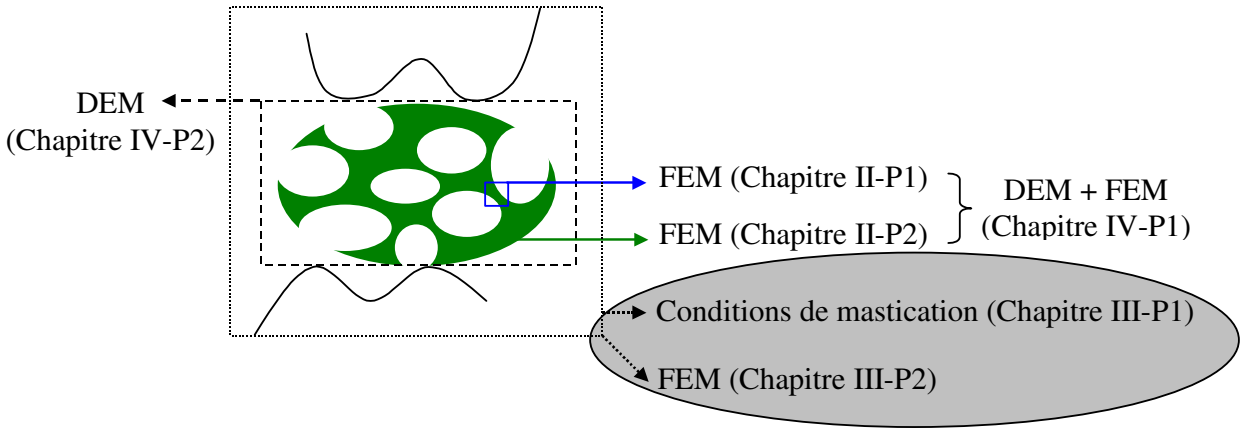

La mastication est la première étape de la digestion et son principal rôle est de préparer l'aliment pour sa déglutition, via sa déstructuration, qui, pour des aliments solides, implique des phénomènes de rupture. Chacun de ces phénomènes dépend de la texture de l'aliment et du sujet. En effet, la performance masticatoire d'un individu, habituellement évaluée par la taille de fragments d'une gomme étalon après différents cycles de mastication, dépend des caractéristiques physiologiques (état dentaire, flux salivaire, activité musculaire). Outre les propriétés mécaniques et la géométrie des aliments, la compréhension de la mécanique de la mastication nécessite donc la connaissance des forces de mastication, leur amplitude et fréquence, la trajectoire mandibulaire ainsi qu'une information précise sur le contact aliment-dents. Ces aspects font l'objet d'une étude expérimentale développée dans une première partie, dont les résultats sont utilisés dans une deuxième partie, pour aborder la modélisation de la compression d'aliment entre deux dents en tenant compte du contact aliment-dents.

Le but de la première partie, est donc de déterminer les conditions cinématiques et mécaniques qui gouvernent la déstructuration d'aliments céréaliers réels, pour un seul sujet. Ces aliments sont assimilables à des mousses solides fragiles dont les propriétés mécaniques dépendent de la structure alvéolaire. Le comportement de cinq produits céréaliers commerciaux est caractérisé en cours de mastication par un enregistrement simultané de mouvements de la mâchoire par capteurs infrarouges et de l'activité musculaire par électromyographie (EMG). La distribution de taille des particules avant déglutition est également évaluée par analyse d'images ; elle est comparée à l'évolution des variables cinématiques et EMG, telles que le nombre de cycles et la force de mastication maximale. Les résultats suggèrent que la mastication de ces aliments fragiles ne nécessite pas de cisaillement important, même à l'approche de la déglutition; la durée d'un cycle est constant et dépend assez peu de l'aliment alors que la composition (% sucre) évolue dans le même sens que la durée de la séquence ; en outre, les résultats suggèrent l'importance des premiers cycles pour la fragmentation, soulignant donc l'importance des mécanismes de rupture.

Dans une deuxième partie, il s'agit d'exploiter ces résultats pour la mise en situation numérique de l'aliment à mastiquer, à l'aide d'un modèle éléments finis (EF). Tout d'abord, les techniques d'imagerie (profilométrie, tomographie RX) sont utilisées pour déterminer, respectivement, la géométrie des molaires et la structure cellulaire de deux céréales petit-déjeuner, testées dans la première partie. Ensuite, un modèle EF de la géométrie précise de l'aliment et des dents est développé pour simuler le comportement mécanique de l'aliment lors du contact avec les dents dans la cavité buccale. Les conditions de chargement, incluant

les mouvements, normal et de cisaillement, du système buccal, sont reproduites pour chaque produit. Le modèle permet de déterminer les distributions de contraintes qui se développent lors du chargement. L'effet du cisaillement est associé à celui de la compression lors de la mastication des aliments. Une simple contrainte à la rupture de la paroi solide permet la conversion des distributions de contrainte à des fragments de l'aliment. La principale conclusion est que la fragmentation se produit plus tôt, avant l'occlusion complète et tend à produire un grand nombre de fragments, dont la taille dépend de la structure alvéolaire.

Partie 1

Fragmentation d'aliments céréaliers alvéolaires fragiles pendant la mastication.

Article.3

Mastication dynamics and related size reduction during chewing of brittle cereals foods

Mastication dynamics and related size reduction during chewing of brittle cereals foods

L. Hedjazi[1] , S. Guessasma[1]*, C. Yven[2], G. Della Valle[1], C. Salles[2]

[1]INRA, BIA, Rue de la Géraudière, Nantes 44130, France

[2]JRU INRA-CNRS CSGA, Dijon

* Corresponding author

Phone. +33 (0)2 40 67 50 36, fax.+33(0)2 40 67 51 67

E-mail address: sofiane.guessasma@nantes.inra.fr

1. Abstract

We study the masticatory behaviour of five commercial cereal products with different formulations, shape and mechanical properties. The investigation of oral behaviour consists in a simultaneous recording of jaw movement and muscle activity (EMG). We analyse the level of food degradation by considering food size distribution at the swallowing point. We compare kinematics and EMG parameters such as the number of cycles, sequence duration, mastication force and work to the resultant size distribution for the studied cereals. As expected, experimental results suggest that chewing of brittle cereals does not require significant shearing even when bolus is close to the swallowing point. Comparison between products is discussed and correlations are highlighted between oral parameters and fragment size distributions.

Keywords

Breakfast cereals, Oral parameters; jaw kinematics ; Food breakdown; Particle Size Distribution.

2. Introduction

Chewing is the first step in the process of digestion and is meant to prepare the food for swallowing and further processing in the digestive system. During chewing, food particles are reduced in size and assembled with the incorporation of saliva into a cohesive form suitable for swallowing [1-3]. The urge to swallow can be triggered by a threshold level in both food particle size and lubrication of the food bolus [2, 4]. Masticatory performance, defined as the particle size distribution after a given number of chewing cycles, depends on dental state and body size of individual [5, 6]. Beside individual influence, differences in food texture have a

major influence on the masticatory performance and swallowing [7-12]. Recently, we have confirmed this statement by studying human mastication of two different corn flakes (Yven et al., 2010). It is not usual to find studies giving a complete cover of the human mastication. Some of them look at the food breakdown from the sensory perception viewpoint, focusing on a single type of food like the study of Lenfant et al. (2009) on wheat flakes chewing. Besides, many other works neglect food texture aspects and focus on oral phenomena such as chewing kinematics [13, 14], jaw motion and robotics [15, 16], electromyography (EMG) analysis [17, 18], food fragment models [4, 19, 20] and some combinations of these facets [21-24]. These works have a large interest, for surgery applications for instance, but also for the information they bring on the physiological parameters of mastication, but they do not take into account the complete mechanisms of food breakdown during mastication. Therefore, there is still a need to study the relations between the physiological variables and the breakdown of foods during mastication for the same type of foods, having different structural features, nevertheless.

In this context, the aim of this study is to ascertain the chewing behaviour of cereal brittle foods products, assessed by muscle activity, mandible motion and final particle size distribution. For this purpose, breakfast cereal foods with different texture, shape, structure and formulation are selected and tested by one individual. We use the same subject for all our experiments to get rid of human variability.

3. Material and methods

A volunteer man aged 28 years is enrolled in this study. He has natural dentition at least up to the second molars without evident defect of dental structures, periodontal problems or severe malocclusion. The average daily flow of whole saliva varies in health between 1 and 1.5 L (Humphrey et al 2001). Five different types of test foods (commercial breakfast cereals) are used: Chocapic, **C,** Golden Grahams, **G** (Nestlé S.A., Vevey, Switzerland), Miel Pops, **M,** Kellogg's corn flake, **K** (Kellogg's Produits Alimen-taires, Rosny-sous-Bois, France) and one organic cornflake **B** (Cereco, Domagné, France). The physical characteristics of these products (e.g. density, water content, fat percentages and yield point) have been previously reported [25, 26]. Table 1 recalls here the basic composition of these products. Since sample weight would have a certain effect on oral results [27], the volunteer is asked to chew the same 2 g of each product (Figure 1) in his usual manner until the swallowing point. Samples are served in a random order. The subject freely rinses his mouth with water before each

experiment. The recording session includes instruction, electrode setting, few practice trials and then randomized trials for the five selected products. All experiments are repeated three times. A short rest is imposed between each recording, to avoid muscular fatigue. Food boluses are analysed and food fragment distributions are determined using a 2D image analysis protocol described in details in [28]. This protocol is more accurate than sieving methods that are popular for extracting particle size distribution [20, 29].

Table 1: Composition of the samples as provided by commercial data.

Sample code	**Commercial name**	**Composition (g/100g)**		
		Lipids	Starch	Sugars
C	Chocapic	8.28	46.73	44.99
M	Miel Pops	1.13	61.8	37.07
G	Golden Grahams	3.75	60.22	36.03
K	CornflakesKellogg's	1.06	89.52	9.42
B	Cornflakes Bio	1.14	93.8	5.06

The mandibular movement is recorded for each experiment using a certus motion capture system from Northern Digital inc (Optotrak Model K-6, Myotronics Inc., Seattle,USA). Three high speed infrared markers (M1, M2, M3) are positioned on the individual face as shown in Figure 2. One marker is dedicated to swallowing point detection (M3). The second marker (M2) captures the lower mandible movement whereas the third marker provides the reference point. This configuration allows us to study all characteristics of the mandible motion such as opening, closing, inclination (α) and shearing (θ) with contrast to other solutions that give only vertical movement [9]. The system operates with a resolution of 0.01 mm. The marker acquisition frequency is adjusted to 100 Hz. Prior positioning, the skin areas, where the electrodes are to be placed, are cleaned with alcohol to reduce the impedance and enhance signal conductivity. The electrodes are attached with adhesive strips and are firmly pressed in place. The subject is sitting straight on an ordinary upright chair without head support. The Optotrak detector performs a triangulation calculation to determine the location of each marker. Post-treatment of the signals includes the determination of mandible displacement and velocity in the frontal plane (Figure 2). Further processing is performed using ImageJ, a software from the public domain. Mandible displacement loops are approximated as elliptical shapes and related quantities are computed such as area (a), orientation (α), minor (dx) and major (dy) axis lengths. Electromyography (EMG) activity is recorded in a similar way to a previously published work [28]. The activities of masseter and temporalis muscles are recorded and EMG signals are filtered and amplified. Chewing time (t), number of bursts

(N), swallowing time (T), mean (fm) and maximum (fx) voltage of bursts, cycle muscle work (w) are the main variables collected from each EMG sequence. All these variables, except for the swallowing time, are expressed as function of chewing cycles. Each of them is an average quantity of three replicates.

Figure 1. *Breakfast Cereals used in this study and related boluses.*

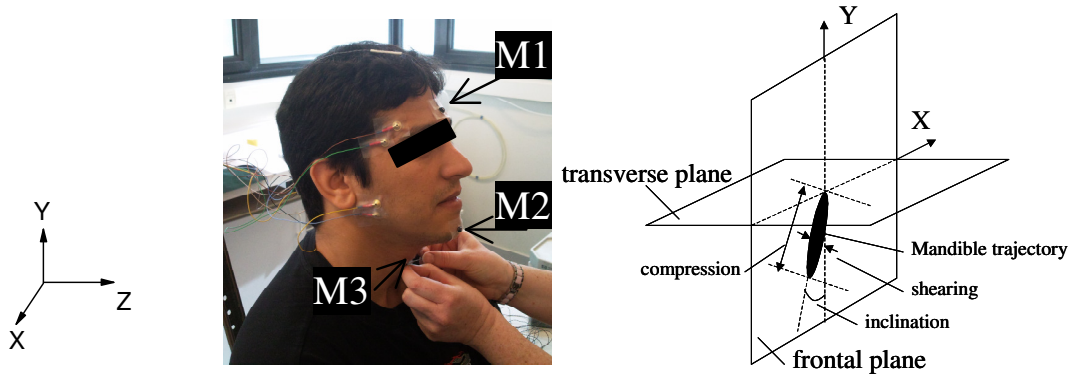

Figure 2. *The measurement setup for the simultaneous acquisition of mandibular movement and muscle activities using EMG.*

4. Results and discussion

4.1. Jaw movement analysis

Figure 3a presents typical mastication patterns of the studied products. Here, the patterns are shifted in x-direction to allow qualitative comparison. We recognise the main stages including

occlusion, opening and closing [15]. Despite apparent similarity, quantitative difference between the chewing trajectories is found. The area of the mandible displacement associated to each stroke can be used as a discriminating factor (Figure 3b).

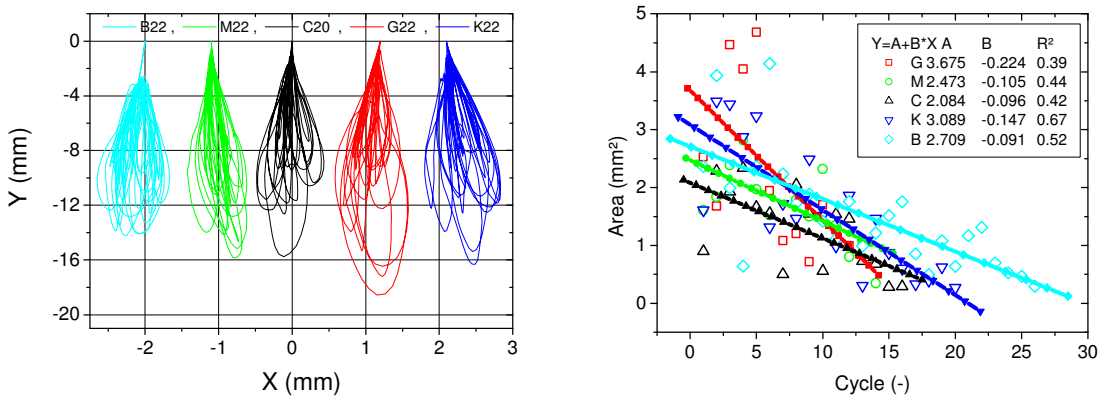

(a) (b)

Figure 3. *(a) Typical masticatory patterns of the studied products. (b) Areas of mandible trajectories as function of chewing cycles for all studied products. Each circle represents the average of three measurements.*

The overall decreasing trend of displacement area with cycle number well confirms that the largest cycle represents the signature of the first bite, whereas the area of subsequent cycles is smaller as a consequence of fragment size reduction. We notice, however, a scattering of area values according to the decreasing trend as a function of chewing cycles. Indeed, linear correlation between area and the cycle number is not satisfactory since the correlation factor (R^2), ranges from 0.39 up to 0.67. The analysis of the area (in mm^2) associated to the mandible displacement of the three first cycles shows the following ranking: G (2.89±1.43); K(2.85±1.07); M (1.95±0.40); B(2.76±1.03); C(1.70±0.72). When compared to the last three final cycles, the ranking changes to the following: G (1.11±0.14); M (0.75±0.38); K(0.43±0.18); B(0.43±0.12); C(0.42±0.23) mm^2. A minor change in ranking of the mandible displacement is noticed despite the large number of cycles that separate the first and final stages. In the average, the area changes from 2.43 mm^2 down to 0.63 mm^2, irrespective of the product type and chewing cycles. The reduction in area by a factor larger than 3 may be explained simply by the reduction in size of the food piece. The first ranking depends on the initial strike and, in turn, on the geometry of the food piece. Surprisingly, the same ranking holds before swallowing suggesting that the effect of food product still influences the mandible trajectory.

Displacement according to y (compression) may be associated to vertical movement because the values of angle α, or mandible inclination (Figure.4a), were found very low (1-3°) and do not vary neither with chewing cycle nor with product type.

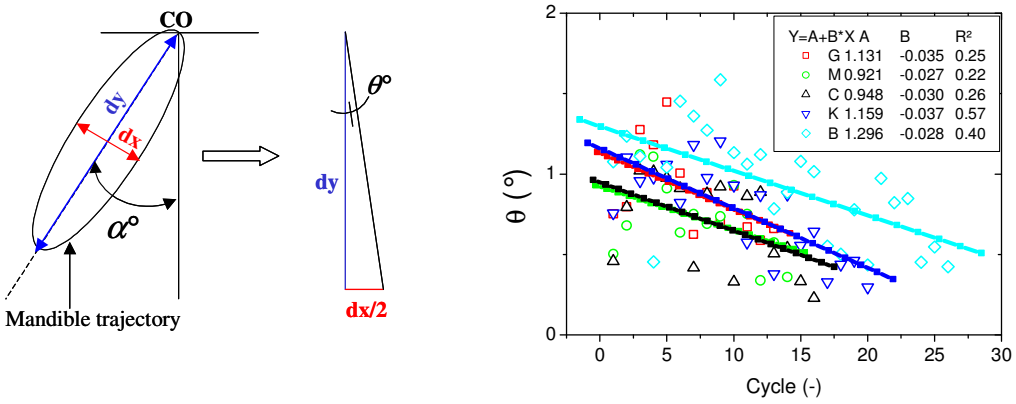

(a) (b)

Figure 4. *(a) Approximation of mandible displacement trajectory as an ellipse and illustration of the inclination (α) and shearing angle (θ). (b) Evolution of the shearing angle as function of chewing cycles for all studied products. Each circle represents the average of three measurements.*

Shearing effect can be approached by computing a shearing angle (Figure 4a):

$$\theta = \arctan\left(dx/2dy\right) \qquad (1)$$

where dy is the maximum opening corresponding to the major axis length. dx is the length of the minor axis, related to the transverse displacement.

Figure 4b depicts the evolutions of shearing angle as function of chewing cycles for all studied products. Linear correlation fails in describing the observed tendencies (i.e., $R^2 < 0.41$ in most cases). If shearing angle is averaged over all cycles together with repetitions, we obtain a small range of variation, 0.69 - 0.92 degrees with regards to the product type. The standard deviation, in the range (31 - 40)%, reflects large variation during chewing. For a typical vertical displacement (dy) of the mandible reaching 11 mm, its lateral movement (dx/2) is lower than 0.27 mm. The observed deviations show that there is no significant dependence of shearing on the mechanical properties of these products. This is confirmed by the correlation between shearing and compression displacements ($R^2 > 0.63$, except for product M), suggesting that dx/dy ratio is almost constant during chewing and does not vary much from one product to another (Figure 5).

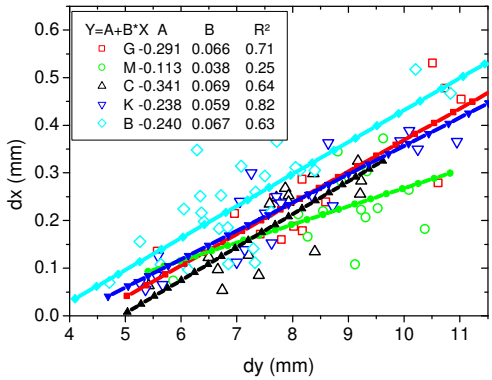

Figure 5. *Correlation between the vertical and lateral movements of the mandible.*

Moreover, the area (a) associated to the mandible trajectory is positively related to dx and dy for all products with a good correlation factor. The area (a) is also linearly related to the shearing angle (R>0.78). (Schindler et al 1998) estimated the maximum kinematic values of vertical movements were between 16 and 20 mm. These values decreased continuously in correlation to the number of chewing strokes and remained constant between 12 and 16 mm.

This result shows that the brittle character of the studied products does not require significant shearing during mastication, when compressive forces are sufficient to guarantee material failure.

Figure 6 shows the evolution of the bite rate in the frontal plane (X-Y). The bite rate increases up to its maximum value at the maximum opening and decreases down to 0 at the closing stage. There is no clear influence of the food item on displacement rate. The shape of the food item does not influence these kinematics since sample M, the spherical one, does not have a distinct behaviour. The largest velocities are around 220 $mm.s^{-1}$, irrespective of the food item whereas the average velocity computed over all cycles is close to 90 $mm.s^{-1}$. It is also common to define the mean opening and closing velocities as additional parameters related to the kinematics of mastication. ([30] estimated these characteristics as function of age and gender: opening and closing velocity ranges are (73 - 100) $mm.s^{-1}$ and (56 - 79) $mm.s^{-1}$, respectively. By separating the velocity loop into an ascending (i.e., opening) and a descending (closing) branches, we compute the mean velocities and obtain 122 $mm.s^{-1}$ and 72 $mm.s^{-1}$ for opening and closing, respectively, whatever is the product.

Finally, for these products, kinematics are very close and seem mainly governed by the brittle nature of the product which have similar mechanical properties as shown by their texture

assessment (Sandoval et al., 2008); the only significant difference comes from the opening displacement which is likely due to product dimensions.

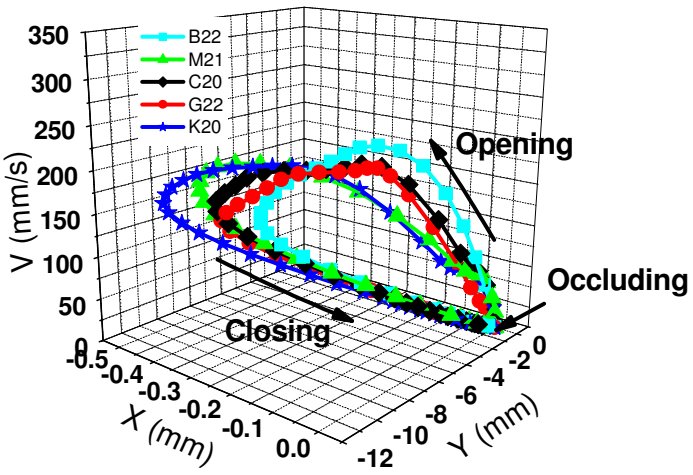

Figure 6. *Chewing rate evolution in the frontal plane.*

4.2. EMG analysis

Figure 7 presents EMG diagrams showing temporal and masseter muscle activities for the five cereal products. EMG charts do not display a higher masseter muscle activity (Figures 7a-7b) compared to temporalis muscles (Figures 7c-7d). Indeed, if we combine results related to maximum forces and sort them out taking as main criterion muscle activity, we end up with an average ratio between masseter and temporalis muscles close to 1.03. The same rationale leads, to a left muscle activity 1.96 times higher than that of right muscles, which reflects that the main characteristic of the subject is his ability to use more efficiently left muscles. Our results are in agreement with literature since differentiation between muscle activities is given less importance in oral studies, as scientists rather use the mean summed EMG activity [9, 27]. In some cases, chewing asymmetry is rather studied by weighting left and right side EMG activities [13, 31]. When specific stages of mastication sequence are of interest, differentiation may be important as temporalis muscles show better burst activity in closing compared to masseter muscles [7]. In the following, all extracted data (mean (fm) and maximum (fx) voltage of bursts, cycle muscle work (w)…) are averaged over masseter and temporalis muscles.

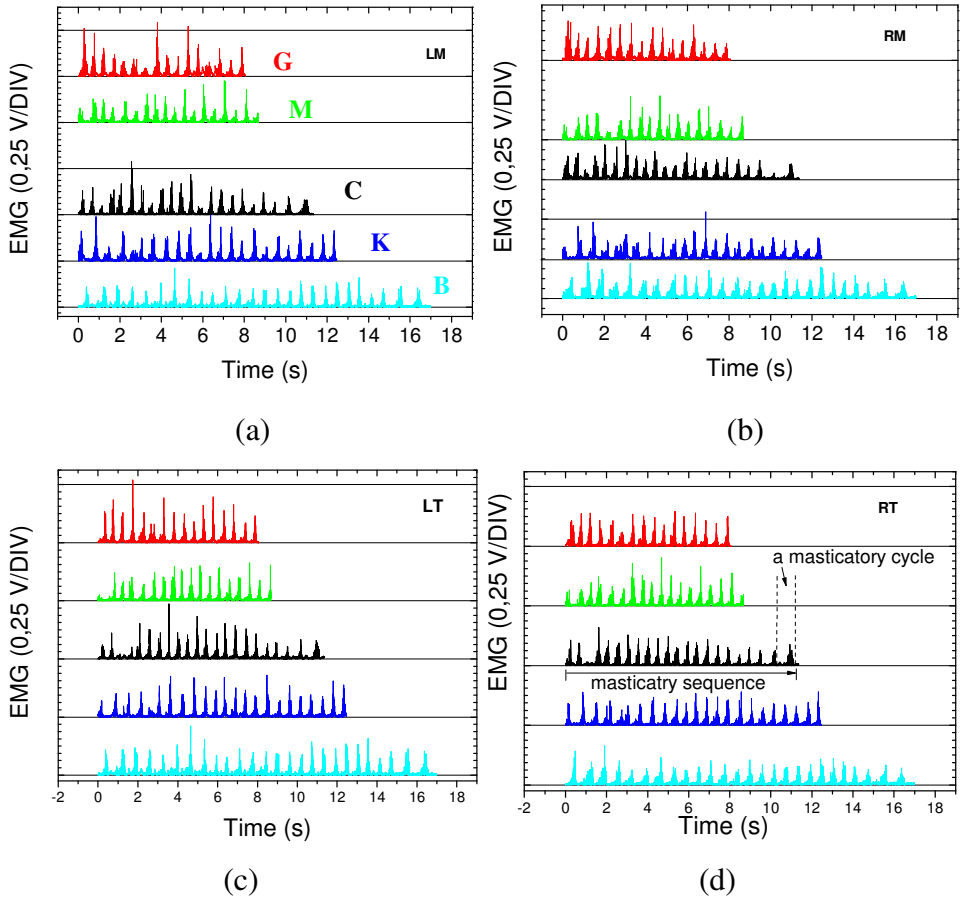

Figure 7. *(a) - (d) EMG Charts related to the mastication of the selected products (from bottom to top B, K, C, M, G). Here, L, R, M and T refer to left, right, masseter and temporalis, respectively.*

Depending on the products, results exhibit significant dispersion in the number of cycles (N = 16 to 26), sequence duration (T = 9 s to 18 s) and masticatory frequency (N/T = 1.12 s^{-1} to 2.00 s^{-1}). These values are close to the ones found by Kohyama et al. (2002) for young subjects eating crispy bread, a product which mechanical behaviour is similar to our cereal solid foams. This comparison also confirms that the selection of the subject in this study does not bring any bias for comparing the behaviour of our cereal products. Cereal products with lower number of cycles, and hence, shorter sequence, correspond to products (G, M, C), which have a high sugar content (Table 1). The burst number N is positively related to sequence duration T with an acceptable correlation factor (R=0.91, Figure 8). In addition, this Figure shows that the displacement dy is inversely correlated with the number of burst, confirming the decreasing trend precedingly remarked (Fig.3b).

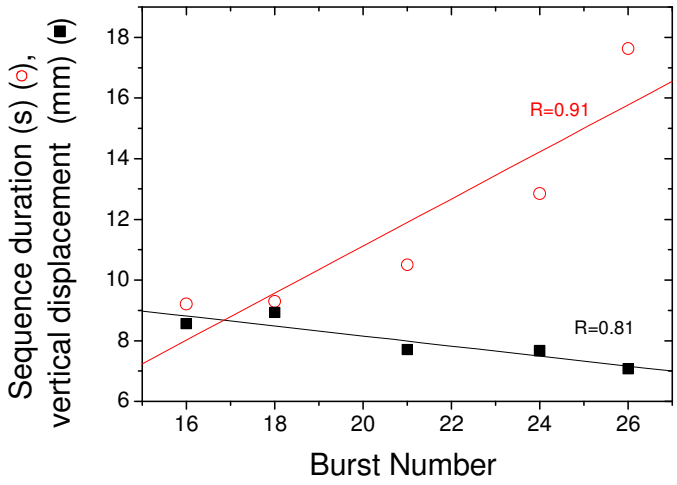

Figure 8. *Variation in the number of cycles (burst) sequence duration of chewing (○) and maximum opening of the jaw (■)*

Figure 9 details the evolution of EMG parameters as functions of chewing cycles for all products. Due to the large fluctuations associated to these results with regard to chewing cycles, a non-linear smoothing procedure is used based on exponential decay (or increase) functions in order to discriminate the products. Except one value for sample C, cycle duration for all products vary in a narrow range, between 0.48 and 0.6 s, overall (Figure 9a). These values were lower but close to those given by Peyron et al. (2002), i.e. 0.65s for model gels of gelatin, likely less stiff than dry cereal products. Their low variation with mastication time confirms that number of cycles and sequence duration are correlated ,as suggested before from Figure 7.

Figure 9b shows that the average chewing force fm decreases with chewing time in the range 0.31 - 0.45 mV for all products. Such a decrease is smaller in the case of product M (5%). Comparable tendencies are obtained for the maximum chewing force fx (Figure 9c) which evolves between 2.35 and 4.5 mV. Both tendencies, for average and maximum forces, are well observed in the literature for a wide range of food products [21, 32, 33]. In spite of similar decreasing trend, comparison between Figures 9b and c well show that products do not rank alike for average and maximum forces. Figure 9d shows that time evolution of the mastication work per cycle lies within the range (0.10 - 0.14) mV.s if we take as a basis the fitting curves. All samples exhibit a decrease of the mastication work by an amount of about 10%, except, again, sample M for which mastication work remains constant. The mastication

work is correlated to the average force since products rank in the same way. These trends are in good agreement with different reported tendencies on the mastication work [8, 33].

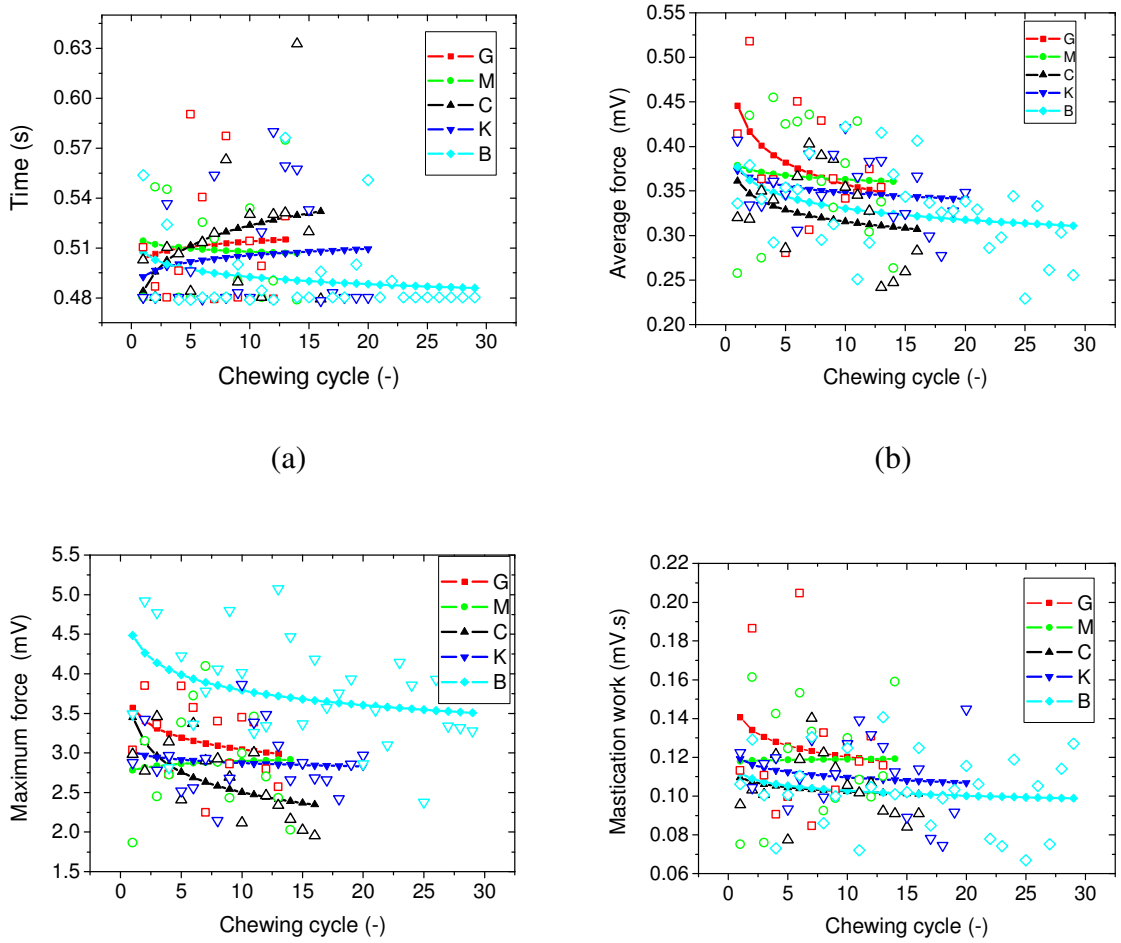

Figure 9. *EMG results for the studied products (a) average and (b) maximum forces, (c) mastication work and (d) burst duration.*

When comparing the present results for B and K to human mastication data reported by [28], qualitative agreement is obtained for average force and mastication work despite that results are related to different subjects. This result also confirms the influence on mastication behaviour of product inner structure, for same composition. Considering the shorter chewing sequence of product with higher sugar content, two interpretations may be suggested: first, the presence of sugar gives a more brittle product that is broken down faster and leading more rapidly to the necessary rheological state for bolus swallowing; secondly, the release of sugars acts as a stimulator for the chewing activity and salivation. In a recent study on cereal boluses,

[34] have shown that a constant final water content is reached at swallowing point. It indicates that saliva flow kinetics would be also involved in chewing sequence durations. In our opinion, saliva flow and food texture are dependent since a strong aptitude to fragmentation (i.e., brittleness) would favour the creation of large number of surfaces and allows better accessibility to saliva.

4.3. Distribution of chewed particles

Images of food blouses after chewing are shown in Figure 1. We observe a distinct cohesive agglomeration of the chewed particles for product M. After applying image analysis on the scanned boluses, particle area distributions are computed (Fig. 10). These distributions are given in a cumulative referential in order to better show the product effect. Each curve is an average of three replicates. The average scatter due to repeatability varies between 2% and 8% depending on the product. All curves exhibit the same shape, close to a truncated sigmoid function. The steepest area evolutions hold for the distributions containing the smallest fragments as for C, M in contrast with G, K, and mainly B. Spreading reflects a larger number of large particles, thus confirming the visual discrimination suggested in Figure 1. Although there is no straightforward relation between fragments size and the chewing duration, distributions containing smaller fragments are better associated to smaller chewing durations and vice-versa. We have fitted these curves using the Rosin-Rammler function to quantify main differences between products [28, 35]:

$$f(x) = 1 - 2^{-\left(x/xc\right)^{b}} \qquad (2)$$

where xc and b are fitting constants to be determined for each product.

In equation (2), the exponent b measures the steepness of the area distribution, whereas a the prefactor xc is the median area size of the distribution; a large value of xc shifts the whole distribution towards large area classes without changing the curve shape.

The exponent b varies between 0.8 and 1.1 whereas the range of variation for the prefactor xc is (0.05 - 0.22) mm². The fitting results are obtained with an excellent correlation factor R^2 (0.97 - 0.99). xc and b are not correlated mainly because product G has a large exponent and a large prefactor, which again underlines the importance of inner structural parameters.

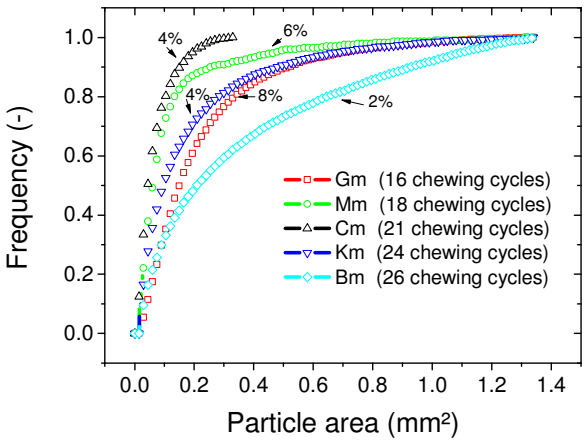

Figure 10. *Cumulative plots of the average area distributions of chewed particles for the selected products. Also are indicated the total bursts required for swallowing and the deviation due to repeatability.*

Compared to product K, which has a smaller prefactor, product B exhibits a more spread distribution, which is confirmatory of the result obtained by [28], for another subject. Figure 11 shows the relationship between xc and fx confirming the importance of the first bite for the fragmentation of the food (Dan and Kohyama, 2007), since maximal forces are obtained during the first cycles; this result shows that this step governs fragmentation and in turn, the final particle size, whatever the process re-agglomeration may occur to form the bowl before swallowing.

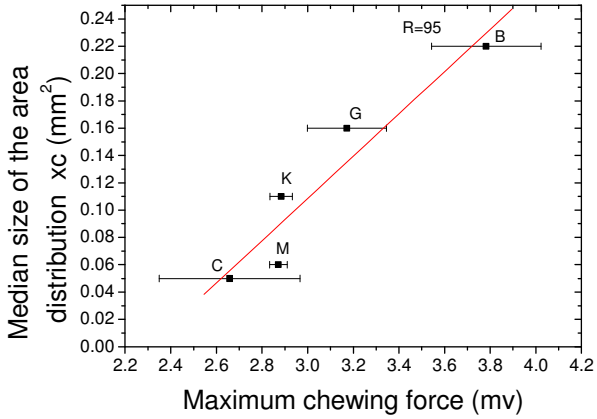

Figure 11. *Variation in xc of cerials before swallowing with maximum chewing force by chewing cycle*

4.4. Discussion

Taking into account the similar behaviour of these britlle products during chewing, correlations between chewing variables and product characteristics may be sought.

Our strategy is based on plotting each variable as a function of all other variables by substituting the chewing time. This work is done for all products using linear fitting routines. When an acceptable correlation factor (R>0.5) is obtained, the correlation is validated. Table 2 summarises the main findings based on these simple relationships. Note that because xc and b are only available at the final chewing time, their effects are reported, separately, in Table 3. The area associated with mandible trajectory has no evident correlation with EMG parameters except for maximum force.

Table 2: Linear correlations between studied variables by substituting the chewing cycle between variables. Also are indicated the correlation factors (R) for B, K, C, M and G, respectively.

		kinematics					***EMG***			
		a	***dy***	***dx***	***α***	***θ***	***fm***	***fx***	***w***	***t***
Kinematics	***a***	+(1)	+(0.84)	+(0.96)	+(0)	+(0.78)	+(0.51)	+(0)	+(0)	+(0)
	dy		+(1)	+(0.73)	+(0)	+(0)	+(0.62)	+(0)	+(0.58)	+(0)
	dx			+(1)	+(0)	+(0)	+(0.62)	+(0)	+(0.58)	+(0)
	α				+(1)	+(0)	+(0)	+(0)	+(0)	+(0)
	θ					+(1)	+(0)	+(0)	+(0)	+(0)
EMG	***fm***						+(1)	+(0)	+(0.94)	+(0)
	fx							+(1)	+(0)	+(0)
	w								+(1)	+(0)
	t									+(1)

Table 3 details the average quantities observed for all products including data on fragment size. The results for a, dx, dy, α, θ, fx, fm, t, T and w are the averages over chewing cycles whereas xc and b are given for the final chewing cycles. The steepness of the fragment size distribution (b) is found to increase with the increase of area associated to the mandible displacement (R=0.99) if we exclude product C. The median of the fragment size distribution is positively related to dx with an acceptable correlation factor (R=0.61). xc is clearly positively correlated to the maximum force (R=0.95) and it is also dependent on the sequence duration T (R=0.71). This last result is qualitatively similar to a study performed by [36] where the authors reported a linear increase of chewing duration as a function of an increasing size of gelatin food bolus. It justifies the interest of a mechanical modeling approach of this phenomenon of fragmentation (Hedjazi et al., 2011)., for which the experimental results obtained her provide boundary conditions.

Table 3: Average values related to kinematics (a, dy, dx, α, θ) and EMG (fm, fx, t, w, T) results over chewing cycles compared to fragment size related parameters (xc, b).

Product	B	C	G	K	M
a (mm²)	1.484±0.966	1.269±0.704	2.106±1.395	1.543±1.065	1.684±0.660
dy (mm)	7.071±1.345	7.709±1.061	8.559±1.671	7.672±1.718	8.934±1.087
dx (mm)	0.235±0.114	0.193±0.092	0.274±0.131	0.218±0.113	0.227±0.083
α (°)	1.327±0.471	1.245±0.493	2.221±0.638	1.595±0.527	1.256±0.680
θ(°)	0.923±0.334	0.692±0.279	0.884±0.272	0.769±0.290	0.720±0.240
fm (mV)	0.330±0.016	0.323±0.015	0.378±0.029	0.350±0.009	0.366±0.005
fx (mV)	3.783±0.240	2.658±0.309	3.172±0.173	2.884±0.050	2.872±0.039
t (s)	0.494±0.027	0.517±0.039	0.513±0.037	0.505±0.035	0.507±0.032
T(s)	17.63±0.77	10.50±0.78	9.21±1.02	12.85±0.34	9.30±0.87
W (mV.s)	0.103±0.003	0.104±0.002	0.125±0.007	0.110±0.003	0.119±0.000
xc (mm²)	0.220±0.004	0.050±0.002	0.160±0.013	0.110±0.004	0.060±0.004
b (-)	0.800±0.016	1.100±0.044	1.060±0.085	0.840±0.034	0.880±0.053

5. Conclusions

From this study the following conclusions are drawn:

- the jaw movement related to the mastication of brittle airy cereals show significant differences with regard to the selected products. However, the shearing angle averaged over all replicates does not show any clear correlation with regards to the selected products. Our results confirm that shearing is not involved in the mastication of brittle cereal foods even at final chewing stages.

- the duration of chewing sequence dis correlated to the number of bursts. EMGs also highlight that maximum and average forces are independent variables but they give different rankings with respect to the studied products. Because of the minor change in the cycle durations, the mastication work is found to be correlated to the average force.

- the final fragment size distributions of the studied cereal products are different. and depend on EMG results mainly reflected by maximum force.

Further analysis involving chewing cycles will be considered later by performing analysis of chewed boluses at different chewing times. At a longer term, these results provide a useful experimental data basis to feed modelling approach of solid foods chewing.

6. References

[1] Hutchings JB, Lillford PJ. The perception of food texture - the philosophy of the breakdown path. Journal of Texture Studies. 1988;19(2):103-115.

[2] Prinz JF, Lucas PW. Swallow thresholds in human mastication. Archives of Oral Biology. 1995;40(5):401-403.

[3] Shi CS, Ouyang G, Guo TW. Masticatory efficiency determined with direct measurement of food particles masticated by subjects with natural dentitions. Journal of Prosthetic Dentistry. 1990;64(6):723-726.

[4] Prinz JF, Lucas PW. An optimization model for mastication and swallowing in mammals. Proceedings of the Royal Society of London Series B-Biological Sciences. 1997;264(1389):1715-1721.

[5] Fontijn-Tekamp FA, van der Bilt A, Abbink JH, Bosman F. Swallowing threshold and masticatory performance in dentate adults. Physiology & Behavior. 2004;83(3):431-436.

[6] Engelen L, Fontijn-Tekamp A, Bilt Avd. The influence of product and oral characteristics on swallowing. Archives of Oral Biology. 2005;50(8):739-746.

[7] Agrawal KR, Lucas PW, Bruce IC, Prinz JF. Food properties that influence neuromuscular activity during human mastication. Journal of Dental Research. 1998;77(11):1931-1938.

[8] Peyron MA, Lassauzay C, Woda A. Effects of increased hardness on jaw movement and muscle activity during chewing of visco-elastic model foods. Experimental Brain Research. 2002;142(1):41-51.

[9] Peyron MA, Blanc O, Lund JP, Woda A. Influence of age on adaptability of human mastication. Journal of Neurophysiology. 2004;92(2):773-779.

[10] Marie AP, Olivier B, James PL, Alain W. Influence of Age on Adaptability of Human Mastication. J Neurophysiol. 2004;773-779.

[11] Lenfant F, Loret C, Pineau N, Hartmann C, Martin N. Perception of oral food breakdown. The concept of sensory trajectory. Appetite. 2009;52(3):659-667.

[12] Peyron MA, Mishellany A, Woda A. Particle size distribution of food boluses after mastication of six natural foods. Journal of Dental Research. 2004;83(7):578-582.

[13] Nishigawa K, Nakano M, Bando E. Study of jaw movement and masticatory muscle activity during unilateral chewing with and without balancing side molar contacts. J Oral Rehabil. 1997;691-696.

[14] Buschang PH, Hayasaki H, Throckmorton GS. Quantification of human chewing-cycle kinematics. Archives of Oral Biology. 2000;45(6):461-474.

[15] Xu WL, Bronlund JE, Potgieter J, Foster KD, Röhrle O, Pullan AJ, Kieser JA. Review of the human masticatory system and masticatory robotics. Mechanism and Machine Theory. 2008;43(11):1353-1375.

[16] Odake S, Van Ruth, S. M., Roozen, J. P., Miura, T., & Akuzawa, R. Influence of mouth model masticatory force on the release of limonene from orange fruit glucomannan jelly. In: Blank I, Wüst M, Yeretzian C, editors. 12th Weurman Symposium Proceedings. Interlaken, Switzerland: Zürcher Hochschule für Angewandte; 2008. p. 608.

[17] Stohler CS. A comparative electromyographic and kinesiographic study of deliberate and habitual mastication in man. Archives of Oral Biology. 1986;31(10):669-678.

[18] Throckmorton GS, Teenier TJ, Ellis E. Reproducibility of mandibular motion and muscle-activity levels using a commercial computer-recording system. Journal of Prosthetic Dentistry. 1992;68(2):348-354.

[19] Baragar FA, van der Bilt A, van der Glas HW. An analytic probability density for particle size in human mastication. Journal of Theoretical Biology. 1996;181(2):169-178.

[20] Flynn CS, Foster KD, Bronlund JE, Lentle RG, Jones JR, Morgenstern MP. Identification of multiple compartments present during the mastication of solid food. Archives of Oral Biology. 2011;56(4):345-352.

[21] Schindler HJ, Stengel E, Spiess WEL. Feedback control during mastication of solid food textures--a clinical-experimental study. The Journal of Prosthetic Dentistry. 1998;80(3):330-336.

[22] Lucas PW, Ow RKK, Ritchie GM, Chew CL, Keng SB. Relationship between jaw movement and food breakdown in human mastication. J Dent Res. 1986:400-404.

[23] Youssef RE, Throckmorton GS, Ellis E, Sinn DP. Comparison of habitual masticatory cycles and muscle activity before and after orthognathic surgery. Journal of Oral and Maxillofacial Surgery. 1997;55(7):699-707.

[24] Lin K-R, Chang C-H, Liu T-H, Lin S-W, Lin C-H. Experimental and numerical estimations into the force distribution on an occlusal surface utilizing a flexible force sensor array. Journal of Biomechanics. in press;44(10):1879-1884.

[25] Chaunier L, Courcoux P, Della Valle G, Lourdin D. Physical and sensory evaluation of cornflakes crispness. Journal of Texture Studies. 2005;36(1):93-118.

[26] Sandoval AJ, Chaunier L, Courcoux P, Della Valle G. Bulk mechanical behavior of commercial particle food foams. Journal of Texture Studies. 2008;39(4):405-425.

[27] Kohyama K, Yamaguchi M, Kobori C, Nakayama Y. Mastication effort estimated by electromyography for cooked rice of differing water content Bioscience Biotechnology and Biochemistry. 2005;69(9):1669-1676.

[28] Yven C, Guessasma S, Chaunier L, Della Valle G, Salles C. The role of mechanical properties of brittle airy foods on the masticatory performance J Food Eng. 2010;101(1):85-91.

[29] Mishellany-Dutour A, Peyron M-A, Croze J, François O, Hartmann C, Alric M, Woda A. Comparison of food boluses prepared in vivo and by the AM2 mastication simulator. Food Quality and Preference. 2011;22(4):326-331.

[30] Kiliaridis S, Karlsson S, Kjellberg H. Characteristics of Masticatory Mandibular Movements and Velocity in Growing Individuals and Young Adults. J Dent Res. 1991;1367-1370.

[31] Di Palma E, Gasparini G, Pelo S, Tartaglia GM, Chimenti C. Activities of masticatory muscles in patients after orthognathic surgery. Journal of Cranio-Maxillofacial Surgery. 2009;37(7):417-420.

[32] Gibbs CH, Mahan PE, Lundeen HC, Brehnan K, Walsh EK, Sinkewiz SL, Ginsberg SB. Occlusal forces during chewing--Influences of biting strength and food consistency. The Journal of Prosthetic Dentistry. 1981;46(5):561-567.

[33] Tarrega A, Yven C, Sémon E, Salles C. In-mouth aroma compound release during cheese consumption: Relationship with food bolus formation. International Dairy Journal. 2011;21(5):358-364.

[34] Loret C, Walter M, Pineau N, Peyron MA, Hartmann C, Martin N. Physical and related sensory properties of a swallowable bolus. Physiology & Behavior. in press;In Press, Corrected Proof.

[35] Julien KC, Buschang PH, Throckmorton GS, Dechow PC. Normal masticatory performance in young adults and children. Archives of Oral Biology. 1996;41(1):69-75.

[36] Daet DG, Watanabe M, Sasaki K. Association between the interarch distance and food bolus size in the early phase of mastication. The Journal of Prosthetic Dentistry. 1995;74(4):367-372.

Partie 2

Simulation réaliste par la méthode des éléments finis de la répartition entre deux dents d'un aliment céréalier de structure alvéolaire l

Article.4

Realistic simulation of cereal food breakdown using finite element method

Written for presentation at the 2011 CIGR Section VI International Symposium on "Towards a Sustainable Food Chain Food Process, Bioprocessing and Food Quality Management" Nantes, France - April 18-20, 2011

Realistic simulation of cereal food breakdown using finite element method

Lotfi Hedjazi[1], Sofiane Guessasma[1*], Cyrus Abbasi[2], Guy Della Valle[1], Tariq A. Khraishi[2]

[1]INRA, UR1268 Biopolymères, Interactions & Assemblages (BIA), 44316 Nantes, France

[2]Mechanical Engineering Department, University of New Mexico

Albuquerque, NM 87131, USA

1. Abstract

Human mastication is a complex oral process that leads to food breakdown. The understanding of the mechanics of mastication requires the knowledge of food item properties and geometry, chewing force amplitude and frequency, mandibular trajectory as well as a precise information about food-teeth contact. In this work, all these oral aspects are handled numerically using a finite element model. Firstly, experimental procedures are used to determine molar geometry and cellular structure of two breakfast cereals. Secondly, a Finite Element (FE) model is developed accounting for the exact geometry of both food items and teeth to simulate food breakdown. The loading conditions including normal and sliding motions of the teeth system are reproduced for each product. Teeth-food item contact is optimized to avoid significant material overlapping. The model is able, at least for the first bites, to determine strain and stress distributions that develop upon mastication loading. It also highlights the shearing effect associated to food compression during mastication. Simple considerations about failure strain of the solid material allow the conversion of the strain distributions to food fragments. The major finding is that fragmentation occurs earlier before complete occlusion and tends to produce a large number of fragments.

Keywords: Cereal food product, Mastication, Finite Element Method, mandible displacement.

2. Introduction

The main function of mastication is reducing the size of the food item to ease swallowing and contributes to food chemical and physical degradation (Lucas, Prinz, Agrawal & Bruce, 2002). The complex nature of the forces involved during mastication and food complexity makes it difficult to follow experimentally the stress and strain states that develop in the food

item during mastication stage. These states would be very informative about sequencing of rupture events and in turn, the formation of the food bolus (Yven, Guessasma, Chaunier, Della Valle & Salles, 2010). Our interest on cereals goes from that side of considering this food as a major ingredient in our processed food. And for some individuals, it is difficult to maintain regular consumption of cereals because of age, dental problems and/or inadequate formulations. It is thus an exciting challenge to be able to adjust the formulation and design process of transformed products to match some mastication criteria. But, before addressing this challenge, one has to know how the structure and texture of the food item affect the human mastication. In such a way, this work is a first attempt to consider realistic simulation of food degradation using finite element computation. Our approach is rendered realistic as much as possible by sticking to relevant experimental data. The ideas detailed in this work focus on the implementation of the mechanical model, typically on how oral parameters are handled. The paper also underlines the effects of product structure involved during the simulation of human mastication.

3. Finite element simulation

3.1. Teeth geometry

The geometry of a volunteer's oral cavity is acquired using dental molding (Figure 1). The plaster moulds of maxilla and mandible are then scanned using 3D laser probe. The point density reaches typical values of 100 points.mm^{-2}.

(a) (b)

Figure 1. *Mandible and maxilla surface geometries from plaster moulds (a) and acquired using laser scanning (b).*

The cloud point is converted into a triangular irregular meshing using plane element (Figure 2). Each element is described by two nodes capable of displacements in the relative X-Y plane. In order to allow 3D displacement of the mandible, surface meshes are extruded into volume meshing using prism elements in Z direction. Further processing includes mesh cropping on the molars and molar distance adjustment depending on the food item.

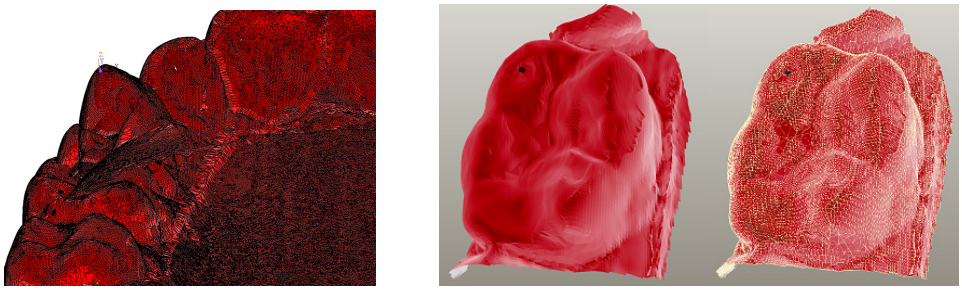

(a) (b)

Figure 2. *(a) Rough view of surface meshing, (b) zoomed views on surface topography and meshing of one molar.*

3.2. Food product cellular structure

Two commercial breakfast cereal foods, Miel Pops (M) and Golden Grahams (G), are selected as a case study (Figure 3). These are characterized by different geometry and texture. Table 1 shows the composition and fracture energy data from (Sandoval, Chaunier, Courcoux & Della Valle, 2008). Note that failure energy is derived from Kramer cell experiments as detailed in the same work.

Table 1: Main components and failure energy data of the studied products.

	moisture (wet basis)	sugars (g/100g)	starch (g/100g)	failure energy (J)
M	3.6	33.0	55.0	13.2
G	3.7	31.8	49.2	15.1

The cellular structure of the food item is determined using a synchrotron radiation at the ID19 beamline from ESRF facility (F38-Grenoble) using a two-dimensional detector as well as a CCD camera for computerized X-ray micro-tomogaphy (XRT) experiments. The number of radiographic images needed for 3D feature reconstruction ranges from 1200 to 1500 depending on samples. The pixel size is fixed to 7.46 µm but the whole acquisition of the samples requires several stacks to be built and gathered.

The process leads to crop volumes in the range 4.2 - 8.6x10^9 voxels. Separation between the solid and the voids is clearly established thanks to the good contrast. Thresholding operator is then performed to process towards binary images. Because of computation resources limitation, the full resolution of the images could not be used for finite element computation.

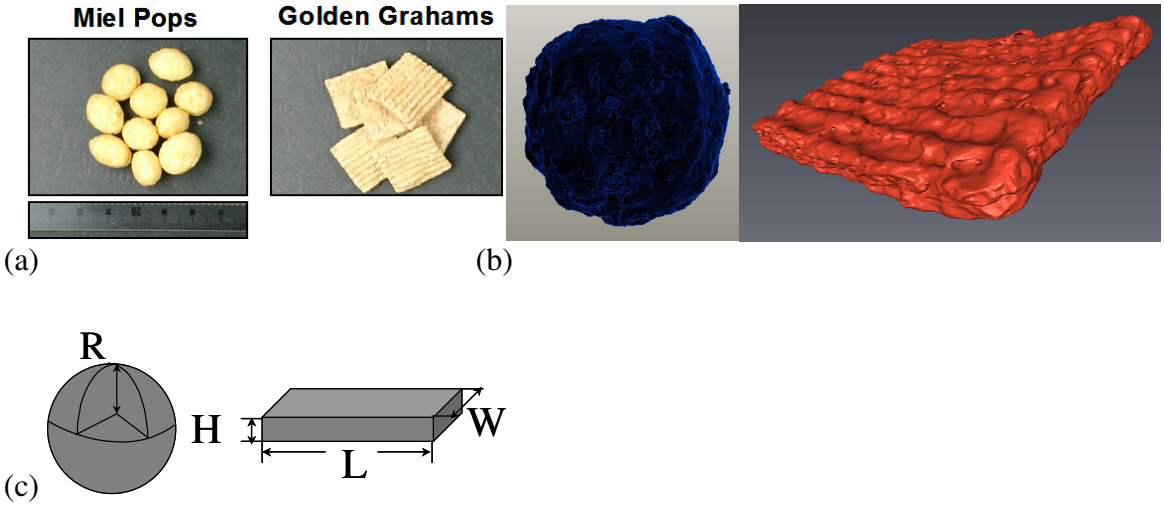

Figure 3. *(a) Selected breakfast cereals M and G. (b) Perspective views of the products as acquired using XRT and (c) approximated shapes (in mm): R=6, L=19. 7, W=17, H=2.8.*

Sub-resolutions are then recomputed and the subsequent effect on the cellular structure is evaluated. Cell size and wall cell size distributions are determined using granulometry technique. Octahedral structuring element is grown numerically and the scores for each size class is saved. In addition to size distributions, the relative density of each sample is computed. This quantity expresses the density for the cellular material over that of the solid phase. Such definition scales naturally the relative density between 0 and 1. If we consider the density of the solid phase as the measurement unit, it turns out that relative density ρ writes

$$\rho = \sum_{i=1}^{V} \delta_i / V \quad \left| \delta_i = 1 \right. \left| \; ni = 255 \; ; \quad \delta_i = 0 \right| ni = 0 \qquad \text{and} \qquad \text{Porosity} = 1 - \rho \qquad (1)$$

where V is the volume of the cellular material as a voxel count. δ is a threshold function of the gray level ni of the image coded in 8 bits.

In order to compute the relative density, we have to provide, in equation (1), an evaluation of the cellular volume which is clearly lower than the crop volume. For that reason, a contour of the cellular material has to be found. Different approaches can be attempted among which the fill hole approach, the manual boundary detection and the wrap technique. This last method is attempted because the first fails in detecting open void structure and the second is too time consuming. The basic lines of wrap technique is to roll a hard sphere of radius r=10 voxels along the solid phase starting the sphere displacement from the boundaries of the crop volume.

Meshing of the food item is irregular using tetrahedral elements, where each element is described by four nodes. Three degrees of freedom are associated to each node corresponding

to 3D structural displacements. Irregular meshing allows, in our situation, a substantial node saving because the element size is adjusted depending on the local solid curvature. Despite that saving, the solid still needs 127000 elements to be meshed.

3.3. Setting food pieces in contact between teeth

Contact between meshed items is performed by creating contact elements on the deformable body and target elements on the sliding rigid teeth. The point-to-point contact is managed using the penalty method where normal and tangential stiffness are implemented when surface overlap is detected. Figure 4 shows the geometry and meshing of the whole system. The whole model stands with less than 38 000 elements for each tooth added to about 26 000 contact and target elements.

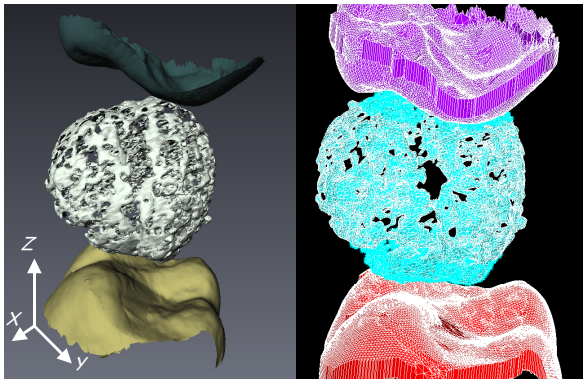

Figure 4. *Geometry and of the teeth-food system.*

Virtual human mastication with two molars and a food piece requires thus less than 2.10^5 elements. In addition to meshing, isotropic elastic properties for both teeth and food item are implemented. The solid phase of the food item is described by the following properties: Es=0.231 GPa, vs=0.30, where E and ν refer to Young's modulus and Poisson coefficient, respectively, index s indicating “solid phase”. In order to avoid stress to develop in teeth (index t), the following material properties ratios are used: Et/Es>>10 and νt/νs =0.23 which fall in the same orders of magnitude as the known material properties for dentine (≈30GPa) and enamel (≈160GPa). Boundary conditions require rigid displacement of the lower tooth (normal in Z direction and transverse in X direction). A shearing angle is defined as follows:

$$\theta = \left| UX/UZ \right| \qquad (2)$$

Where UX and UZ are structural displacements imposed to all nodes of the lower tooth.

In addition, all degrees of freedom are fixed for the upper tooth. Constraints against displacements in X and Y directions are imposed for three particular nodes belonging to the food item to avoid rigid body motion and rotation.

4. Results and discussion

Figure 5 shows that the wrap technique is relevant to determine the contour of the studied samples and, in turn, the relative density. The void contents, as computed using equation 1, are 46% and 74% for G and M, respectively.

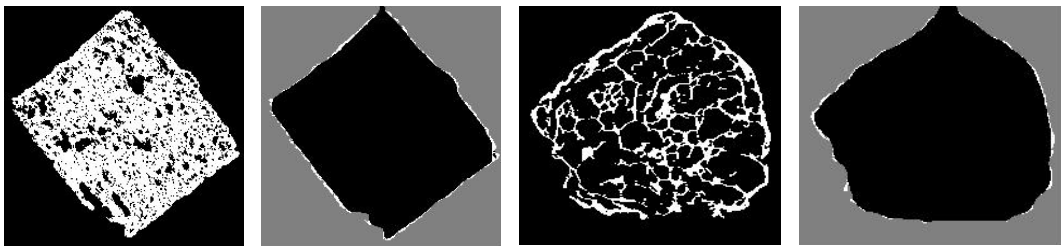

(a) (b) (c) (d)

Figure 5. *Cross-sections of (a) G and (c) M foods, and related (b)-(d) closed contours using wrap technique, respectively.*

The effect of resolution roughening is studied through the pore (void) and solid phase (wall) size distributions. Table 2 summarizes the numerical results for three subresolutions A, B and C, where the pixel size d is d_A=2 x d_B = 8 x d_C = 16 d_D, and d_D=7.46 µm is the original pixel size. Distributions are processed in a cumulative referential, where the scores of all preceding size classes to a given class are summed. Thus, the highest size class contains the whole distribution count. All classes are then scaled with regards to the total score. Our results indicate that size distributions are similar in shape regardless the resolution. However, these are lower bounded differently. The finest resolution (C) intercepts thin walls as small as 15 µm instead of 60 µm for resolution (A). All distributions end up to about 970 µm which represents the largest pore size in the structure. The evaluation of the largest pore size is more precise with the fine resolution because of narrower size classes. We loose 8% and60% of small walls, for products M and G respectively, with resolution A, whereas such loss drops to less than 3% and 27%for resolution B. In a similar way, the study of resolution effect on cell wall size distributions reveals a lower size cut-off for resolution A. The effect on missing walls seems to be stronger in this case. For products M and G respectively, up to 47% and 55%(M) of small cell walls (< 45 µm(M), <134µm(G)) disappear for resolution A. Such percentage decreases to about 20% and23% for resolution B. Table 2 summarizes the statistics performed on both pores and walls distributions.

Figure 6a-b shows typical nodal solutions for a compression of about 1.6 mm without shearing effect. Despite local contact, strain is transmitted to the whole cellular structure, where strain localization appears not only near the contact region. Note that strain does not develop in teeth even near the contact regions. Z-displacement contours do not match the normal displacement imposed because rotation during compression is not forbidden. Further comment would necessarily introduce failure data about solid material. Comparing data from (Guessasma, Chaunier & Lourdin, 2010) where strain at failure for starch does not exceed 2%, and z-strain range between 6.7 and 8.5%, in Figure 6b indicates that solid failure has to occur during first stages of compression. Also, an increase of shearing angle modifies significantly the x-displacement distribution as shown in Figure 6c-e. The comparison between strain distributions (e_{33}) for both products, at the same compression level, indicates an upper strain level for at about 0.08 whereas for G, nodal strain is lower than 0.02.

Table 2: Numerical results compilation about the studied products.

	average void size(µm)			average solid size(µm)			relative density (B)
resolution	A	B	C	A	B	C	
Miel Pops (M)	219	267	304	89	80	77	0.26
Golden Graham (G)	198	209	272	301	182	161	0.54

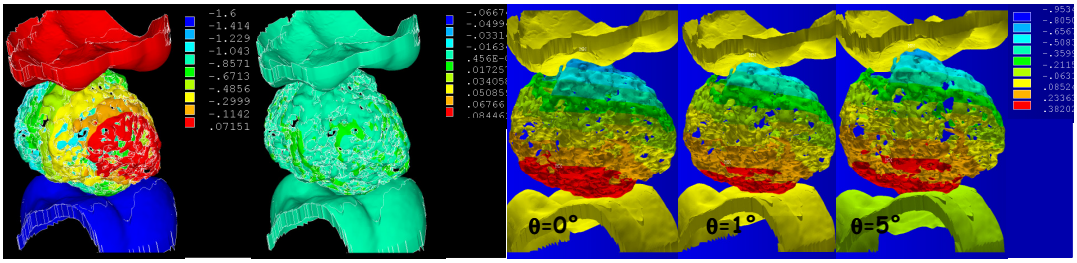

(a) (b) (c) (d) (e)

Figure 6. *Nodal solutions showing, (a) Z-displacement, (b) Z-strain, (c)-(e) X-displacement as function of shearing angle.*

Based on the former discussion, failure probability is significant in the case of M, which is confirmed by the lower fracture energy observed experimentally for this cereal food.

5. Conclusions

Our main finding is that fragmentation is likely to occur at first deformation stages before complete occlusion. Our computation also shows that, in spite of same intrinsic material properties, the two cereal foods display different strain distributions; this result particularly highlights the role of geometry and cellular structure in driving fragmentation process. Further

processing, in near future, is needed to convert strain solutions into fragments distribution. By doing so, it will be possible to compare experimental and numerical fragment size distributions at least for the first mastication cycles. Validation will also be attempted by comparing the numerical reaction forces to EMG profiles.

Acknowledgements

Authors are acknowledging Mrs Barbara Fayard (Novitom) and Anne-Laure Réguerre (INRA Nantes) for XRT imaging and analysis.

References

Guessasma, S., Chaunier, L., & Lourdin, D. Finite element modelling of the mechanical behaviour of vitreous starch/protein composite. *Journal of Food Engineering,* **98**(2): 150-158.

Lucas, P. W., Prinz, J. F., Agrawal, K. R., & Bruce, I. C. (2002). Food physics and oral physiology. *Food Quality and Preference,* **13**(4): 203-213.

Sandoval, A. J., Chaunier, L., Courcoux, P., & Della Valle, G. (2008). Bulk mechanical behavior of commercial particle food foams. *Journal of Texture Studies,* **39**(4): 405-425.

Yven, C., Guessasma, S., Chaunier, L., Della Valle, G., & Salles, C. (2010). The role of mechanical properties of brittle airy foods on the masticatory performance *Journal of Food Engineering,* **101**(1): 85-91.

Chapitre IV. Mécanismes de fragmentation

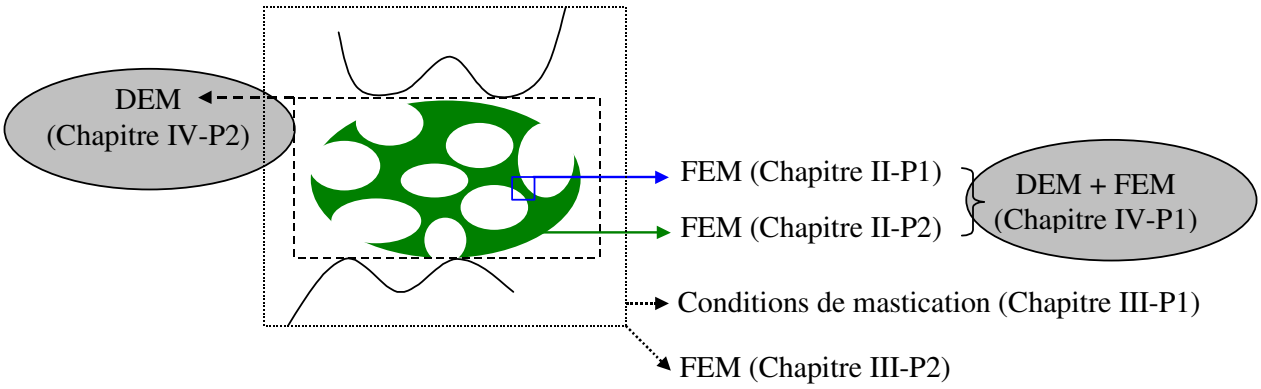

Etant donnée son importance dans la mastication d'aliments solides fragiles, il est nécessaire de pouvoir modéliser le phénomène de fragmentation, ce qui fait appel au développement de méthodes numériques. A cet effet, la méthode des éléments discrets (DEM), mise au point pour représenter le comportement mécanique de matériaux particulaires, semble bien convenir pour aborder certains aspects liés aux problèmes dynamiques rencontrés pour les matériaux fragiles étudiés ici. La raison de ce choix réside dans le fait que la méthode des éléments finis utilisée devient instable pour décrire un comportement on grandes déformations comme c'est le cas de la mastication humaine. Il convient donc, dans un premier temps, de l'adapter à la représentation du comportement interne de structures en amidon vitreux, dense, où la fissuration est l'une des principales causes de déformation et d'endommagement. Ensuite, la méthode pourra être appliquée à l'endommagement de structures alvéolaires, qui résulte d'un couplage entre l'écrasement des cellules et la propagation de fissures dans le matériau constitutif.

La propagation de fissures dans un amidon vitreux est étudiée numériquement, analytiquement et expérimentalement **dans une première partie**. Cette partie présente la DEM et plus particulièrement une méthode basée sur des éléments discrets sphériques. Des éprouvettes entaillées, et présentant de trous, sont testées en traction. Comme nous l'avons vu au Chapitre II, partie 1, la visualisation par caméra rapide révèle une déviation de la fissure et l'apparition de réseaux de fissures. Pour décrire la propagation locale en mode mixte, des simulations par éléments discrets et par éléments finis sont mises en œuvre et comparées. Les deux méthodes sont capables de prédire le chemin observé de la fissure, mais seule la DEM permet de prédire l'apparition du réseau de fissures avec un simple critère de contact entre particuls.

Dans une seconde partie, le modèle DEM a été étendu à des matériaux alvéolaires, dont la structure cellulaire, hétérogène conduit à une hétérogénéité des contraintes qui entraîne une localisation des champs. Le modèle DEM à été appliqué à un aliment céréale petit-déjeuner, dont la structure numérique 3D a été déterminée par micro tomographie aux rayons X (ESRF, Grenoble), afin de simuler numériquement la compression de l'aliment jusqu'à l'étape de densification. On montre comment la gestion du contact permet d'étudier des phénomènes complexes liés à la fragmentation. Dans tous les cas étudiés, les résultats sont en accord qualitatif avec ceux obtenus expérimentalement. Cette étude montre donc la capacité de la modélisation par éléments discrets à aborder des problèmes pour lesquels la mécanique des milieux continus est confrontée à des difficultés majeures. En dépit des coûts de la simulation

numérique, elle a aussi montré ses potentialités dans l'étude de la fragmentation des matériaux à microstructure complexe tels que les mousses solides, dont les céréales du petit-déjeuner constituent un bon exemple dans le domaine alimentaire.

Partie 1

Modélisation de la propagation de fissures dans un biopolymère vitreux par la méthode des éléments discrets

Article.5

Dynamics of material discontinuities revisited using discrete element method: application to crack propagation in a vitreous dense biopolymer material

Dynamics of material discontinuities revisited using discrete element method: application to crack propagation in a vitreous dense biopolymer material

L. Hedjazi[1,2*] , C. L.Martin[2], S. Guessasma[1] , G. Della Valle[1], R. Dendievel[2]

[1] INRA, UR1268 BIA, Rue de la Géraudière, Nantes 44316.

[2] Laboratoire SIMAP, Grenoble INP/UJF/CNRS, 101, rue de la physique, BP 46, 38402 Saint Martin d'Hères cedex

* Corresponding author

Phone. +33 (0)2 40 67 50 36, fax.+33(0)2 40 67 51 67

E-mail address: lotfi.hedjazi@nantes.inra.fr

1. Abstract

Crack propagation in a vitreous biopolymer material is studied using the Discrete Element Method (DEM). Our experiments combine a high-speed camera monitoring of crack branching together with a micromechanical testing of samples where local mixture mode is generated by introducing a stress concentrator. Our experimental results show unstable crack propagation and branching occurring upon crack deviation by the action of the stress concentrator. Numerical prediction of crack instabilities is performed using DEM. The validity of the DEM predictions is checked by comparing its results to the Finite Element Method (FEM) and an analytical expression under similar conditions. Our DEM results show a higher sensitivity to mixed mode compared to FEM and fall closer the analytical formulation. In addition, crack branching is well predicted using DEM with no specific criterion for the initiation of secondary cracks.

Keywords

Fracture mechanics; Biopolymer; Discrete element method; finite element analysis

2. Introduction

Fracture behaviour in brittle materials is one of the subjects which are of utmost interest in the research community in the recent years. Crack deviation under the action of a given loading is common in materials exhibiting a large material properties contrast such as in cellular materials [1]. Crack instabilities are also a matter of concern, especially crack branching,

which is not yet completely understood [2]. Extensive work has been published on the mechanisms leading to crack initiation and propagation in various brittle materials. Numerical methods can help in describing such mechanisms thanks to available computation resources and well elaborated models that are capable of handling local microstructural information [1, 3]. Brittle fracture, as an example, is proved to be sensitive to local heterogeneities that explain crack deviation and crack branching. These heterogeneities affect stress distribution and leads more or less to change in crack trajectory [1, 4].

In this paper, we use discrete element simulations to study crack propagation in a brittle biopolymer.

The Discrete Element Method (DEM) is a powerful numerical method proposed for predicting the behaviour of particulate media. It is a well popular and suitable approach to study the dynamics of granular geomaterials [5] and powders [6]. The main lines of the method consist in describing the material as an assembly of interacting grains. Grain motions obey Newton's second law where forces and displacements are updated at a suitable time increment [7]. The whole system evolves following a state path that enforces dynamics equilibrium on each particle. Boundary conditions can be implemented using rigid geometric objects such as cylinders, planes, spheres or periodic boundary conditions. The interactions between particles are described by adequate contact models, such as elastic force displacement laws or Coulomb friction (Figure 1b). Attractive forces such as van der Waals forces can be implemented, thus allowing the modelling of cohesive particulate systems [8]. Another important family of contact models includes those allowing particles bonding so that tensile forces and moments are transmitted through contacts [9-11].

In several applications, each modelled particle represents a physical entity, and the total system models a granular material. Another more recent application for DEM is the modelling of dense materials with bonded particles. In this case, each modelled particle does not represent a physical entity. Instead, it is the set of microproperties that is able to model the dense material. Interactions laws are implemented and adjusted to correctly represent the dense material behaviour [9, 12].This kind of approach is particularly suited to tackle fracture in dense materials [9]. In our paper, this method is adopted to model the fracture in a vitreous dense biopolymer material, chosen as model for cereal foods.

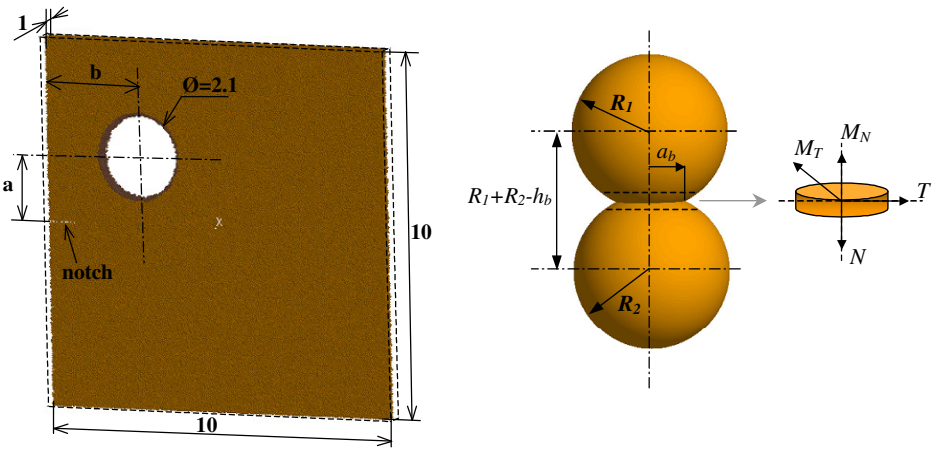

(a) (b)

Figure 1. *(a) Representation of random packing of spheres to simulate crack propagation in btittle starch using DEM. (b) Contact model assumed for the DEM.*

3. Model Description

3.1. Discrete element method

The dense material is represented by a packing of overlapping spherical particles nearly monosize. Particles are first packed together to obtain a dense particulate system with a 0.60 relative density. This packing is then further densified to obtain some overlapping between particles, using a sintering scheme described in [13]. At this stage, a relative density of 0.72 is reached. The sintering stage allows for a homogeneous but still random structure to be generated. At the end of this sintering stage, each particle has on average 7.23 contacts with neighbouring particles. All along the preparation stage, two planes orthogonal to direction z are used as boundary conditions, while periodic conditions are used in the lateral conditions.

Once generated, the dense sample is given microproperties between contacting particles which represent bonds. These microproperties consist of normal and tangential stiffness, resisting moments and strength parameters.

Denoting R_1 and R_2 the particle radii, the equivalent radius R^* is written as:

$$R^* = \frac{R_1 R_2}{R_1 + R_2} \qquad (1)$$

The bond radius is denoted as a_b, while the normalized bond radius, a^*, is defined as (Figure 1b):

$$a^* = \frac{a_b}{2R^*} \tag{2}$$

The normal and tangential components, N and T, of the bonding force between two spheres with equivalent radius R^* are:

$$N = \Sigma_N a^* R^* u_N \ , T = -\Sigma_T a^* R^* u_T \tag{3}$$

where u_N and u_T are the accumulated normal and tangential displacements integrated from the actual relative displacements of the two particles. Σ_N and Σ_T are material parameters with stress dimension.

Forces are taken positive in tension while the tangential force opposes the accumulated tangential displacement. The bonded contacts transmit resisting moments, M_N and M_T, in the normal and tangential directions:

$$M_N = -2\Sigma_T \left(a^* R^*\right)^3 \theta_N \ , M_T = -\Sigma_N \left(a^* R^*\right)^3 \theta_T \tag{4}$$

where θ_N and θ_T are the accumulated relative rotations in the normal and tangential directions (Figure 1b).

A fracture criterion is included in the microproperties of the bond. Approximating the solid bond by a cylindrical beam of radius a_b and using beam theory, the maximum tensile and shear stresses at the bond periphery may be evaluated as [9]:

$$\sigma_N = \frac{N}{4\pi\left(a^* R^*\right)^2} + \frac{|M_T|}{2\pi\left(a^* R^*\right)^3} \quad , \quad \sigma_T = \frac{|T|}{4\pi\left(a^* R^*\right)^2} + \frac{|M_N|}{2\pi\left(a^* R^*\right)^3} \tag{5}$$

Thus, bond fracture may occur due to tensile, shear or bending deformation of the beam. It is assumed that fracture occurs whenever $\sigma_N > \Sigma_c$ or $\sigma_T > \Sigma_c$, where Σ_c is a material parameter with stress dimensions that represents the strength of the solid bond.

Two particles may resume contact after the original bonded contact has failed. We assume that this occurs when the interparticle distance is the same as that when the solid bond failed (Figure 1b). When it resumes, the contact behaves with the same normal stiffness in compression as a bonded contact ($\Sigma_N a^* R^*$). Thus, whereas an unbroken bond behaves symmetrically in tension and compression, a broken solid bond behaves asymmetrically in tension (no force) and compression (same stiffness as an unbroken bonded contact). The tangential force for a broken bond follows the Hertz–Mindlin law where a Coulomb friction (friction coefficient μ) limits the norm of the tangential force during sliding. A broken bond transmits a resisting moment in the tangential direction but none in the normal direction. This broken bond model allows the existence of a previous bond to be taken into account in a

simplified manner. In any case, since we are interested in tensile tests, broken bonds seldom transmit compressive force. The boundary conditions used during the sample generation are modified for the tensile test. The periodic conditions are removed and replaced by free surface conditions. The particles in contact with the two planes of normal in the z direction, are bonded to the planes ($R_{plane} \to \infty$ in the R^* expression). Motion is imposed to these planes to apply the imposed strain rate.

The development of cracks is simulated under different sample configurations shown in Figure 1a varying the hole position and size. In addition, experimental configurations are tested in which a hole of 2.10 mm diameter is drilled in the middle of the specimen at normal and lateral distances a and b , respectively. The following combinations are used for (a, b) values: { (3.34, 3.30); (1.83, 2.78); (0.60, 3.05) mm }. These combinations correspond to the measured distances on specimens used in three different experimental configurations. Testing of these configurations allows us to study the hole-crack interaction under various stress heterogeneity conditions. The conditions of experimental testing and material preparation are detailed in [14]. They correspond to a tensile test under a constant displacement rate of 40 µm.s^{-1} on notched specimens of dimensions of 30 mm x 10 mm x 1 mm thick. The notch size of about 0.83 mm deep is introduced at the mid-span of the specimens. Crack propagation experiments are conducted using a micromechanical testing machine with a load cell having a peak force of ±125 N and an accuracy of 0.25 N. The load frame is 0.5–125 N, The driving system is composed of two synchronised motors ensuring a displacement accuracy of 1.25 µm. The displacement range is 0.01–20 mm. The displacement rate can be tuned in the range 1.25–2000 µm s^{-1}. The specimens are glued on the fixture allowing a gage length of about 10 mm. Sample observation is performed by means of a high-speed camera mounted on stereomicroscope (Figure 2).

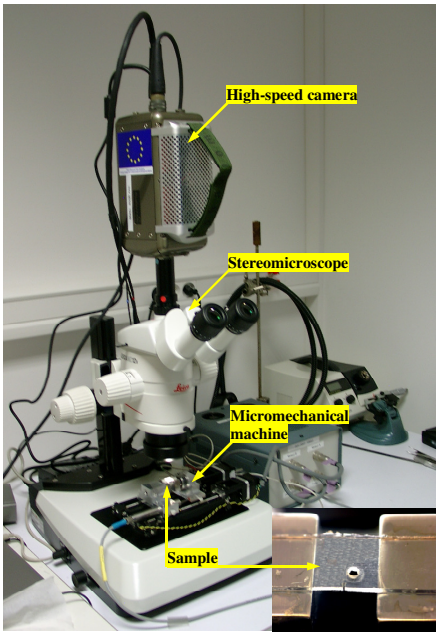

Figure 2. *Experimental set-up for fracture tests.*

3.2. Finite element method

In addition to the experimental validation of the crack propagation, finite element computation is also compared to DEM results. The method has been fully described in [14]. In all crack growth simulations, plane strain conditions are assumed with isotropic material properties (Young's modulus E = 0.312 GPa and Poisson's ratio ν = 0.3). Finite-element modelling is carried out using ANSYS package (ANSYS Inc, Canonsburg, Pennsylvania, U.S.A.). The sample geometry is chosen to fit the experimental and DEM conditions. Regular meshing is performed in 2D using quadrilateral elements defined by four nodes and two structural displacements per node. Each element in our regular mesh does not share any node with the neighbouring elements. Coupling of coincident nodes is performed prior to loading. Crack propagation is then possible by means of node decoupling. The notch has a zero lateral dimension in this case and corresponds to node decoupling through a horizontal line.

Tensile conditions are applied as displacement constraints. Nodes of the lower and upper lines are displaced in opposite directions whereas lateral displacements are forbidden.

We use the preconditioned Conjugate Gradient PCG algorithm to solve the elasticity problem. At the crack tip, stress intensity factors are computed based on nodal displacement field. Crack deviation is then decided based on the maximum energy release rate, which can be expressed as

$$\frac{\partial}{\partial\theta}\Sigma = 0 \quad ; \quad \frac{\partial^2}{\partial\theta^2}\Sigma < 0 \qquad (6)$$

Where θ is the crack orientation angle, Σ is the factor of strain energy density, which depends on the strain energy density Γ and the radial distance from the crack tip r in the following form

$$\Sigma = r\Gamma \tag{7}$$

Following the maximum release energy rate criterion, the dilatational part Γ_v of the strain energy density is the unique contributor within this principle since it tunes the volume change. It can be written as

$$\Gamma_v = \frac{(1-2\nu)(1+\nu)^2}{6E}\left(\sigma_1+\sigma_2\right)^2 \tag{8}$$

Knowing the expressions of the stress components as function of spatial variables

$$\sigma_1 = \frac{K_I}{\sqrt{2\pi r}}\cos\frac{\theta}{2}\left(1-\sin\frac{\theta}{2}\sin\frac{3\theta}{2}\right)-\frac{K_{II}}{\sqrt{2\pi r}}\sin\frac{\theta}{2}\left(2+\cos\frac{\theta}{2}\cos\frac{3\theta}{2}\right) \tag{9}$$

$$\sigma_2 = \frac{K_I}{\sqrt{2\pi r}}\cos\frac{\theta}{2}\left(1+\sin\frac{\theta}{2}\sin\frac{3\theta}{2}\right)+\frac{K_{II}}{\sqrt{2\pi r}}\sin\frac{\theta}{2}\cos\frac{\theta}{2}\cos\frac{3\theta}{2} \tag{10}$$

Where K_I, K_{II} are the stress intensity factors corresponding to the opening (tensile) and shearing (sliding) modes, respectively.

And combining the former equations leads to the expression of the optimal crack angle θc as function of stress intensity factors

$$\theta_C = \arctan\left(\frac{2K_IK_{II}}{K_{II}^2-K_I^2}\right) \tag{11}$$

Crack extension is performed on a regular grid few elements away from the former crack tip position to allows us considering small angle deviations [14].

4. Results and discussion

Figure 3 depicts crack propagation solved using both DEM and FEM for a given crack-hole configuration for a crack length of 1.25 mm. In Figures V.3a- V.3c, DEM-related normal force distributions at increasing axial strains are illustrated. The blue lines represent compressive forces whereas red lines indicate tensile forces. Figure 3a corresponds to the situation of maximum crack opening before crack departure. It indicates the development of tensile forces at the crack tip because of the crack opening. In addition, tensile forces predominate at the lateral sides of the hole whereas compressive forces dominate on both top and bottom of the hole. Heterogeneous distribution of the force takes place around the hole as a consequence of hole shape modification from circular to elliptical form. In Figures V.3b-

V.3c, evidence of crack deviation from a fully opening-mode propagation is highlighted. We notice a substantial release of the force at the back sides of the crack tip and tensile force concentration ahead the crack. Despite the absence of compressive principal stresses (S_1), a similar scenario is reproduced using FEM as shown in Figure 3d-V.3f. Both methods qualitatively represent the same evolution of stress distribution. Figure 3e-3f also indicates less sensitive crack propagation to the local mixed mode. This is attributed to the choice of the angle - stress intensity factor dependence as formerly described [14].

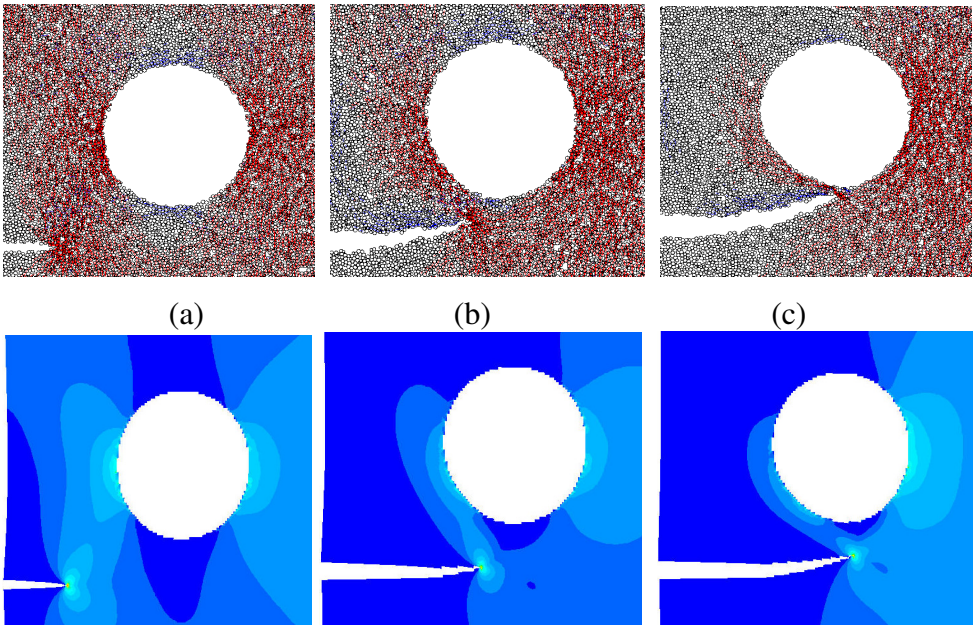

Figure 3. *Qualitative comparison between evolving force distributions in DEM ((a)-(c): blue lines = compressive forces; red lines = tensile forces), and principal stress distributions* in FEM (d)-(f), corresponding to three different crack extensions at (a,d) x=0 mm, (b,e) x=1.56 mm and (c,f) x=1.92 mm.

Figure 4 compares the predicted crack trajectories for different hole sizes using FEM, DEM and analytical method (ANM). For this purpose, we use the theoretical crack deflection function $y = x(t)$ derived from [3, 15], which has the following form (Figure 5)

$$y(x) = \frac{r^2}{2b}\left[2 - t\left(2 + t - t^2\right)\right] \tag{12}$$

With

$$t = \frac{b - x}{\sqrt{(b)^2 + (a - x)^2}} \tag{13}$$

Where x is the coordinate of the semi-infinite crack tip (Figure 5), the defect is circular (radius r) and centred at a given position (a ; b).

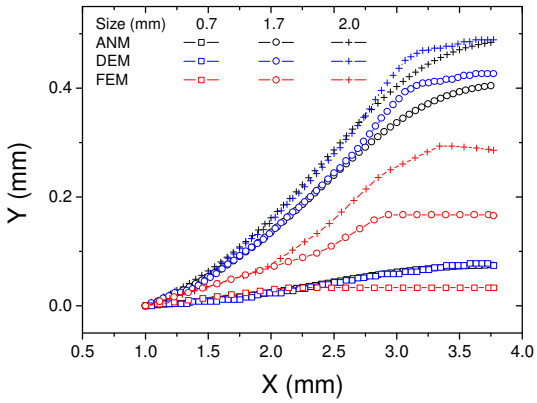

Figure 4. *Comparison between analytical and numerical crack trajectories for different hole diameter. Hole position is (2.57, 2.02) mm and crack position is (1.0, 0.0).*

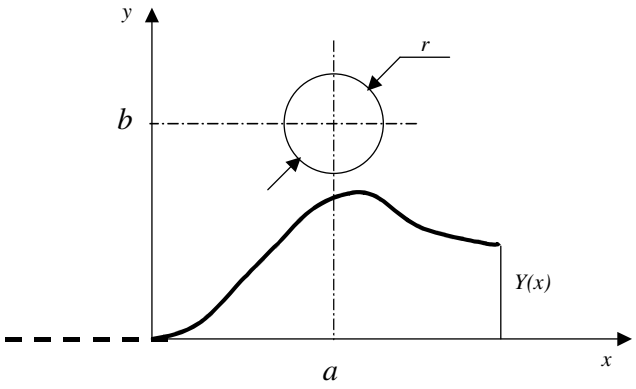

Figure 5. *Sketch of the main variables related to crack propagation in the vicinity of a stress concentrator.*

As illustrated in Figure 3 and depicted in Figure 4, change in the crack angle is minor in all cases for FEM. FEM is, in that way, less sensitive to the local mixed mode compared to DEM and ANM. DEM is closer to the analytical prediction at small crack deviations, but ends at larger angle deviations when the crack tip is closer to the hole. A larger hole size triggers a stronger hole attraction as confirmed by all techniques.

Figure 6 shows a similar analysis of the crack trajectory where several abscise positions (x) of the hole are tested. The hole diameter is fixed for all cases to 2.15 mm. The ordinate position of the hole centre is selected smaller than the ordinate position of the crack tip (*a, b*). Under these conditions, a smaller abscise (x) allows a larger shearing contribution, and, in turn, a significant crack deviation. For a highly sensitive approach to mixed mode, it even ends to

crack annihilation as in the case of DEM. The examination of the cases depicted in Figures 4 and 6, shows that DEM is in good agreement with the analytical approach as long as crack is not too close to the hole.

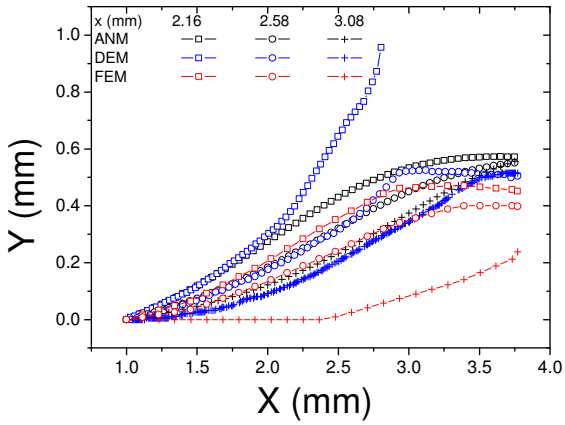

Figure 6. *Crack trajectories showing the ranking of the DEM, FEM and ANM approaches with regards to the local mixed mode. Hole ordinate position 2.02 mm, hole size= 2.13 mm.*

Figure 7a shows the crack propagation results obtained by varying the ordinate position of the hole. The comparison between the studied approaches indicates the same ranking of the crack deviation by the different methods; however, FEM is the less sensitive to local mixed mode, and comes after ANM and DEM. It suggests also that, for DEM, y positioning is less critical compared to x positioning of the hole.

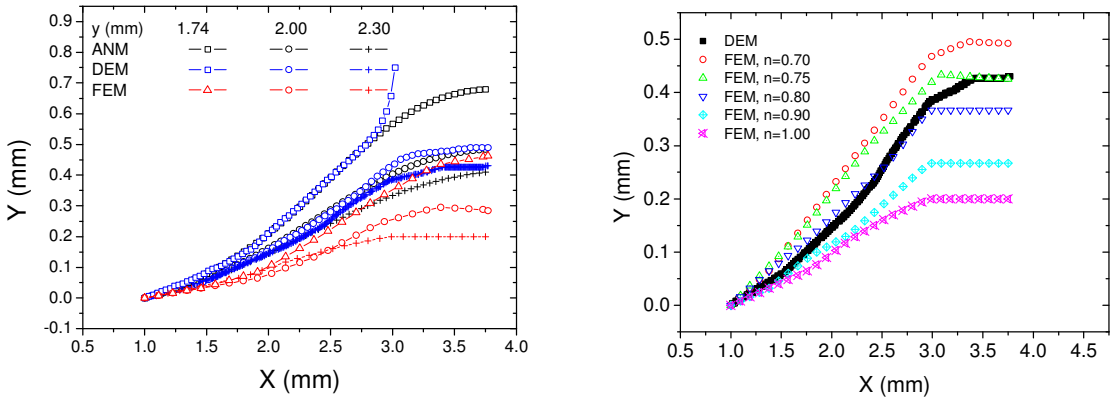

(a) (b)

Figure 7. *(a) Effect of the ordinate positioning of the hole on the crack propagation. Comparison between numerical (FEM,DEM) approaches. Hole abscise position 2.59 mm, hole size= 2.00 mm. (b) Predicted crack deviation using a modified crack angle criterion in FEM based on the ratio of stress intensity factors. Hole position (2.59, 2.30) mm, hole size= 2.00 mm.*

In order to determine what mixed mode is associated to DEM, the crack angle - stress intensity factors relationship in FEM is slightly modified from the expression given in [14] to the following form:

$$\tan(\theta) = 2\alpha^n / (\alpha^{2n} - 1) \quad (14)$$

Where

$\alpha = K_{II} / K_I$, K_I, K_{II} are the stress intensity factors associated to opening and shearing modes, n is a coefficient that measures the sensitivity to shearing mode.

FE results shown in Figure 4, 6 and 7 are obtained by setting n to unity. Deviation from the principle of maximum energy release rate is allowed by changing n towards smaller values in order to favour a more sensitive way to crack deviation. Following this idea, Figure 7b shows examples of crack deviations predicted using FEM computation by changing n from 1 down to 0.7. We obtain a more sensitive crack propagation to the mixed mode ratio (K_{II}/K_I), which becomes optimal with regards to DEM when n=0.75. But, even if the final crack position is correct, the FEM curve profile is still different from DEM curve, which means that the modified release energy criterion is definitely not the best approximation of the DEM result.

Figure 8 compares the deformed structures for three different hole positions. The result is expressed as the principal stress distribution in FEM, whereas for DEM, the colour code represents the connectivity between the bonded particles. When the notch tip is far enough from the stress concentrator (Figure 8a), DEM predicts a single crack propagation, close to the opening mode. The experimental result suggests a fragmentation process, which clearly indicates multiple crack propagation. In fact, the phenomenon of crack branching occurs in all specimens, mostly when the crack bypasses the hole. The crack splits into two or more branches.

The most complex situations are related to closer positioning of the hole to the crack tip (Figure 8b- V.8c). DEM predicts, in these cases, significant crack deviation, annihilation and then crack branching. Some of these branches do not reach the free edge of the sample because of lack of available driving force. Also, the number of branches is rather small, which again is predicted by DEM. Comparison between the DEM results in Figure 8a and Figure 8b, suggests that crack branching has to deal with local mixed mode. In contrast to this, FEM predicts no crack branching in all situations and crack trapping is only visible in Figure 8c.

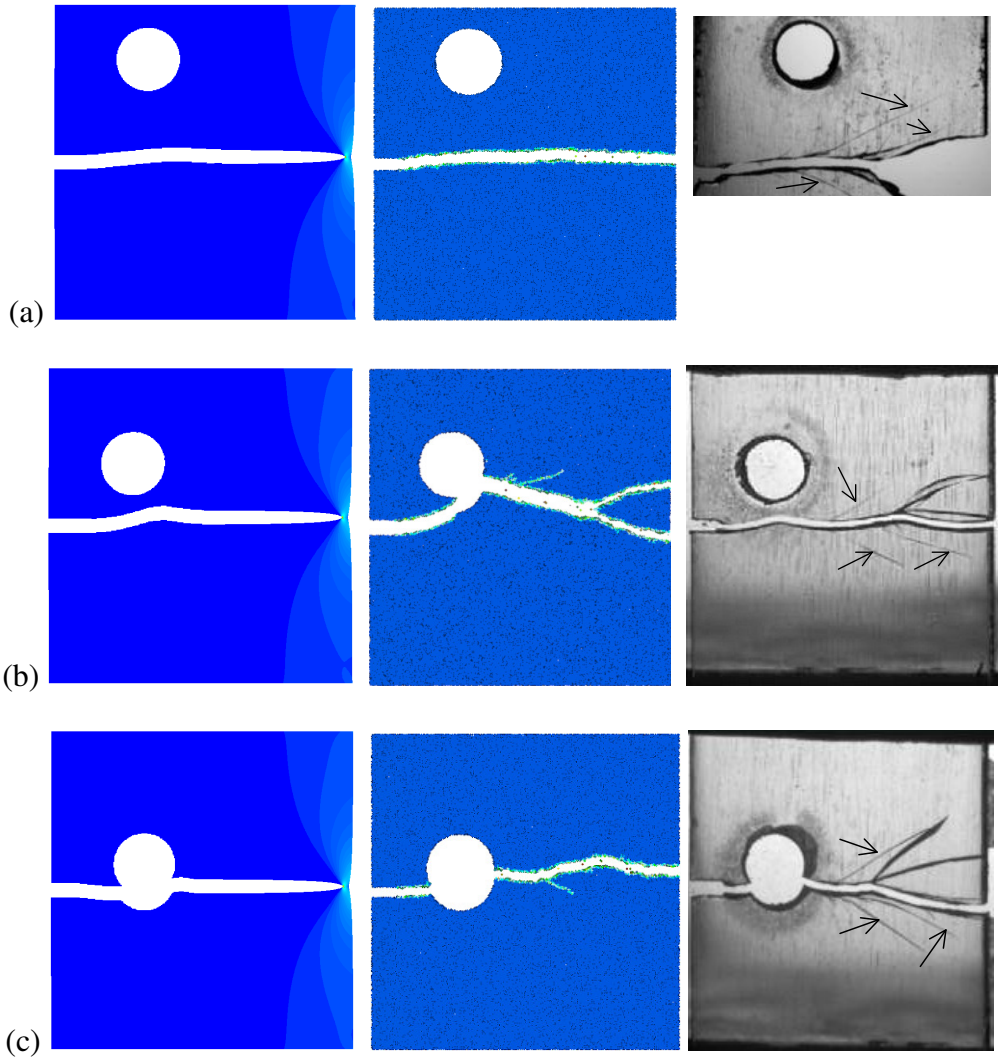

Figure 8. *Comparison between FEM, DEM and experimental crack propagation for (a)-(c) three different positions of the hole.*

Figure 9 illustrates typical mechanical responses corresponding to the experimental condition depicted in Figure 8a. Good agreement is found between the considered approaches taking as a criterion the slope of the stress-strain curves. The ultimate properties slightly differ by less than 5% for DEM and a negligible deviation for FEM, with regards to the experimental properties. We notice the unstable crack propagation, as predicted by both numerical methods, which causes the sudden drop of the stress at the break point.

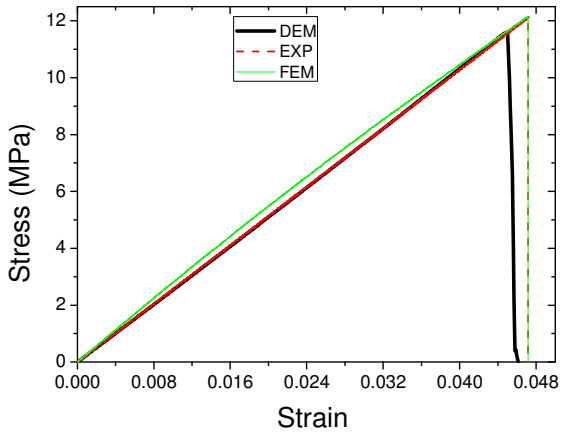

Figure 9. *Stress-strain curves predicted by FEM and DEM in Comparison with the experimental response.*

5. Conclusions

We summarize here the main results of our investigation of crack propagation in the two following statements:

- DEM proves to be highly sensitive to stress heterogeneities compared to FEM under the criterion of maximum release of elastic energy. DEM gives better results that are closer to the considered analytical model, when the crack tip is not too close to the hole.

- Crack branching is predicted by DEM under no specific criterion for the creation of secondary cracks. This result suggests that better understanding of crack branching has to include the role of local heterogeneities around the crack tip. FEM analysis should be conducted in that way to allow the departure of secondary cracks around the crack tip based on a criterion of micro-failure.

References

1. Hedjazi, L., et al., *Finite element modelling of crack propagation in carbohydrate extruded starch with open void structure.* Carbohydrate Polymers. **83**(4): p. 1696-1706.
2. Ramulu, M. and A.S. Kobayashi, *Mechanics of crack curving and branching — a dynamic fracture analysis.* International Journal of Fracture, 1985. **27**(3): p. 187-201.

3. Valentini, M., Serkov, S.K., Bigoni, D., Movchan, A.B.,, *Crack propagation in a brittle elastic material with defects.* Journal of Applied Mechanics, 1999. **66**: p. 79-86.
4. Cotterell, B. and J.R. Rice, *Slightly curved or kinked cracks.* International Journal of Fracture, 1980. **16**(2): p. 155-169.
5. Cundall, P.A., and O.D.L. Strack., *The Development of Constitutive Laws for Soil Using the Distinct Element Method.* The Development of Constitutive Laws for Soil Using the Distinct Element Method, 1979. **1**: p. 289-317.
6. Martin, C.L., D. Bouvard, and G. Delette, *Discrete Element Simulations of the Compaction of Aggregated Ceramic Powders.* Journal of the American Ceramic Society, 2006. **89**(11): p. 3379-3387.
7. Martin, C.L., D. Bouvard, and S. Shima, *Study of particle rearrangement during powder compaction by the Discrete Element Method.* Journal of the Mechanics and Physics of Solids, 2003. **51**(4): p. 667-693.
8. Balakrishnan, A., P. Pizette, and C.L. Martin, *Discrete Simulation of the Consolidation of Nano-sized Aggregated Powders.* AIP Conference Proceedings, 2009. **1145**(1): p. 105-108.
9. Potyondy, D.O. and P.A. Cundall, *A bonded-particle model for rock.* International Journal of Rock Mechanics and Mining Sciences, 2004. **41**(8): p. 1329-1364.
10. Jefferson, G., G.K. Haritos, and R.M. McMeeking, *The elastic response of a cohesive aggregate--a discrete element model with coupled particle interaction.* Journal of the Mechanics and Physics of Solids, 2002. **50**(12): p. 2539-2575.
11. Liu X., et al., *Elasticity and strength of partially sintered ceramics.* Journal of the Mechanics and Physics of Solids. **58**(6): p. 829-842.
12. Wang, Y. and P. Mora, *Macroscopic elastic properties of regular lattices.* Journal of the Mechanics and Physics of Solids, 2008. **56**(12): p. 3459-3474.
13. Martin, C.L. and R.K. Bordia, *The effect of a substrate on the sintering of constrained films.* Acta Materialia, 2009. **57**(2): p. 549-558.
14. Hedjazi, L., et al., *How cracks propagate in a vitreous dense biopolymer material.* Engineering Fracture Mechanics. **78**(6): p. 1328-1340.
15. A.B. Movchan, N.V.M., *Movchan, Mathematical Modelling of Solids with Non-Regular Boundaries,.* CRC Press, Boca Raton, FL, 1995.

Partie 2

Modélisation, basée sur la structure cellulaire réelle, de la compression d'une céréale petit déjeuner par la Méthode des Eléments Discrets

Article.6

Discrete element method to study fragmentation in biopolymer cellular materials

Discrete element method to study fragmentation in biopolymer cellular materials

L. Hedjazi[1,2*] , C. L.Martin[2], S. Guessasma[1] , G. Della Valle[1], R. Dendievel[2]

[1] INRA, UR1268 BIA, Rue de la Géraudière, Nantes 44316.

[2] Laboratoire SIMAP, Grenoble-INP/UJF/CNRS, 101, rue de la physique, BP 46, 38402 Saint Martin d'Hères cedex

* Corresponding author

Phone. +33 (0)2 40 67 50 36, fax.+33(0)2 40 67 51 67

E-mail address: lotfi.hedjazi@nantes.inra.fr

1. Abstract

The fragmentation behaviour of brittle airy cereal food is studied both numerically and experimentally. The food item is subjected to severe compression until densification stage. Experimental evidence of typical cellular material behaviour is pointed out including elasticity, cell collapse and densification regimes. In order to better explain the observed behaviour, especially the resulting fragmentation, a numerical approach is proposed based on discrete element method. Predicted results show good agreement with experimental mechanical responses. Moreover, large size fragments are found to form as a consequence of small rupture events.

Keywords:

Cellular structure; X-ray microtomography; fragmentation; Starch; Discrete element method

2. Introduction

Fragmentation of brittle cellular solids is one of the most fundamental problems in applied mechanics, and it is of considerable scientific and industrial interests(Chau et al 2000; Harireche & McDowell 2003; Sun & Xu 2008). A great number of experimental (Peleg 1997; Peroni et al 2006), numerical (Caty et al 2008; Guo & Gibson 1999) and analytical (Ford & Gibson 1998; Kitazono et al 2002) studies on the behaviour of cellular materials under quasi-static loading have been reported in past decades (D'Addetta et al 2001). The most important feature may be the following: the behaviour of a cellular material can be derived from the

properties of the constitutive material (cell wall material) and its relative density with a reasonable accuracy (Ashby & Gibson 1988). The stress–strain curve, for a cellular solid in compression, is characterized by three regimes: (1) a linear elastic regime driven by cell edge bending or face stretching, (2) a stress plateau corresponding to progressive cell collapse by elastic buckling, plastic yielding or brittle crushing, depending on the nature of the constitutive material and, (3), densification, corresponding to the collapse of the cells throughout the material and subsequent loading of the cell edges and faces against one another.

In food science, resistance to compressive stresses is an important physical signature of the processed food as it represents an intrinsic component of its texture (McDowell & Humphreys 2002; Guessasma et al 2011). It may represent, moreover, the prevailing mechanism that explains the mastication behaviour of many brittle food products like breakfast cereals (Yven et al 2010). Mechanical properties of bread also include sponginess because bread has compressive behaviour similar to that of many solid foams (Peleg et al 1989; Scanlon et al 2000). One of the most determinant factors that affect the compression behaviour is the void arrangement within the airy structure. Determination of key relationships between mechanical parameters and structural attributes has attracted many research (Guessasma et al 2008). It became then necessary to have a precise idea of the complexity of the 3D structure of food items (Babin et al 2007). Three-dimensional characterisation and visualisation of porous materials by X-ray tomography has nowadays become an important and powerful tool in that respect. The general principle of the tomography technique has been described in numerous papers (Landis & Keane 2010; Olmos et al 2009). The technique reveals several structural features in static and under loading conditions(Lhuissier et al 2009; Vasic et al 2010). Even such information is not sufficient to determine the compression behaviour of solid foams since analytical mechanical models are not capable of handling such complexity. Numerical modelling is then considered as an alternative to relate the structural information to some mechanical parameters through adequate simulation. Among the known techniques, finite element computation has been able to predict the mechanical behaviour of various porous media (Babin et al 2005; Guessasma et al 2008). The method is usually accurate when it is used to virtually test porous materials under small strain conditions. However, at large strains, the method is quite limited since many problems due cell wall contact and element distortion are encountered.

The Discrete element method (DEM) is an alternative that avoid the above mentioned drawbacks since it is a mesh free method (D'Addetta et al 2001). It has been developed to

study the dynamics of granular media (D'Addetta et al 2001; Harireche & McDowell 2003). But it is more and more involved in the prediction of mechanical behaviour of polymer foams(Mills & Gilchrist 2007; Viot et al 2010), where the material is typically assembled using a large number of discrete units. It has been proposed recently to tackle several challenges related to food technology including texture analysis and human mastication behaviour (McDowell & Humphreys 2002; Sun & Xu 2008).

In this paper, we are concerned by the implementation of discrete element method to study the fragmentation of a typical brittle airy food, namely breakfast cereals. This study combines DEM analysis with experimental characterisation of 3D cellular structure of the food item, in order to relate the predicted response to the observed mechanical behaviour.

3. Experimental layout

A specific commercial breakfast cereal, named "Miel Pops" is selected as material fro this study (Figure 1a). It is a brittle product the texture properties of which have been studied in a previous paper (Sandoval et al 2008). The chemical composition is as follows: Lipids 1.13 %, starch 61.8 % and Sugars 37.07 %. It has an ellipsoidal shape, the approximate dimensions of which are 9.07±0.78 x 11.83±0.55 x 13.28±0.75 mm^3. Mechanical testing is performed to study crushing properties of the product assuming that it can represent a simplified human mastication process. Crushing properties will be thus important to determine the capability of this food product to fragmentation. Compression tests are performed using an Instron testing machine model 1122 (Figure 1b). The product is deformed up to a conventional strain of 80% and at a constant velocity of 0.83 $mm.s^{-1}$. Force – displacement signature of the product is recorded and up to 20 replicates are used to derive average behaviour and assess dispersion.

The 3D void structure of food item has been determined by synchrotron radiation at the ID19 beamline from the ESRF facility in Grenoble (France). The number of radiographic images needed for 3D feature reconstruction ranges from 1200 to 1500 depending on samples. The beam energy is 17.6 keV and the resolution is 6.47 µm. With such a small resolution, the whole object needs to be built in several stages by gathering numerous stacks. Typically, up to ten stacks are required to build an object of centimetre size. The acquisition leads to crop volumes in the range 4.2 - $8.6x10^9$ voxels. Separation between the solid and the void is clearly established thanks to a good contrast between phases. Image processing is performed using the public domain software ImageJ. After converting the image from 32 to 8 bits type, no particular losses of details is noticed. Conversion to 8 bits images helped to decrease the CPU time for processing large size images. Thresholding of the grey-level images is then

performed to obtain a clear separation between dense and void phases. Due to limitation of computation resources, the resolution has to be decreased and the effect of this loss of sensitivity on several image attributes has to be discussed. Among these attributes, cell size and wall cell size distributions are determined using granulometry technique (Guessasma et al 2008). Octahedral structuring element is grown numerically and the scores for each size class are saved. In addition to size distributions, the relative density ρ of the structure is computed. This quantity can be defined as

$$\rho=\sum_{i=1}^{V}\delta i/V \quad |\delta=1 \quad | \; ni=255 \;\; ; \;\; \delta=0 \; | \; ni=0 \qquad \text{and} \qquad \text{Porosity} = 1 - \boldsymbol{\rho} \qquad (1)$$

where V is the volume of the cellular material as a voxel count. δ is a threshold function of the grey level ni of the image which takes either 0 or 255 for black and white, respectively.

In order to compute the relative density, we need a precise quantification of the object contour. A wrap technique is used to determine the contours of the sample. This technique is efficient for contour detection even if open pores are present at the surface. The contour surface is built by the displacement of a hard disk of radius r=10 voxels along the solid phase edges.

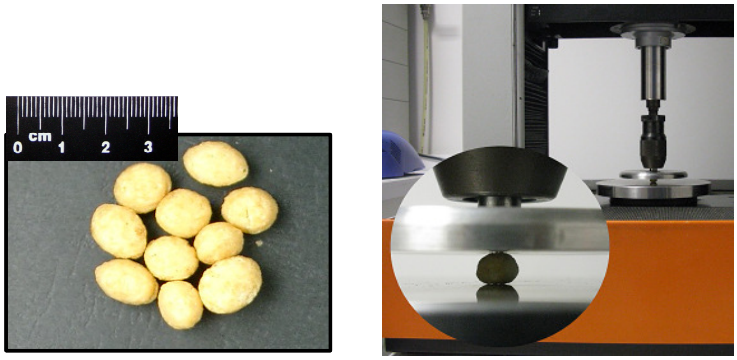

(a) (b)

Figure 1. *(a) Pieces of the studied breakfast cereal . (b) Experimental setup showing uniaxial loading of the food item.*

4. Modelling technique

The structure of the food item is converted into a discrete assembly of monomodal spheres. Each voxel in the image is replaced by one sphere. Due to the limited computation resources, we worked with an intermediate resolution, where the physical dimension of a given voxel is 29.84 µm. This dimension corresponds also to the diameter of the spheres in the discrete assembly that is built with more than one million units (i.e., spheres). The sample volume, as

computed from x-ray tomography image, is 702 mm^3, a value very close to the overall volume taking into account ellipsoid shape approximation, i.e. 744±51 mm^3.

Two planes are used as boundary conditions in the z-direction to impose crushing while periodic conditions are used for lateral directions. Physical properties are associated to each contact, allowing resistance to compression, tension and bending to form, while imposing relative displacement between the two spheres. Contact properties thus consist of normal and tangential stiffness, resisting moments and strength parameters. Denoting R_1 and R_2 the particle radii (see Figure 2), the equivalent radius R^* is written as:

$$R^* = \frac{R_1 R_2}{R_1 + R_2} \tag{2}$$

The bond radius is denoted as a_b, while the normalized bond radius, a^*, is defined as:

$$a^* = \frac{a_b}{2R^*} \tag{3}$$

The normal and tangential components of the bonding force between two spheres with equivalent radius R^* is:

$$N = \Sigma_N a^* R^* u_N \ , T = -\Sigma_T a^* R^* u_T \tag{4}$$

where u_N and u_T are the accumulated normal and tangential displacements at the contact point. Σ_N and Σ_T are material parameters with stress dimension. These parameters are adjusted to fit the observed elasticity behaviour of dense starch material.

Normal forces are either compressive or tensile forces. Tangential forces oppose the accumulated tangential displacement representative of local shear. The bonded contacts transmit resisting moments in the normal and tangential directions:

$$M_N = -2\Sigma_T \left(a^* R^*\right)^3 \theta_N \ , M_T = -\Sigma_N \left(a^* R^*\right)^3 \theta_T \tag{5}$$

where θ_N and θ_T are the accumulated relative rotations in the normal and tangential directions (Figure 2).

Solid material fracture at the scale of the discrete units (i.e., spheres) is accounted thanks to a bond fracture criterion applied to the contact volume approximated as a cylindrical beam. Maximum tensile and shear stresses at the bond can be thus derived using beam theory as follows (Potyondy et al 2004):

$$\sigma_N = \frac{N}{4\pi\left(a^* R^*\right)^2} + \frac{\left|M_T\right|}{2\pi\left(a^* R^*\right)^3} \quad , \quad \sigma_T = \frac{\left|T\right|}{4\pi\left(a^* R^*\right)^2} + \frac{\left|M_N\right|}{2\pi\left(a^* R^*\right)^3} \tag{6}$$

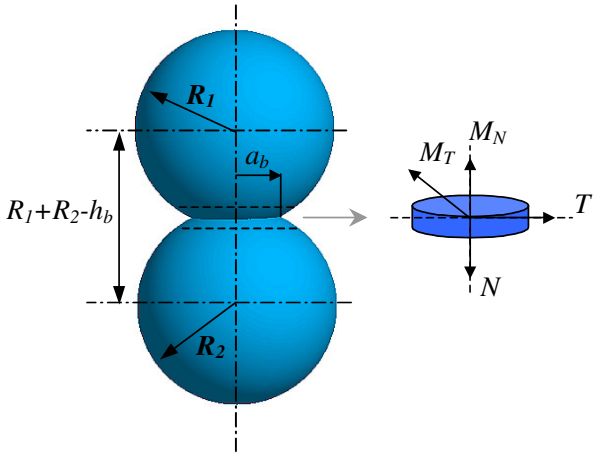

Figure 2. *Contact model between bonded spheres.*

Mechanisms leading to fracture can be related to either tensile, shear or bending deformation of the beam. In our case, we assume that fracture occurs under the conditions:

$\sigma_N > \Sigma_c$ or $\sigma_T > \Sigma_c$ (7)

where Σ_c is a material property representing the strength of the solid bond. It can be adjusted depending on the observed resistance of the product. In our case, it is adjusted to match observed fracture behaviour of dense brittle starch, as studied precedingly.

Two particles may resume contact after the original bonded contact has failed. We assume that this occurs when the interparticle distance is the same as that when the solid bond failed (Figure 2). This situation occurs at densification stages where resistance is essentially driven by the solid material after disappearance of a large part of the cellular structure. When the contact is resumed, the normal stiffness in compression is conserved while the tensile stiffness is null. In addition to contact forces, friction is accounted for any broken bond by modulating the tangential force during sliding thanks to the implementation of a Coulomb-like law.

5. Results and discussion

5.1. Cellular structure

Figure 3 depicts transparent and surface views of a typical 3D structure of Miel Pops. The crop dimensions are 14.92 x 12.46 x 12.38 mm^3. The surface view represents the external envelope of the food item as computed using wrap technique. The relative density of the product is 0.28 indicating that the structure is an open cell structure with more than 70% of

the material occupied by air. Cross-sections of the same structure in z-direction (Figure 4) indicate a fine solid phase arrangement and a more complex form compared to the apparent spherical shape (Figure 1a).

Another interesting feature appears to be a thin solid skin surrounding the void structure which may be inferred to the design process. The voxel count corresponding to the solid phase is larger than 10^8 voxels. Converting an image containing this huge number of solid units to a discrete assembly is not possible using conventional computation resources. The decrease of the resolution is then attempted to a certain degree to ensure that the number of solid units lies under 10^6 voxels. We define a subresolution index (n) that measures the roughening of the structure induced by increasing the pixel size

$$d^* = n.d_0 \qquad (8)$$

where d_0= 6.47 µm is the original pixel size, d^* is the pixel corresponding to a given integer value n.

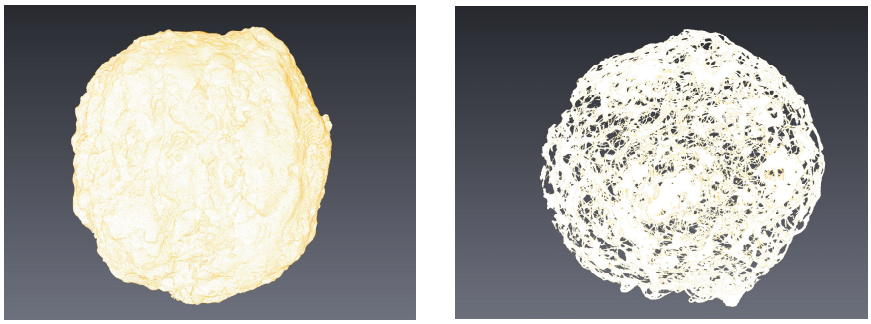

(a) (b)

Figure 3. *(a) Surface and (b) transparent views of Miel Pops as determined using X-ray tomography. Crop dimensions are 835x759x830 voxels where the voxel size is 14.92 µm.*

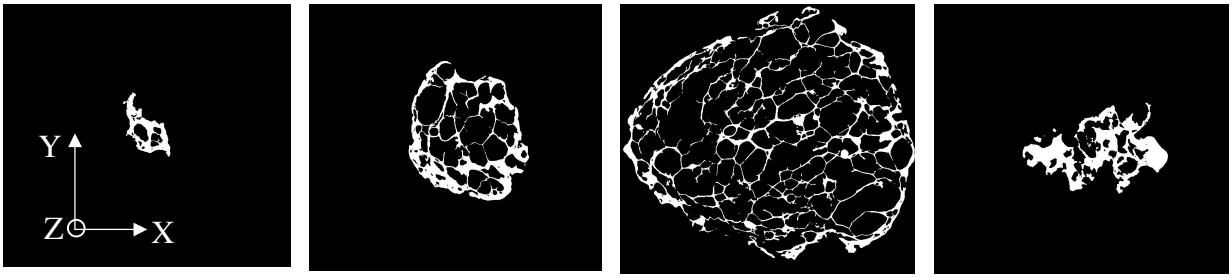

(a) (b) (c) (d)

Figure 4. *Cross-sections in the cellular material at different z depths (a) 16 voxels (0.24 mm), (b) 83 voxels (1.24 mm), (c) 402 voxels (6.01 mm), (d) 791 voxels.*

Table 1 show that the relative density varies by 4% when n is doubled. The change becomes non negligible (about 21%) when n = 8. Figure 5 shows the distribution of the cell size and cell wall thickness for the same resolutions expressed in a cumulative referential. The effect of resolution is remarkable on the cell size distribution compared to the cell wall thickness distribution. In the case of the cell wall distribution, a slight change is observed when n=4. Average quantities are extracted from these distributions and summarised in Table VI.1. The overall changes due to resolution are 16% and 28% for cell wall thickness and cell size, respectively.

Table 1: Structural properties of the food piece as function of resolution.

Subresolution index	8	4	2
voxel size d* (µm)	59.68	29.84	14.92
relative density ρ (-)	0.34	0.29	0.28
average cell wall thickness (µm)	88.86	80.40	76.76
average cell size (µm)	219.14	266.63	304.09

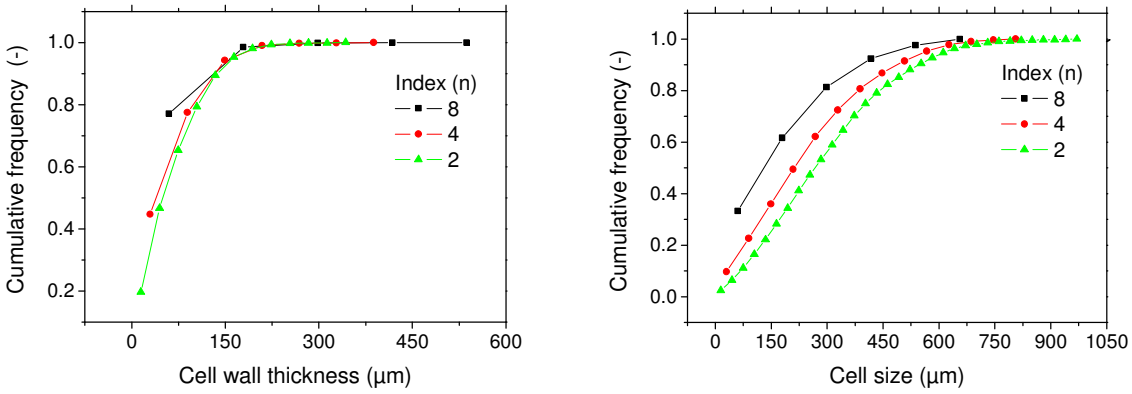

(a) (b)

Figure 5. *Effect of resolution on the (a) cell wall thickness and (b) cell size distributions.*

5.2. Experimental compression

Figure 6 shows compression responses of several food pieces. We distinguish three main stages that are common to all observed trends. The first stage represents a quasi-linear elastic response of the cellular material. Deformation mechanisms responsible for material resistance are basically inferred to cell wall by bending and uniaxial deformation if cells are thick

enough. The slope of the curve in the first stage is 19±8.1 N.mm^{-1} whereas the displacement cut-off separating the elastic regime from the nonlinear one is 0.8±0.3 mm. The peak force that immediately follows the elastic domain is 24.9±8.7 N. The slope here cannot be simply related to a Young's modulus because the contact area between the sample and the plates evolves during compression, and more generally, because of the complexity of the sample shape. The second stage is a large collapse plateau corresponding to successive events of cell wall rupture. Our results show that the plateau width is 8.6±1.3 mm. The third stage consists in the crushing of cells and the beginning of cell wall resistance to imposed deformation. This stage is characterised by a rapid stress increase with a slope of about 162±66 N.mm^{-1}.

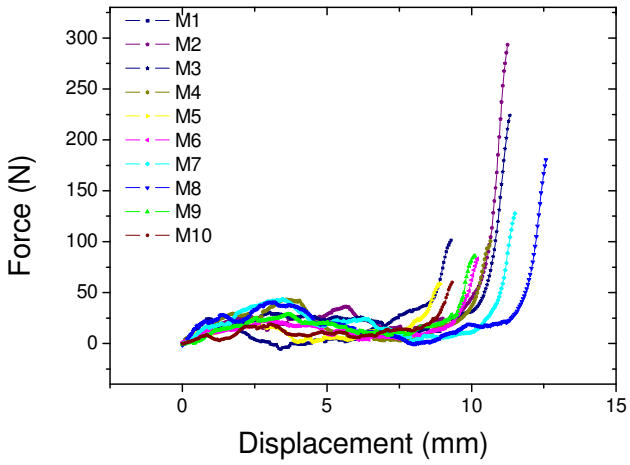

Figure 6. *Typical compression responses of the studied cereal food.*

Visual observation of the fragments after testing shows that despite severe mechanical compression, large fragments are formed together with a large number of very small fragments (Figure 7). Intuitively, a more homogeneous and smaller size distribution could have been expected because of the fine structure revealed using X-ray tomography. In order to provide more explanation about the observed evidences, simulation of mechanical degradation is considered using discrete element method.

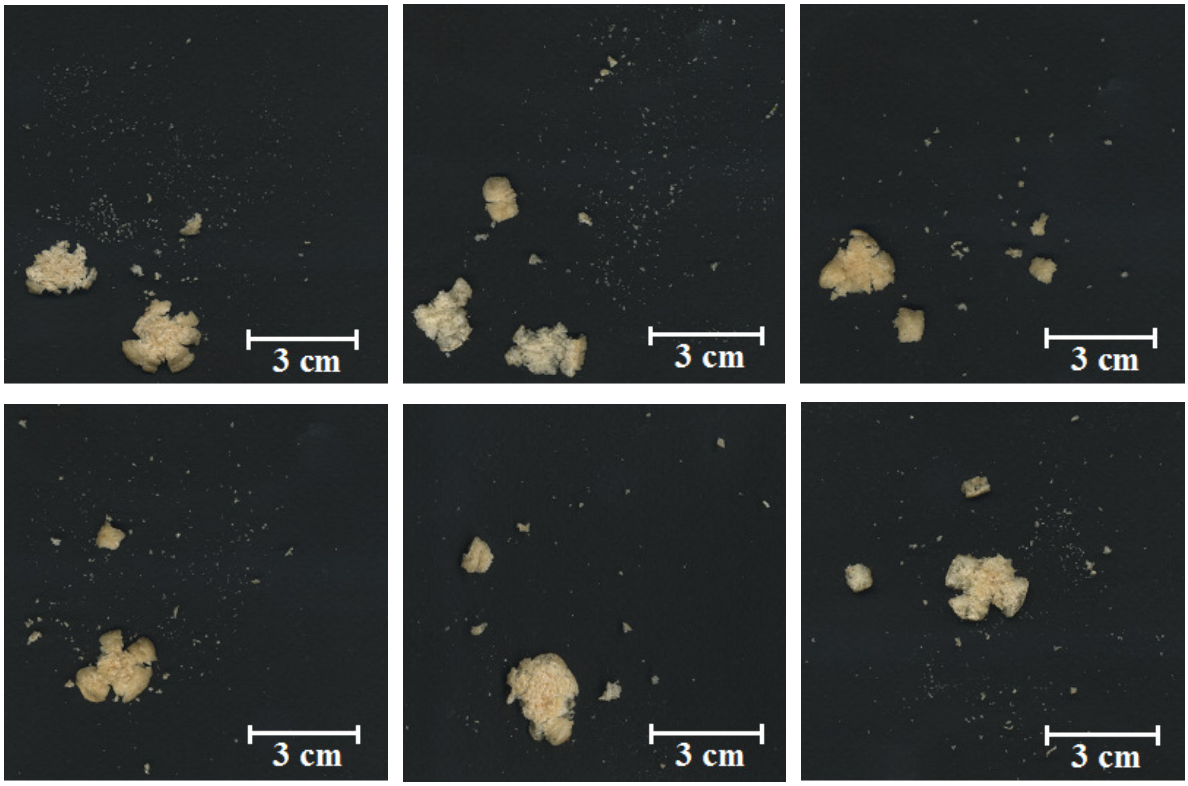

Figure 7. *Fragment size distribution after compression.*

5.3. Compression simulation

Figure 8 shows the discrete element structure after a slight densification that allows strain accumulation between bonded spheres.

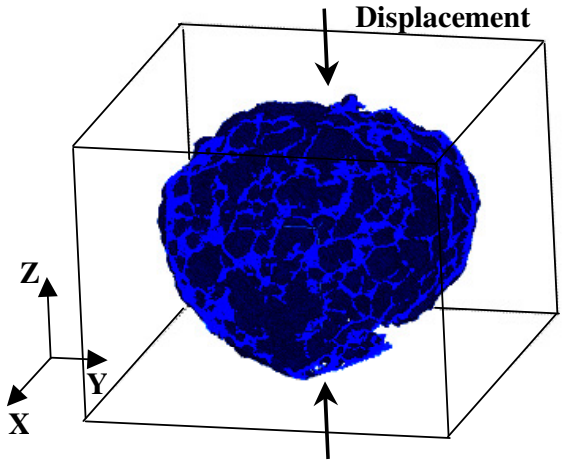

Figure 8. *Miel Pops geometry converted from X-ray tomography to a discrete assembly of spheres. The sample orientation is also illustrated in the simulation box.*

The structure contains 918 257 spheres. Boundary conditions are similar to the experimental conditions. The total force acting on the platen is calculated from all the reaction forces at each displacement increment up to a conventional deformation of 76 %. The computation took approximately 6 weeks to achieve the imposed strain on a workstation equipped with 4 cores - Xeon 2 - X5560 processors and 24 Gbytes and with a openMP parallelization of the code.

Figure 9 depicts the numerical force - displacement response and the evolution of percentage of broken bonds as function of the imposed strain. The predicted mechanical response is quite typical of a cellular material behaviour under compression(Viot et al 2010; Wang et al 2011; Zhu et al 1997). It is also similar in all stages to the observed trends in Figure 6. The first peak force beyond the elastic domain is 24 N, which is very close to the average value of measured forces. However, the initial slope (5.2 N. mm^{-1}) is four times smaller than the experimental result. This may be due to the fact that in the numerical sample, only two spheres are initially contacting the platens, whereas the real samples have a much larger contact area. The maximum elastic displacement is approximately 0.8 mm, which is close to the experimental value.

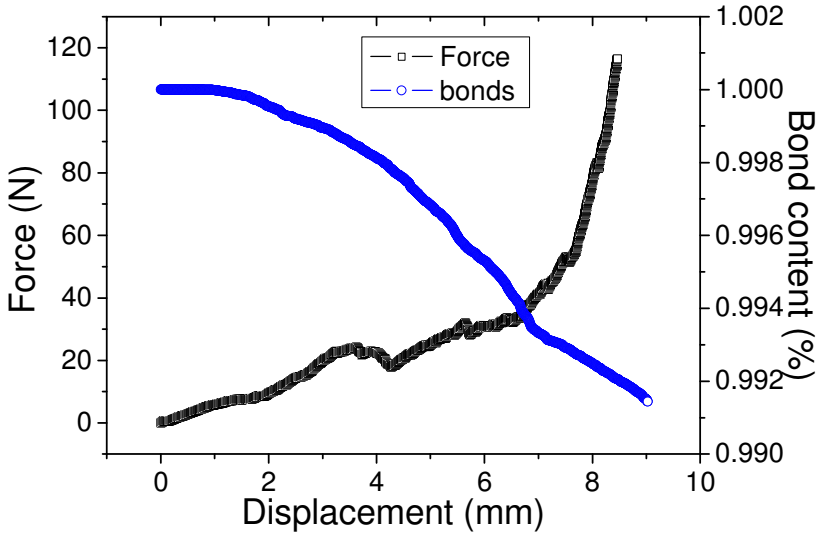

Figure 9. *Mechanical response and percentage of unbroken bonds corresponding to the simulation of compression.*

The percentage of unbroken bonds is plotted as a function of the imposed strain. The total number of bonds is 1.98×10^6, while the number of broken bonds increases only up to 1.7×10^4. The small broken bond content (<2%) indicates that only a small portion of the imposed

structural displacement is transmitted to the material as deformation. In other words, strain localization arises. This result is not surprising since the relative density of the material is small enough to allow large structural displacements inside the cellular structure. At the beginning of the compression, the number of unbroken bonds equals the initial bond content indicating that up to 0.78 mm, the predicted reaction force represents the response of the intact cellular material. Beyond this cut-off, the broken bonds growth is continuous and irregular, especially at the densification stage where a slower progress is noticed.

Figure 10 illustrates the final fragments obtained after simulation. Colour coding is used to separate cohesive blocks to clearly highlight the number of fragments. Large fragments remain even at the final stage of simulation. The two largest fragments are volumes consisting of 391 644 and 395 600 units and together represent 86% of the whole total number of spheres in the structure.

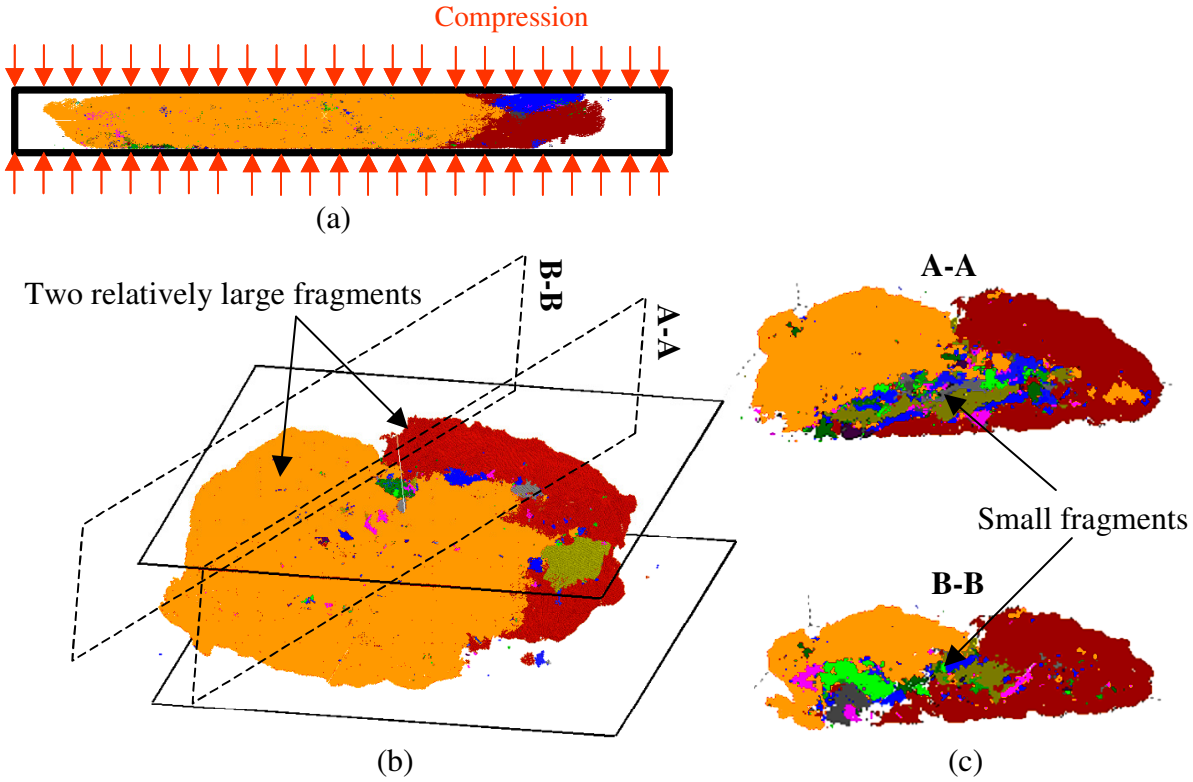

Figure 10. (a) lateral, (b) perspective and (c) cross-section views showing food fragments at final stage of compression in the numerical simulation.

In order to compare the resultant fragment size distribution to the experimental ones, conversion of fragment areas to volumes is considered. For this purpose, we approximate fragments as cylinders of constant height. This height corresponds to the distance left after

complete compression (4.25 mm). Using this approximation, the largest structure generated in the simulation has a volume of about 105 mm^3. 2D images of the fragments in Figure 7 are processed taking away fragment areas lower than 10 pixels (<1 mm^2). The largest fragment has a volume of about 117±10 mm^3, which is 10% larger than the numerical prediction. We use a cumulative volume distribution so that small size fragments would have a minor contribution. Figure 11 compares the experimental and numerical fragment volume distributions. Despite the rough approximation about the volume - area conversion, DEM gives a realistic prediction of the fragment volume distribution.

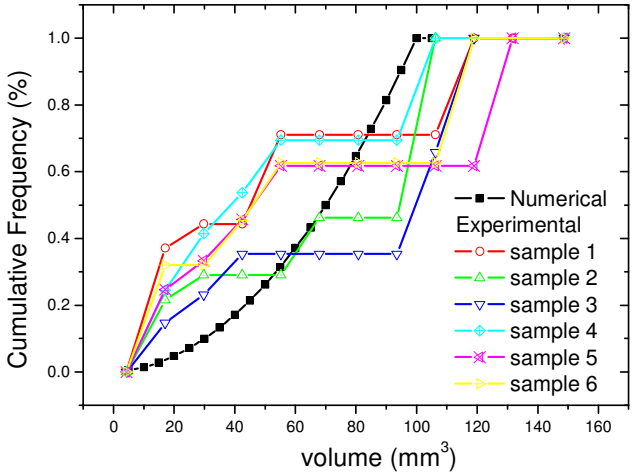

Figure 11. *Comparison between experimental and numerical volume distributions of fragments at the end of compression.*

In order to ascertain a more quantitative view of the differences between experimental and numerical distributions, we have fitted all curves using Gompertz growth model:

$$f(v) = a\exp\left(-\exp\left(-k\left(v - v_c\right)\right)\right) \qquad (9)$$

where f is the volume frequency associated to volume class v, a, v_c and k are fitting constants determined for each curve.

Since all curves are upper bounded ($f(v \to \infty) = 1$) then the amplitude a=1 in all cases.

The numerical distribution follows Gompertz growth model with an excellent correlation factor (R^2=0.998) whereas for experimental distributions $R^2 \geq 0.75$. vc expresses the centre of the growth function where $f(v_c)=f(a/2.718)$. It is found that the numerical value (v_c= 90 mm^3) is larger by a factor of two than the experimental value (v_c=42±16 mm^3). However, the values obtained for coefficients (k) from numerical (0.019) and experimental (0.02±0.05) curves are close to each other.

6. Conclusions

Structural analysis of a cereal breakfast using X-ray tomography reveals a airy structure with a total porosity of 78% , containing 100 µm thick solid struts and an average pore size three times thicker. Compression up to a conventional deformation of 80% reveals a standard cellular material behaviour. The analysis of fragments indicates a heterogeneous distribution of fragment size containing few fragments of large size and a large number of small ones. Discrete element method is used as an original approach to explain why the fine cellular structure results in a heterogeneous fragmentation process. The predicted results highlight few rupture events (less than 2%), with contrast to the large imposed displacement. Only small part of the mechanical energy is converted into an effective strain that contributes to material rupture. Good agreement is then found between the numerical and experimental fragmentation process as attested by the final size distributions.

References

Ashby MF, Gibson LJ. 1988. Cellular Solids - Structure and Proprties. *Oxford : Pergamon Press*,532

Babin P, Della Valle G, Dendievel R, Lourdin D, Salvo L. 2007. X-ray tomography study of the cellular structure of extruded starches and its relations with expansion phenomenon and foam mechanical properties. *Carbohydrate Polymers*, *68*,329-40

Babin P, Valle G, Dendievel R, Lassoued N, Salvo L. 2005. Mechanical properties of bread crumbs from tomography based Finite Element simulations. *Journal of Materials Science*, *40*,5867-73

Caty O, Maire E, Youssef S, Bouchet R. 2008. Modeling the properties of closed-cell cellular materials from tomography images using finite shell elements. *Acta Mater.*, *56*,5524-34

Chau KT, Wei XX, Wong RHC, Yu TX. 2000. Fragmentation of brittle spheres under static and dynamic compressions: experiments and analyses. *Mech. Mater.*, *32*, 543-54

D'Addetta G, Kun F, Ramm E, Herrmann H, Vermeer P, et al. 2001. From solids to granulates - Discrete element simulations of fracture and fragmentation processes in geomaterials

Continuous and Discontinuous Modelling of Cohesive-Frictional Materials. pp. 231-58: Springer Berlin / Heidelberg

Ford CM, Gibson LJ. 1998. Uniaxial strength asymmetry in cellular materials: an analytical model. *Int. J. Mech. Sci.*, *40*,521-31

Guessasma S, Babin P, Della Valle G, Dendievel R. 2008. Relating cellular structure of open solid food foams to their Young's modulus : finite element calculation. *International Journal of Solids and Structures*, *45*,2881-96

Guessasma, S., et al., *Mechanical modelling of cereal solid foods.* Trends in Food Science &Technology, 2011. **22**(4): p. 142-153.

Guo XE, Gibson LJ. 1999. Behavior of intact and damaged honeycombs: a finite element study. *Int. J. Mech. Sci.*, *41*,85-105

Harireche O, McDowell GR. 2003. Discrete element modelling of cyclic loading of crushable aggreates. *Granular Matter*, *5*,147-51

Kitazono K, Sato E, Kuribayashi K. 2002. Micromechanics analysis for elastic modulus, coefficient of thermal expansion and thermal conductivity of anisotropic closed-cell metal foams. *Journal of the Japan Institute of Metals*, *66*,53-9

Landis EN, Keane DT. 2010. X-ray microtomography. *Mater. Charact.*, *61*,1305-16

Lhuissier P, Fallet A, Salvo L, Brechet Y. 2009. Quasistatic mechanical behaviour of stainless steel hollow sphere foam: Macroscopic properties and damage mechanisms followed by X-ray tomography. *Materials Letters*, *63*,1113-6

McDowell GR, Humphreys A. 2002. Yielding of granular materials. *Granular Matter*, *4*,1-8

Mills NJ, Gilchrist A. 2007. Properties of bonded-polypropylene-bead foams: data and modelling. *Journal of Materials Science*, *42*,3177-89

Olmos L, Martin CL, Bouvard D, Bellet D, Di Michiel M. 2009. Investigation of the Sintering of Heterogeneous Powder Systems by Synchrotron Microtomography and Discrete Element Simulation. *Journal of the American Ceramic Society*, *92*,1492-9

Peleg M. 1997. Review: Mechanical properties of dry cellular solid foods. *Food Science and Technology International*, *3*,227-40

Peleg M, Roy I, Campanella OH, Normand MD. 1989. Mathematical Characterization of the Compressive Stress-Strain Relationships of Spongy Baked Goods. *Journal of Food Science*, *54*,947-9

Peroni L, Avalle M, Martella P. 2006. Multiaxial characterization of the mechanical behaviour of aluminium foam. *High Performance Structures and Materials Iii*, *85*,249-58

Potyondy, D.O. and P.A. Cundall, A bonded-particle model for rock. International Journal of Rock Mechanics and Mining Sciences, 2004. 41(8): p. 1329-1364.

Sandoval AJ, Chaunier L, Courcoux P, Della Valle G. 2008. Bulk mechanical behavior of commercial particle food foams. *J. Texture Stud.*, *39*,405-25

Scanlon MG, Sapirstein HD, Fahloul D. 2000. Mechanical Properties of Bread Crumb Prepared from Flours of Different Dough Strength. *Journal of Cereal Science*, *32*,235-43

Sun Y, Xu WL. 2008. Simulation of food mastication based on discrete element method. *15th international conference on mechatronics and Machine vision Practice*, p. 201. Auckland, New-Zealand

Vasic S, Grobéty B, Kuebler J, Graule T, Baumgartner L. 2010. XRCT characterisation of Ti particles inside porous Al2O3. *Mater. Charact.*, *61*,653-60

Viot P, Bouix R, Iordanoff I, Lataillade JL. 2010. Deformation localisation modelling of polymer foam microstructure under compression: A new approach by discrete element modelling. *Compos. Struct.*, *92*,585-92

Wang Z, Shen J, Lu G, Zhao L. 2011. Compressive behavior of closed-cell aluminum alloy foams at medium strain rates. *Materials Science and Engineering A*, *528*,2326–30

Yven C, Guessasma S, Chaunier L, Della Valle G, Salles C. 2010. The role of mechanical properties of brittle airy foods on the masticatory performance *J. Food Eng.*, *101*,85-91

Zhu HX, Knott JF, Mills NJ. 1997. Analysis of the elastic properties of open-cell foams with tetrakaidecahedral cells. *J. Mech. Phys. Solids*, *45*,319-343

Chapitre V : Résultats majeurs et synthèse des travaux

1. Rappel de la démarche

L'objectif de ce travail est de développer un modèle mécanique de mastication des aliments céréaliers fragiles. Ce modèle mécanique s'appuie sur des concepts de la mécanique de la rupture, d'une connaissance des propriétés et de la structure des produits céréaliers et des conditions réelles de la mastication (Figure 1a). Ce travail a été effectué en trois étapes dont le bilan est présenté ci-après en respectant cette logique:

1) Un modèle en éléments finis a été développé afin de déterminer les **mécanismes et des critères de propagation de fissures** dans les produits céréaliers (Figure 1b). Le modèle est consolidé par une démarche expérimentale visant à le valider par des essais mécaniques sur les produits denses et alvéolaires en présence de pré-fissures. L'amidon amorphe est choisi comme matériau d'étude car il constitue la base des aliments céréaliers.
2) Les **conditions** réelles **de mastication** ont été établies lors d'une campagne expérimentale de mastication humaine (acquisition EMG, profil masticatoire, analyse des bols des produits mastiqués), et ces conditions ont été simulées par un modèle en éléments finis, intégrant la structure cellulaire de l'aliment.
3) **La fragmentation** des produits céréaliers ont été modélisées par la méthode des éléments discrets.

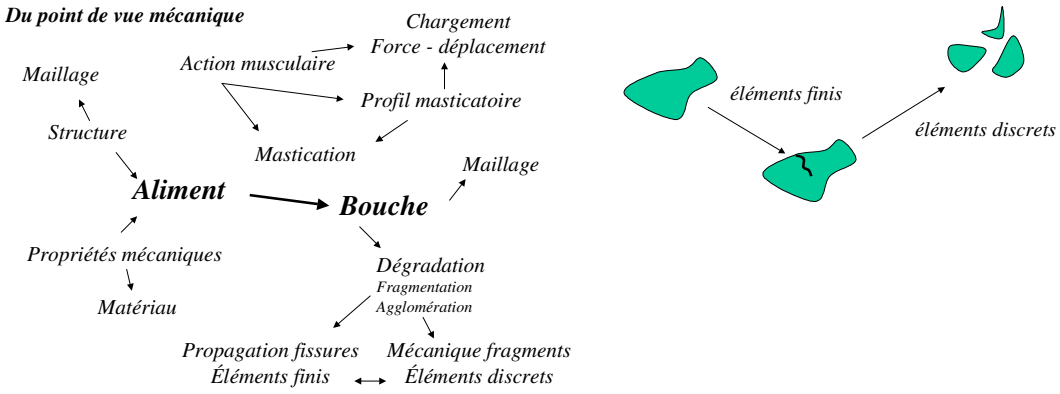

Figure 1. *(a) Approche systémique pour un modèle mécanique de la mastication (b) démarche de la thèse.*

2. Résultats majeurs :

2.1. Mécanismes de propagation de fissures :

Le raisonnement adopté dans le déroulement de la première étape (approche éléments finis) est de nature multi-échelle, allant du simple vers le plus complexe (Figure 2). Tout d'abord, la propagation de fissures dans un matériau massif (amidon amorphe dense) a été étudiée [1]. Ensuite, le problème a été transposé à un matériau alvéolaire (amidon expansé par extrusion) [2].

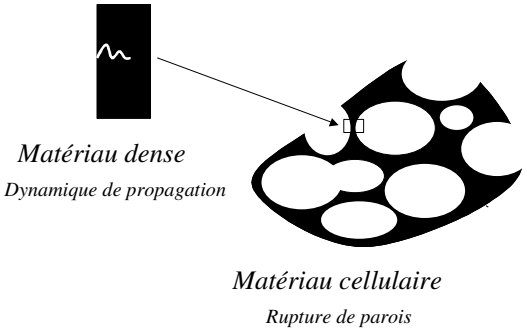

***Figure** 2. Approche multi-échelle pour la compréhension des mécanismes physiques de dégradation d'un produit céréalier.*

Un modèle en éléments finis (FEM) a été développé pour suivre la propagation d'une fissure dans un milieu homogène. Ce modèle numérique s'appuie sur une technique de découplage des degrés de liberté quand un critère physique d'extension de la fissure est satisfait. Un critère de propagation a été proposé combinant les facteurs d'intensité des contraintes associés à un état de contrainte en présence d'une fissure [1]. Des résultats numériques ont été obtenus pour le cas du mode d'ouverture (fissure perpendiculaire à la direction de chargement) et pour le cas « mode mixte local » grâce au positionnement d'un concentrateur de contraintes (trou). Le critère du taux de restitution d'énergie élastique maximal proposé a été validé expérimentalement pour un amidon amorphe vitreux, élaboré par thermomoulage, représentatif de la paroi des produits cellulaires. Le comportement de ce matériau est élastique, linéaire et isotrope et les valeurs de ses propriétés élastiques sont E= 2,62GPa et ν=0,3, sa densité = 1,43g/cm^3. Sur ce matériau amidon, avec ou sans concentrateur de contraintes, des essais de traction ont été réalisés sur un banc micro-mécanique (vitesse 40 µm/s) couplé à une caméra rapide (cadence $\leq 1.9 \times 10^5$ images/s) – Figure 4. Le modèle montre que localement, la fissure est soumise à un champ de cisaillement mais au delà du trou, la propagation se poursuit suivant un mode d'ouverture avec peu d'effet de cisaillement.

La ténacité ou le facteur d'intensité de contrainte critique est mesuré dans le cas de l'amidon dense par différents taille pré-fissurées (a=2,83 à 5 mm).

La ténacité K_{IC} est déterminée en mesurant la force à la rupture ,en utilisant la formule (1) [3]:

$$K_{IC} = \frac{F}{w\ a}\sqrt{\pi a}\left[1.12 - 0.23\left(\frac{a}{b}\right) + 10.55\left(\frac{a}{b}\right)^2 - 21.72\left(\frac{a}{b}\right)^3 + 30.39\left(\frac{a}{b}\right)^4\right] \quad (1)$$

Avec :

$$Y(a/b) = \left[1.12 - 0.23\left(\frac{a}{b}\right) + 10.55\left(\frac{a}{b}\right)^2 - 21.72\left(\frac{a}{b}\right)^3 + 30.39\left(\frac{a}{b}\right)^4\right] \quad (2)$$

Où F = la force maximale, l = la longueur entre appuis, b= la largeur, w= l'épaisseur
a = la profondeur de la préfissure, $Y\ (a/b)$= le facteur géométrique (Figure 3).

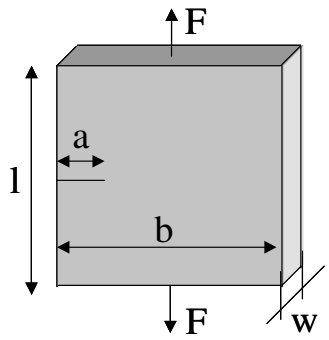

Figure 3 *: Eprouvette de traction .*

Comme indiqué dans la figure 3 les résultats donnent une ténacité moyenne égale à $K_{IC} = 2{,}28 \pm 0{,}288\ MPa\sqrt{m}$ indépendante de la taille de la pré-fissure.

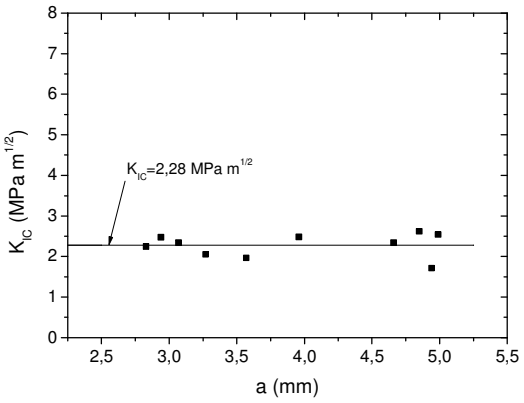

Figure 3 *: Variation de la ténacité à la rupture des échantillons avec différents taille de pré-fissures.*

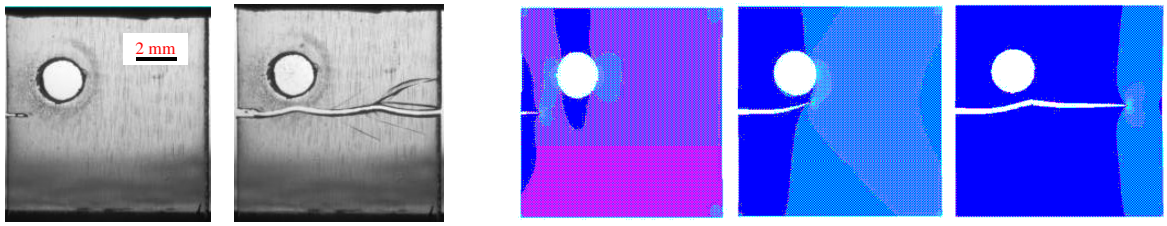

(a) (b) (c) (d) (e)

Figure 4 *: Propagation d'une fissure dans un amidon amorphe vitreux (a) –(b); modélisation de cet effet par éléments finis avec déboutonnage des nœuds (c)-(e) [1].*

Afin de généraliser le concept précédent au cas des matériaux alvéolaires représentatifs de produits céréaliers transformés, une représentation adéquate de l'effet de la structure alvéolaire a été proposée pour intégrer explicitement l'effet de la structure alvéolaire [2]. Une valeur du module élastique, comprise entre celle de l'amidon vitreux E et $E/10^9$ est ainsi attribuée à chaque élément fini du matériau amidon expansé (densité = 0,420 g/cm^3). Les résultats obtenus montrent que le modèle est capable de représenter la propagation irrégulière de fissures dans une structure alvéolaire moyennant un contraste suffisant et un encadrement adéquat des propriétés élastiques (Figure 5). Ils soulignent l'importance de la structure alvéolaire de tels matériaux sur les mécanismes de leur rupture et la propagation des fissures.

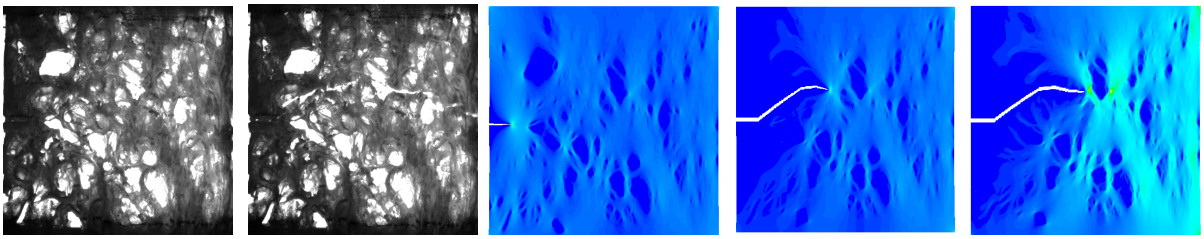

(a) (b) (c) (d) (e)

Figure 5*. Propagation d'une fissure dans un matériau amidon extrudé (a) –(b) et champs de contraintes associés à la propagation d'une fissure (c)-(e) [2].*

L'analyse des facteurs d'intensité de contrainte révèle que le ratio KII /KI est significativement affectée par la structure alvéolaire. KII / KI varie dans une large gamme de 0,003 à 0,3.

2.2. Mécanismes de mastication :

Cet aspect aborde la modélisation réaliste de la fragmentation associée aux conditions réelles de mastication (Figure 5).

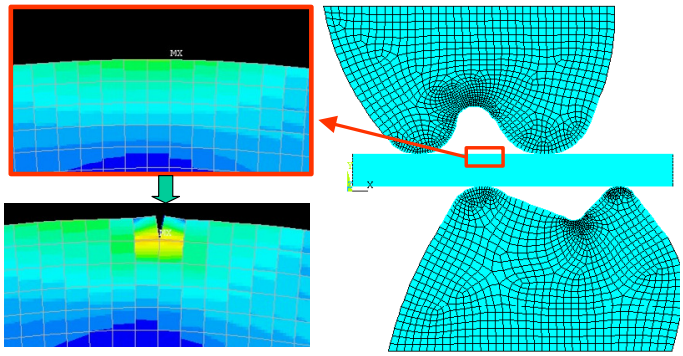

***Figure 5**. Modèle 2D pour la simulation de la mastication humaine.*

Les conditions de chargement réel ont été déterminées au laboratoire CSGA de l'INRA de Dijon, lors d'expérimentations de mastication humaine de 5 aliments réels (céréales petit-déjeuner commerciales), de comportement mécanique fragile mais de forme, densité et composition variées. L'ensemble des mouvements de mâchoires a été représenté par des cycles dont l'aire décroît au cours de la mastication par un facteur de 3 à 4, ce qui reflète la réduction de taille de l'aliment. En outre, les faibles valeurs de déplacement frontal par rapport au déplacement orthogonal suggèrent que les déformations en cisaillement sont très faibles devant celles du compression. Les vitesses d'ouverture et de fermeture sont de l'ordre de 0,1m.s^{-1}, en accord avec les valeurs couramment rencontrées, quelque soit l'âge du sujet [4]. Les différences de cinématique ne sont pas significatives entre produits sauf pour l'aire initiale des cycles qui dépend des dimensions de l'aliment. Ce comportement est typique de produits fragiles, aux propriétés mécaniques voisines [5].

Du point de vue dynamique, en raison de faibles différences d'activité entre les 4 muscles, temporaux et masséters, gauches et droits, seule l'évolution de la valeur moyenne du signal électromyographique (EMG) est prise en compte.

Nous avons ainsi trouvé que le nombre de cycles N, qui varie de 16 à 26 selon les produits, est bien corrélé à la durée totale de la séquence de mastication T, avant déglutition, variant (9 - 18s) (r^2 = 0,82, Figure 6). En outre, cette Figure montre que le déplacement en compression dy est inversement corrélé au nombre de cycles, ce qui suggère que « plus on ouvre la bouche grande, moins on l'ouvre longtemps ».

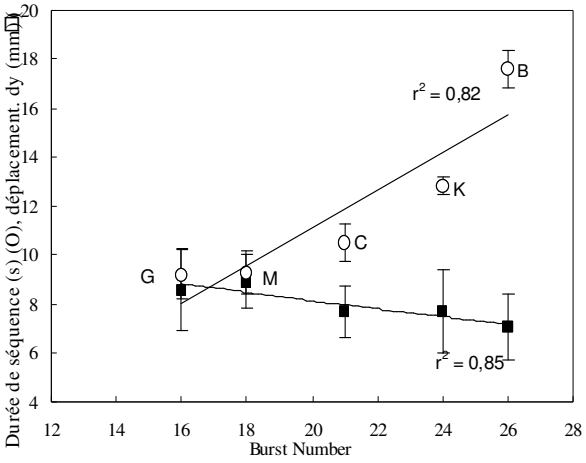

Figure 6 : *Variations, en fonction du nombre de cycles (burst), et de l'ouverture de la mâchoire (■) et de la durée de mastication (O) de céréales petit-déjeuner.*

La durée d'un cycle, ou, inversement la fréquence, varie donc peu d'un produit à l'autre, entre 0,48 et 0,6s, ce qui est proche de valeurs obtenues (0,65s) pour des aliments modèle à base de gélatine, de comportement mécanique pourtant très différent [6]. Les valeurs les plus faibles de N et T sont obtenues pour les produits les plus riches en sucre, qui sont donc déglutis plus rapidement, ce qui peut être expliqué soit par le caractère plus fragile du produit, soit par la stimulation accrue de l'activité musculaire et de la salivation [7]. Parmi les signaux EMG, l'évolution de la force maximale par cycle, pour les 5 aliments, a été ajustée par une exponentielle décroissante qui reflète bien la déstructuration progressive de l'aliment solide et confirme l'importance du « premier coup de dent » (« first bite », [8]). Les valeurs de force moyenne et de travail par cycle évoluent de façon similaire à Fmax, sans différence significative entre les produits et aucune corrélation simple ne peut être trouvée avec les variables cinématiques et la composition du produit. Les courbes de distribution d'aires des particules d'aliments, déterminées après analyse d'images des bols juste avant déglutition et représentées en fractions cumulées (Figure 10), et très bien ajustées par une fonction de type Rosin-Rammler, comme pour d'autres aliments fragmentés en cours de mastication [9]. La détermination des paramètres médiane et pente de ces distributions confirme la tendance observée pour l'influence de la composition mais surtout, permet d'établir une corrélation entre la taille médiane des fragments et la valeur moyenne des forces maximales par cycle Fmax (Figure 7).

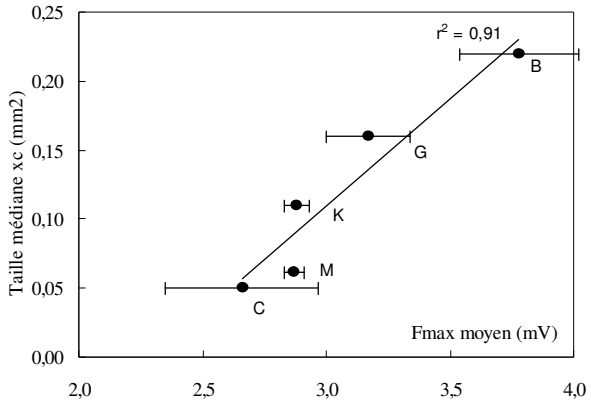

Figure 7 : *Variation de la taille médiane des particules de céréales avant déglutition avec la moyenne des forces maximales par cycle de mastication.*

Cette corrélation, qui n'a jamais été établie auparavant, doit être consolidée par d'autres valeurs expérimentales. Néanmoins, elle confirme l'importance du « first bite » pour la fragmentation de l'aliment et montre que cette étape de fragmentation gouverne la taille finale des particules, quels que soient les processus de ré-agglomération qui peuvent survenir pour former le bol avant déglutition [10]. Elle justifie l'intérêt d'une démarche de modélisation mécanique de ce phénomène, pour laquelle les résultats expérimentaux obtenus ici fournissent des conditions aux limites et des éléments de validation.

La compréhension de la mécanique de la mastication nécessite la connaissance des propriétés des produits alimentaires et de leur géométrie. La procédure expérimentale utilisée pour déterminer la géométrie des molaires s'appuie sur une analyse par profilométrie laser. Pour déterminer la structure cellulaire des deux produits (Miel Pops, Golden Grahams), on utilise la micro-tomographie RX. Le modèle éléments finis (EF) tient compte du contact dent-aliment. Il nous a permis de mettre en évidence de déformations supérieures à limites observées pour l'amidon dense. Ceci révèle donc que la fragmentation commence dès les premiers stades de la compression. Le modèle est capable, lors du premier chargement, de déterminer les distributions de déformations et de contraintes qui se développent en volume; celles-ci montrent une concentration de contraintes au voisinage des points de contact (Figure 8).

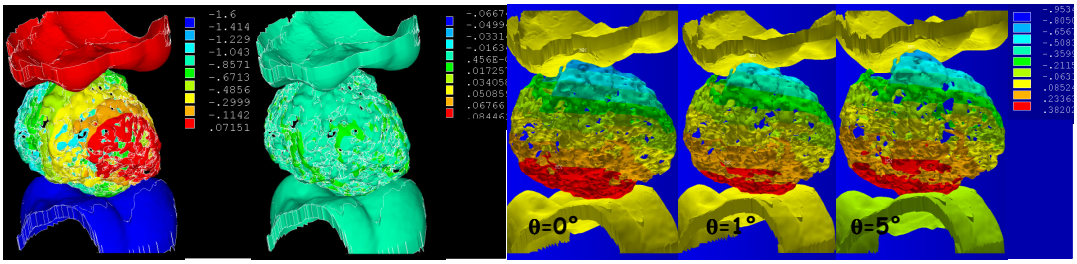

(a) (b) (c) (d) (e)

Figure 8. *Solutions nodales, (a) Déplacement-Z, (b) Déformation-Z, (c)-(e) Déplacements en fonction de l'angle de cisaillement -X.*

2.3. Mécanismes de fragmentation:

Nous avons montré que les caractéristiques dynamiques de la mastication d'aliments céréaliers alvéolaires sont bien gouvernées en premier lieu par leur comportement mécanique, et que celui-ci favorise la fragmentation des aliments durant les premiers cycles de mastication. Ces travaux sont donc poursuivis par la modélisation mécanique de la fragmentation de solides fragiles alvéolaires. Dans ce but, la méthode des éléments discrets (DEM) est employée, ce qui requiert, avant d'étudier le matériau expansé, et à l'instar de la démarche adoptée durant la première étape, d'aborder le matériau dense. Ainsi, il est possible d'en comparer les résultats, avec ceux obtenus, étape 1, par l'expérience et la modélisation par éléments finis (FEM, Chapitre II, partie 1).

Pour cela, le matériau dense est représenté par un empilement de particules sphériques de même taille. La densité initiale de l'empilement est typiquement de l'ordre de 0,6. L'ensemble est densifié jusqu'à une valeur finale de 0,72 par compaction en autorisant le chevauchement des particules et en appliquant des conditions périodiques latéralement [11]. À la fin de cette étape, chaque particule a en moyenne 7,23 contacts avec les particules voisines (Figure 9). On note que la notion de porosité induite par la méthode est compensée par des propriétés mécaniques adéquates qui permettent à l'échelle des particules de représenter le comportement. Les particules sont liées entre elles par une loi de contact qui définit un pont solide élastique. La force de contact entre deux particules se décompose en forces normale et tangentielle ; elle est définie par deux paramètres Σ_N et Σ_T.

Le comportement prédit par la DEM est linéaire, du fait de l'utilisation de la linéarité entre la force et le déplacement. L'ajustement des paramètres Σ_N et Σ_T permet un meilleur accord avec la réponse expérimentale, par rapport à la FEM. Le module élastique implémenté dans la FEM n'est pas ajusté contrairement à la démarche utilisée dans la DEM. Le module élastique du matériau est déduit de l'ajustement à une courbe contrainte-déformation expérimentale, des résultats numériques obtenus par la DEM ; on obtient la valeur E=0,257 GPa.

Paramètre matériaux :

Contrainte à la rupture (GPa)	a*	Coefficient de frottement ν
0,28	0.5	0,5

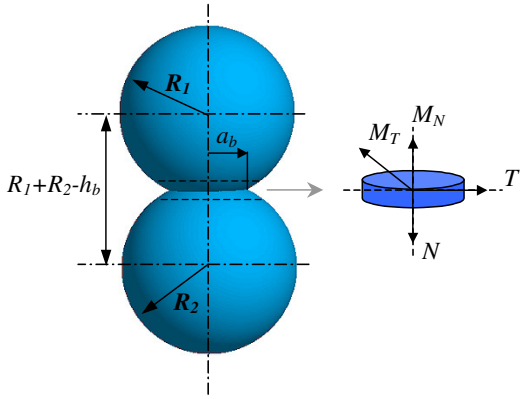

Figure 9. *Schéma de deux particules sphériques en contact.*

Pour la FEM, le départ de la fissure est directement imposé par le chargement quand le déplacement imposé correspond au déplacement à la rupture relevé expérimentalement. Les écarts entre les résultats de contrainte et déformation à la rupture des méthodes numériques DEM et FEM avec les résultats expérimentaux sont faibles (≤ 5%).

L'examen des champs de contraintes (pour FEM) et des forces (DEM) révèle des similitudes (effet papillon) entre DEM et FEM dans la distribution des champs de traction notamment aux contours du trou et au fond de la fissure, malgré la discontinuité des champs pour DEM (Figure 10). La fissure avance donc vers le concentrateur de contrainte dans les deux cas. Cependant, pour la DEM, une localisation des forces compressives (régions en bleu) due à la trajectoire courbe du front de la fissure est observée, surtout en arrière du fond de fissure. L'interaction entre les particules en arrière du front développe ces forces de compression.

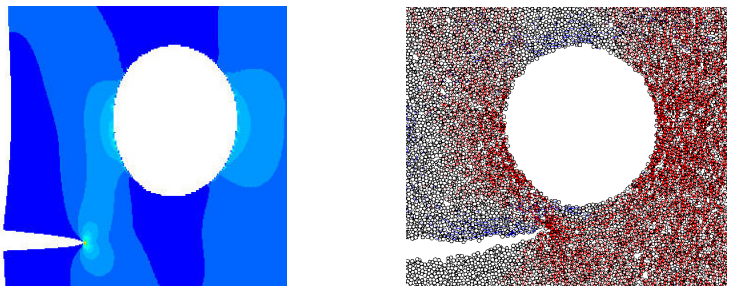

(a) (b)

Figure 10. *Distribution des (a) contraintes principales et des (b) forces obtenues après ouverture et propagation d'une fissure en utilisant FEM et DEM, respectivement.*

Si on compare les trajectoires obtenues pour une position du front de la fissure plus proche du trou, on remarque que le critère de rupture dans la DEM est plus sensible au mode mixte que celui de la FEM ce qui conduit à l'initiation de la fissure dans le trou (Figure 11a et b). Un chargement supplémentaire conduit, dans ce cas, à une concentration des contraintes aux bords du trou, puis à l'initiation d'une autre fissure. Ce critère de départ de fissure n'est pas intégré explicitement dans le formalisme DEM, ce qui démontre la capacité de la DEM à prédire la création de fissure à partir de défauts. Le résultat obtenu par FEM est, cependant, plus proche de l'observation expérimentale (Figure 11c).

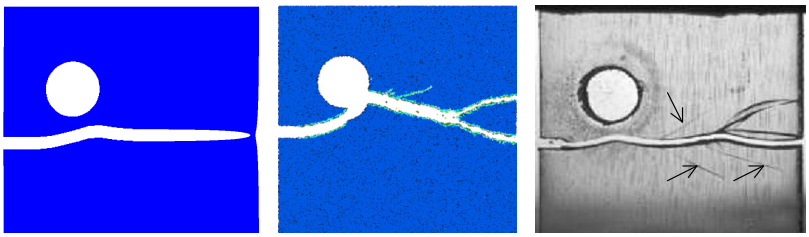

(a) (b) (c)

Figure 11. *Comparaison des trajectoires de la fissure initiée près du trou: (a) FEM, (b) DEM, (c) observation expérimentale.*

Au delà du trou, la trajectoire prédite par la DEM génère un réseau de fissures, observé expérimentalement (Figure 11c). Il peut être relié à la présence d'hétérogénéités ou à d'autres considérations énergétiques qui font qu'énergétiquement, la fissure se scinde en deux ou à vitesse de propagation critique de la fissure [17,18]. Ce phénomène de réseaux de fissure n'est pas prédit par le calcul FEM qui nécessiterait, pour cela, un critère supplémentaire. Afin de comparer les trajectoires obtenues d'une manière quantitative, la fonction $y = x(t)$ reliant les coordonnées de la position du front de la fissure est étudiée. La comparaison des trajectoires de fissure obtenues par la FEM et la DEM , et par un formalisme analytique [12, 13] montre que le calcul analytique, puis la prédiction par la DEM sont plus proches de la réalité expérimentale.

Cette étude montre que la DEM peut être utilisé pour simuler la dynamique de discontinuités dans des milieux continus. Cette méthode est capable de prédire le départ de fissures à partir d'hétérogénéités, ainsi que les instabilités de type réseaux de fissures avec comme seule hypothèse de base, la rupture d'un pont élastique entre les particules formant le matériau. La condition de pont élastique unique entre les particules permet d'obtenir une réponse élastique linéaire jusqu'à rupture du matériau. Par l'application d'un critère simple de rupture, la DEM donne une sensibilité plus marquée à la déviation de la fissure comparée à la FEM.

Dans le cas du matériau alvéolaire on applique la même propriété mécanique (module de Young) que l'amidon dense aux parois solides.

Pour réaliser la simulation numérique de la compression d'un aliment réel (céréale petit déjeuner étudiée lors de la 3ème chapitre), nous avons utilisé une microstructure cellulaire numérique aussi proche que possible de la microstructure réelle, à partir d'une image 3D issue de la tomographie RX (ESRF Grenoble). Deux plateaux sont utilisés comme conditions aux limites dans la direction z, pour imposer l'écrasement, tandis que les parois latérales se déplacent vers l'extérieur lors de la compression de l'aliment. Les propriétés physiques sont associées à chaque contact, ce qui permet une résistance à la compression. L'image contient 10^6 particules (Figure 12a). Ainsi elles permettent de déterminer correctement les variables d'entrée et de sortie du modèle qui peuvent intervenir sur la fragmentation de l'aliment. Un exemple de variable d'entrée est le type de contact entre les entités qui constituent les fragments. La sortie concerne essentiellement la distribution de taille des fragments.

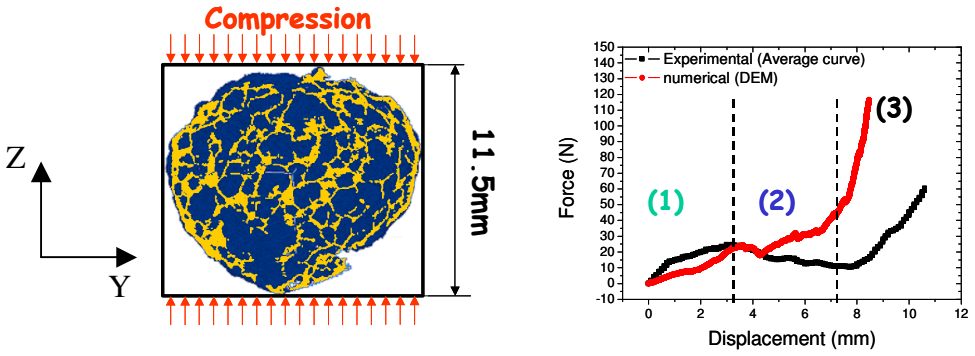

(a) (b)

Figure 12. *(a) Image 3D reconstruites du volume maximal observé par microtomographie-RX (ESRF-ID19, SPR=7µm), (b) courbe force déplacement en compression de l'aliment représenté en (a) (rouge : prédit par DEM, noir : expérimental).*

La courbe expérimentale moyenne (10 essais) de force-déplacement en compression entre 2 plateaux parallèles montre bien que la compression d'un matériau cellulaire est un processus en trois étapes (Figure 12b) : (1) d'abord une réponse typique d'un matériau cellulaire à la charge avec quelques événements de rupture des parois ; (2) un régime plateau représente une forte augmentation des événements de fracture, sans augmentation supplémentaire de la force ; (3) une augmentation rapide de la force en raison de la densification et dont la pente peut être corrélée à la rigidité du matériau constitutif. Considérant la grande dispersion des

courbes expérimentales, toutes ces étapes sont correctement prédites par la méthode des éléments discrets, et l'accord pour la force maximale (F ≈ 20N) à l'issue de la première étape, est remarquable. La pente de la courbe de densification peut être reliée à la rigidité des éléments discrets (sphères).

De plus, durant le processus de compression, le modèle DEM conduit finalement et à deux grands fragments du produit (Figure 13). Ce résultat est très proche de celui obtenu expérimentalement, avéré par analyse d'images.

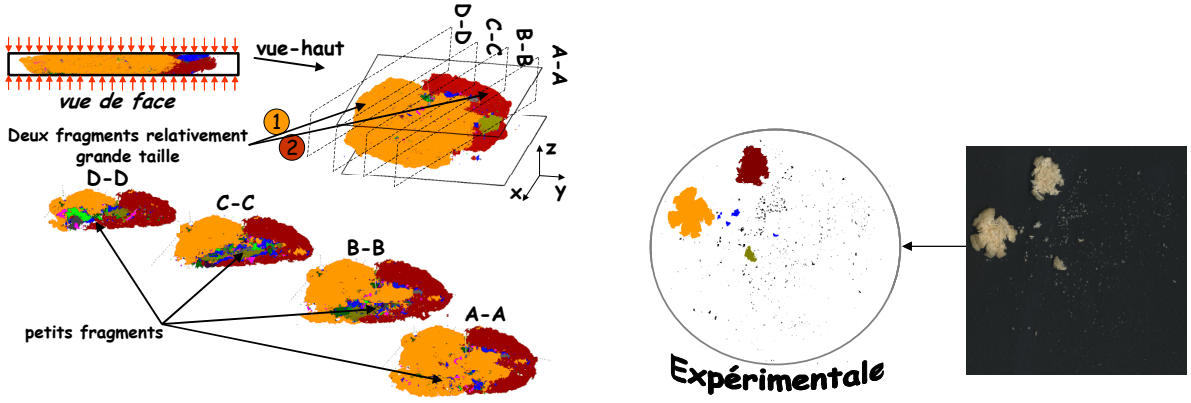

(a) (b)

Figure 18: *(a) Comparaison modèle (DEM)/ (b) expérience de compression d'un aliment céréale petit-déjeuner.*

Considérant l'importance, avérée lors de l'étape 2, des tous premiers cycles de mastication et de la compression, ce résultat confirme que la modélisation mécanique par la DEM peut contribuer efficacement à la prévision de la fragmentation d'aliments fragiles dans ces conditions de chargement. Cependant la dispersion des réponses macroscopiques expérimentales est élevée en raison de la variabilité des structures cellulaires et de la géométrie qui influence les conditions de contact évolutives en cours de compression.

Références

[1] Hedjazi L, Guessasma S, Valle GD, Benseddiq N. How cracks propagate in a vitreous dense biopolymer material. Engineering Fracture Mechanics;78(6):1328-1340.

[2] Hedjazi L, Guessasma S, Della Valle G, Benseddiq N. Finite element modelling of crack propagation in carbohydrate extruded starch with open void structure. Carbohydrate Polymers;83(4):1696-1706.

[3] Gdoutos EE. Fracture mechanics : An Introduction. Kluwer Academic Publishers, Dordrecht, The Netherlands. 1993.

[4] Kiliaridis S, Karlsson S, Kjellberg H. Characteristics of Masticatory Mandibular Movements and Velocity in Growing Individuals and Young Adults. Journal of Dental Research. 1991;70(10):1367-1370.

[5] Sandoval AJ, Chaunier L, Courcoux P, Valle GD. Bulk mechanical behavior of commercial particle food foams. Journal of Texture Studies. 2008;39(4):405-425.

[6] Peyron MA, Lassauzay C, Woda A. Effects of increased hardness on jaw movement and muscle activity during chewing of visco-elastic model foods. Experimental Brain Research. 2002;142(1):41-51.

[7] Loret C, Walter M, Pineau N, Peyron M, Hartmann C, Martin N. Physical and related sensory properties of a swallowable bolus. Physiology & Behavior. 2011(In Press).

[8] Dan H, Kohyama K. Interactive relationship between the mechanical properties of food and the human response during the first bite. Archives of Oral Biology. 2007;52(5):455-464.

[9] Baragar FA, vanderBilt A, vanderGlas HW. An analytic probability density for particle size in human mastication. Journal of Theoretical Biology. 1996;181(2):169-178.

[10] Yven C, Guessasma S, Chaunier L, Della Valle G, Salles C. The role of mechanical properties of brittle airy foods on the masticatory performance. Journal of Food Engineering;101(1):85-91.

[11] Martin CL, Bordia RK. The effect of a substrate on the sintering of constrained films. Acta Materialia. 2009;57(2):549-558.

[12] Valentini M, et al. Crack Propagation in a Brittle Elastic Material With Defects. Journal of Applied Mechanics. 1999;66(1):79-86.

[13] A.B. Movchan NVM, Movchan. Mathematical Modelling of Solids with Non-Regular Boundaries. CRC Press, Boca Raton, FL, 1995.

Conclusion et perspectives

Une approche originale basée sur la mécanique est proposée pour étudier la déstructuration des aliments céréaliers, base de notre alimentation, dans la cavité buccale, capteur sensoriel et première étape de la digestion. Cette approche permet de relier le comportement mécanique, donc la texture de l'aliment, sous des conditions complexes de mastication qui peuvent varier en fonction du profil masticatoire de l'individu. La démarche EF est largement entamée et validée par comparaison avec des résultats expérimentaux. Cependant, par cette méthode (MEF), il est plus difficile de modéliser la fragmentation des produits. Pour palier à cette difficulté, la démarche est complétée par la modélisation par la méthode des éléments discrets (DEM). Par cette méthode, il est possible de décrire l'évolution du produit au cours de la mastication.

La fissuration d'une matrice solide alimentaire est définie par un ensemble de critères d'amorce et de propagation. L'amorce est corrélée à la contrainte maximale que le matériau peut accumuler sans rupture. Il s'agit donc d'un critère global qui ne met pas en évidence le rôle des défauts structuraux à partir desquels des phénomènes de localisation et d'amorce de fissure se développent. En d'autres termes, la position et l'extension des préfissures sont connus dans nos simulations, alors que la propagation nécessite le recours à des critères plus élaborés. La propagation de fissures est associée à la résistance à la fissuration et met en évidence la notion de facteurs de concentration des contraintes (KI, KII). La direction de propagation est donc calculée à l'aide de ces grandeurs en utilisant les champs de déplacements au voisinage de la pointe de la fissure (critère du taux de restitution d'énergie). Le modèle éléments finis est validé pour des configurations où le mode d'ouverture est prédominant (cas des éprouvettes trouées). On obtient alors pour l'amidon une résistance critique à la fissuration de 2,28 $MPa.m^{1/2}$. Si les calculs restent sensibles au maillage notamment à cause de sa régularité, l'étude de sensibilité révèle qu'il est possible de réduire cette sensibilité par l'ajustement des propriétés mécaniques et de la taille des éléments. Cette sensibilité reste cependant une limitation de notre démarche par rapport à d'autres méthodes comme le maillage irrégulier ou Xfem. Diminuer la taille des éléments a tout de même un avantage, celui de prendre en compte les faibles angles de propagation en ajustant le pas de découplage des degrés de liberté. Nos résultats quantifient également les modifications de trajectoire des fissures dans un matériau cellulaire malgré le mode d'ouverture global appliqué. La condition à satisfaire reste le contraste que doit pouvoir révéler la microscopie optique, insuffisant notamment pour une épaisseur élevée des éprouvettes. L'autre limite du modèle est d'assurer une taille d'éléments raisonnable par rapport à la taille des cellules, pour éviter de propager une fissure dans un "vide" alors que le principe de la méthode implique

plutôt de traiter le matériau cellulaire comme un matériau effectif ayant des propriétés élastiques proportionnelles à sa densité.
La mastication est une fonction essentielle et complexe dont on connaît aujourd'hui de mieux en mieux le déroulement. Nous avons mis en avant le rôle des paramètres physiologiques lors de la mastication de produits céréaliers fragiles pour un sujet. Les résultats révèlent l'importance de la dégradation des produits testés (céréales petit-déjeuner).
L'amplitude verticale d'ouverture est corrélée négativement au temps de mastication. L'analyse EMG souligne également que le travail de mastication est corrélé à la force moyenne. Les distributions finales de taille des fragments des produits céréaliers étudiés sont différentes et reflètent principalement la variation de la force maximale.

Afin de simuler le processus de la mastication numériquement, nous avons eu recours à la méthode des éléments finis (FEM) pour étudier la compression que subit l'aliment lors du premier cycle. Notre démarche montre qu'il est possible d'approcher la mécanique de mastication en adoptant un contact adéquat dent - aliment tout en représentant fidèlement la structure 3D de l'aliment. Les résultats montrent que la fragmentation est susceptible d'apparaître dès les premiers stades de déformation avant l'occlusion complète. Nos calculs montrent également qu'il est possible de discriminer les produits céréaliers de différentes formes en partant des distributions des déformations. Ce résultat souligne, quantitativement, le rôle de la géométrie et la structure cellulaire dans la fragmentation.

L'analyse de la complexité de l'interaction « aliments-bouche » lors de la mastication fait appel à la méthode d'éléments discrets (ED) englobant la fragmentation de particules en cours de dégradation de la matrice. La propagation de fissures dans un amidon vitreux est à nouveau étudiée numériquement, analytiquement et expérimentalement. Notre étude montre que la DEM peut être utilisé pour simuler la dynamique de discontinuités dans des milieux continus. En effet, la DEM est capable de prédire le départ de fissures sur des hétérogénéités ainsi que les instabilités de type réseaux de fissures avec comme seule hypothèse de base la rupture d'un pont élastique entre les particules formant le matériau. La condition de pont élastique unique entre les particules permet d'obtenir une réponse élastique linéaire jusqu'à rupture du matériau. Par l'application d'un critère simple de rupture, la DEM donne une sensibilité plus marquée à la déviation de la fissure comparée à la FEM. L'étude de la fragmentation d'un produit céréalier par la méthode des éléments discrets révèle un comportement typique d'un matériau cellulaire affichant trois stades de déformation. L'analyse des fragments indique une

distribution hétérogène contenant notamment quelques fragments de grande taille et un grand nombre de petites tailles. Les résultats obtenus mettent en évidence un faible nombre de rupture de parois (moins de 2%), qui est associé à une partie faible de l'énergie mécanique qui est transmise à l'aliment. Un bon accord qualitatif est obtenu entre le processus de fragmentation numérique et expérimental.

Enfin, en raison du caractère pluridisciplinaire des travaux et du temps limité d'un travail de thèse, les résultats obtenus sont des résultats partiels. Ils peuvent être complétés par les éléments suivants, qui sont autant d'étapes de progression dans la modélisation de la mastication d'aliments solides ; nous tentons de les présenter par ordre croissant de difficulté et d'investissement :

* sur le **plan expérimental** de la mastication, étant donnée la grande variabilité interindividuelle, il conviendrait d'abord de situer le sujet dans une population moyenne, notamment pour la salivation et la performance masticatoire, et ensuite, de convertir les mesures d'activité musculaire (mV) en force (N); ces études sont en cours à l'INRA, les résultats pourront être comparés à ceux issus de la bibliographie, afin de fournir une base de comparaison réaliste ;

* il faudra appliquer les **méthodes de modélisation** (FEM et DEM) à d'autre produits céréaliers alvéolaires, d'abord pour conforter la validation entrevue ici et ensuite, pour mieux hiérarchiser les contributions de leurs propriétés, notamment eu égard à l'effet qualitatif du sucre lors du comportement masticatoire ;

* l'étape précédente amènerait aussi à **conforter les bases d'application** des méthodes numériques à ces solides cellulaires, d'une part en affinant la distribution des défauts (alvéoles) par attribution d'une valeur de module (FEM), d'autre part en précisant leurs propriétés mécaniques, y compris leur densité, taille, morphologie, qui gouvernent les lois de contact des particules (DEM);

* la **comparaison de résultas numériques et expérimentaux** serait alimentée par la conversion les déformations en distribution des fragments afin de comparer les distributions de tailles expérimentale et numérique depuis le premier jusqu'au dernier cycle de la mastication; une fois le déplacement des dents décrit par celui, mesuré, des mandibules, alors cette comparaison peut être étendue aux forces appliquées sur les dents à partir de mesures EMG et une calibration adéquate permettant d'avoir accès à l'effort transmis aux dents par les muscles de mastication. Les forces de réaction prédites par le modèle numérique pourront, à cette condition, être comparées aux forces mesurées;

* enfin, pour compléter les simulations jusqu'au dernier cycle de mastication et ainsi **accroître leur caractère réaliste**, il faudra prendre en compte le rôle de la salive ; ceci peut être envisagé en modifiant les lois de contact entre les particules sphériques (DEM) pour aborder la modélisation de l'agglomération ; en outre il faudrait introduire la plasticité pour étudier la propagation de la fissures dans les aliments ayant des teneur en eau plus importantes.

Ces perspectives sont nombreuses et requerront donc un investissement significatif, en accord avec l'importance du programme entrepris à l'INRA sur la compréhension du devenir des aliments dans le tube digestif; nous espérons que ce travail constitue une base solide de la démarche de modélisation adoptée dans cette perspective.

Modélisation mécanique de la fracture et de la fragmentation d'aliments cerealiers modele sous des conditions aux limites de la mastication

Résumé de la thèse

La compréhension du devenir des aliments dans le tube digestif de l'homme doit permettre de concevoir de nouveaux aliments associés à des cibles nutritionnelles, en améliorant leur digestibilité, tout en préservant les propriétés sensorielles. Dans ce contexte, notre travail est guidé par la nécessité de développer une approche mécanique de la mastication humaine de produits céréaliers alvéolaires, pris comme aliments modèle. Nous avons, d'abord, déterminé les principes mécaniques qui régissent la propagation des fissures dans les produits dense et alvéolaire à base d'amidon, représentatifs de ces aliments, en utilisant la méthode des éléments finis. Ensuite, nous avons étudié la mise en œuvre de conditions réalistes comme la géométrie du mandibule et le profil masticatoire par une modélisation déterministe en tenant compte de la structure de ces aliments et de leurs propriétés mécaniques. Enfin, nous avons simulé la fragmentation de produits céréaliers en utilisant la méthode des éléments discrets. Nos résultats ont été validés à l'aide de tests mécaniques, mais aussi d'expérimentations de mastication humaine d'aliments céréaliers réels. Au cours de ces dernières, la cinématique mandibulaire, l'activité musculaire et la distributions des fragments alimentaires ont été déterminées. Nos résultats montrent que la modélisation mécanique de la fragmentation d'aliments solides alvéolaires sous des conditions de mastication permet de mettre en évidence l'importance de leurs caractéristiques structurales.

Mot clés

Amidon, Mastication, Fragmentation, Propagation de la fissure, Eléments finis, Eléments discrets

Mechanical modelling of fracture and fragmentation of cereal foods under mastication boundary conditions

Abstract

Understanding the future of food in the human digestive tract should allow to design new foods with nutritional targets, improving their digestibility, while maintaining their sensory properties. In this context, our work is guided by the need to develop a mechanical approach of chewing alveolar cereal products, taken as model food. We have, first, determined the mechanical principles that govern the propagation of cracks in the dense starch-based cellular products, representative of these foods, using finite element method. Next, we studied the implementation of realistic conditions of chewing as the geometry of the mandible and masticatory profile, by a deterministic model taking into account the structure of these foods and their mechanical properties. Finally, we simulated the fragmentation of cereal products using the discrete element method. Our results were validated using mechanical tests, but also experiments with human mastication of real cereal foods, in which mandibular kinematics, muscle activity and food distributions of fragments were determined. Our results show that the mechanical modeling of the fragmentation of cellular solid foods under realistic conditions of chewing allows to highlight the importance of their structural characteristics.

Keywords

Starch, Mastication, Fragmentation, Crack propagation, Finite Element Method, Discrete Element Method

Discipline : Science des matériaux

N°:
(Ne rien inscrire, attribué par la bibliothèque)